

UNIVERSIDADE FEDERAL DE CAMPINA GRANDE
CENTRO DE CIÊNCIAS E TECNOLOGIA
UNIDADE ACADÊMICA DE ENGENHARIA QUÍMICA
PROGRAMA DE PÓS GRADUAÇÃO EM ENGENHARIA QUÍMICA

**ENGINEERING APPLICATIONS OF TYPICAL NON-REACTING
FLOWS USING COMPUTATIONAL FLUID DYNAMICS**

Paloma Lins Barros

Campina Grande, Paraíba, Brazil
November, 2020

UNIVERSIDADE FEDERAL DE CAMPINA GRANDE
CENTRO DE CIÊNCIAS E TECNOLOGIA
UNIDADE ACADÊMICA DE ENGENHARIA QUÍMICA
PROGRAMA DE PÓS GRADUAÇÃO EM ENGENHARIA QUÍMICA

**APLICAÇÕES DE ENGENHARIA DE ESCOAMENTOS NÃO-
REACIONAIS USANDO FLUIDODINÂMICA COMPUTACIONAL**

Paloma Lins Barros

Campina Grande, Paraíba, Brazil
Novembro, 2020

Paloma Lins Barros

**ENGINEERING APPLICATIONS OF TYPICAL NON-REACTING
FLOWS USING COMPUTATIONAL FLUID DYNAMICS**

Dissertation submitted to the Graduate Program in Chemical Engineering of the Federal University of Campina Grande in fulfillment for the degree of Master of Chemical Engineering. Area: Chemical Engineering.

Supervisor: Dr. José Jailson Nicácio
Alves

Campina Grande, Paraíba, Brazil

November, 2020

B277e

Barros, Paloma Lins.

Engineering applications of typical non-reacting flows using computational fluid dynamics / Paloma Lins Barros. – Campina Grande, 2020.

111 f. : il. color.

Dissertação (Mestrado em Engenharia Química) – Universidade Federal de Campina Grande, Centro de Ciências Biológicas e da Saúde, 2020.

"Orientação: Professor Dr. José Jailson Nicácio Alves".

Referências.

1. Fluidodinâmica Computacional. 2. Simulação Numérica. 3. Hidrociclone. 4. Classificação de áreas. 5. Emissão de Gás. 6. Liberação Bifásica I. Alves, José Jailson Nicácio. II. Título.

CDU 544.272(043)

Paloma Lins Barros

**ENGINEERING APPLICATIONS OF TYPICAL NON-REACTING
FLOWS USING COMPUTATIONAL FLUID DYNAMICS**

Dissertation submitted to the Graduate Program in Chemical Engineering of the Federal University of Campina Grande in fulfillment for the degree of Master of Chemical Engineering. Area: Chemical Engineering.

Aprovado em 23/11/2020



Prof. Dr. José Jailson Nicácio Alves

Orientador



Prof. Dr. Antônio Tavernard Pereira Neto

Avaliador Interno



Prof. Dr. Talles Caio Linhares De Oliveira

Avaliador Externo

Campina Grande, Paraíba, Brazil

Novembro, 2020

Ata de apresentação da 488ª Dissertação de **Mestrado** do Programa de Pós-Graduação em Engenharia Química

Ao vigésimo terceiro dia do mês de novembro de dois mil e vinte às 14:00horas por videoconferência, reuniu-se a **Banca Examinadora** nas formas e termos do Art. 1º e 2º do Regulamento Interno do Programa de Pós-Graduação em Engenharia Química, composta pelos seguintes membros: Prof. Dr. José Jailson Nicácio Alves (**Orientador /UFCG**), Prof. Dr. Antônio Tavernad Pereira Neto (Examinador Interno /UFCG), e o Prof. Dr. Talles Caio Linhares de Oliveira (Examinador Externo /UNINASSAU-CG), para exame da **Dissertação de Mestrado** intitulada “**Engineering applications of typical non-reacting flows using computational fluid dynamics**”, da aluna **Paloma Lins Barros**. Após a explanação da candidata o Orientador passará a palavra aos componentes da Banca Examinadora. Terminada a arguição a Banca Examinadora, após reunião secreta, a atribuir os conceitos aqui transcritos: Prof. Dr. José Jailson Nicácio Alves __APROVADO__, Prof. Dr. Antônio Tavernad Pereira Neto __APROVADO__, e o Prof. Dr. Talles Caio Linhares de Oliveira __APROVADO__. De acordo com o **Artigo 57 do Regulamento Interno do PPGEQ** a candidata foi considerada __APROVADA__. Encerrada a sessão secreta o Orientador informará o resultado do consenso. Nada mais havendo a tratar foi encerrada a sessão, para constar eu Maricé Pereira da Silva – Secretária do PPGEQ, lavrei a presente Ata que assino com os membros da Banca Examinadora e a candidata.

Secretária: Maricé Pereira da Silva

Orientador: 

Examinador: Talles Caio Linhares de Oliveira

Examinador: Antônio Tavernad Pereira Neto

Candidata: Paloma Lins Barros

Acknowledgements

My deepest gratitude to professor José Jailson Nicácio Alves for his supervision and relevant suggestions that made possible the completion of this work. Thank you for all the support over the last eight years.

To all my friends and colleagues from LENP, for all the teamwork and moments that we spent together that made everything worth it. Special thanks to my friend Claudemi for sharing valuable comments and ideas.

To Ranny, Natalya, Victor, Felipe, and Rodolpho for all the encouragement and support. Your friendship means a lot to me.

Immeasurable appreciation to my family Jaci, Edilson, and Anderson, for being so patient. I am grateful for all the emotional support and love.

Resumo

A fluidodinâmica computacional (CFD) é uma área de estudo de vasta aplicação na engenharia. Ela vem se popularizando cada vez mais com a maior facilidade ao acesso a computadores de alta performance para realização de simulações mais complexas. A aplicação de estudos numéricos utilizando ferramentas de fluidodinâmica computacional é particularmente importante em cenários onde experimentos são inviáveis, em situações nas quais variáveis desejadas não podem ser medidas experimentalmente, ou ainda quando não há solução analítica. Nesse sentido, este trabalho tem como objetivo adotar técnicas de CFD em alguns estudos de caso presentes na engenharia química: separação de sólidos em hidrociclones, emissão de gás e jatos bifásicos. Os casos estudados trazem diferentes abordagens de escoamentos multifásicos, modelos de turbulência e tipos de malha construída. Isto torna mais ampla a discussão em relação aos modelos presentes em softwares comerciais e coloca em destaque a importância da escolha adequada da abordagem a ser utilizada. Para cada caso de estudo contemplado neste trabalho, foram definidos os modelos matemáticos e condições de contorno utilizadas. Os resultados obtidos auxiliaram no entendimento mais detalhado do fenômeno estudado e possibilitaram investigar diferentes cenários a partir de um caso base, corroborando a relevância da modelagem e simulação de processos utilizando ferramentas em CFD para aplicações de engenharia.

Palavras-chave: Fluidodinâmica computacional, Simulação numérica, Hidrociclone, Classificação de área, Emissão de gás, Liberação bifásica.

Abstract

Computational fluid dynamics (CFD) is an area of study with a wide application in engineering. It has become increasingly popular with greater ease of access to high-performance computers to perform more complex simulations. The application of numerical studies using computational fluid dynamics tools is particularly important in scenarios where experiments are not feasible, in situations in which desired variables cannot be measured experimentally, or even when there is no analytical solution. In view of that, this work aims to adopt CFD techniques in some case studies that are present in chemical engineering: separation of solids in hydrocyclones, gas emission, and two-phase flow jets. The studied cases address different approaches of multiphase flows, turbulence models, and types of constructed mesh. This broadens the discussion regarding the models presented in commercial software and highlights the importance of choosing the appropriate approach to be used. For each case study included in this work, the mathematical models and boundary conditions were defined. The obtained results provided a more detailed understanding of the studied phenomenon and made it possible to evaluate different scenarios from a verified case model, which corroborates the relevance of modeling and simulation using CFD tools for engineering applications.

Keywords: Computational fluid dynamics, Numerical simulation, Hydrocyclone, Hazardous area classification, Gas release, Two-phase release.

List of figures

Figure 3.1: Principal features of the hydrocyclone (Bradley, 1965)	35
Figure 3.2: Flow diagram for the experiment and experimental setup. 1) Reservoir containing the feed clay, 2) stirrer, 3) pressure valve control, 4) centrifugal pump, 5) hydrocyclone, and 6) reservoir containing the overflow product.....	39
Figure 3.3: RWK-42L hydrocyclone dimensions.....	43
Figure 3.4: Isometric view of the geometry.....	43
Figure 3.5: Grid independence test for (a) volume fraction in the overflow and feed mass flow; (b) axial velocity profile.	45
Figure 3.6: Air volume fraction profile for hydrocyclone with an attached hopper at (a) 0.05s; (b) 0.2s; (c) 0.4s; (d) 1s.	46
Figure 3.7: Air volume fraction profile for hydrocyclone without an attached hopper at (a) 0.05s; (b) 0.2s; (c) 0.4s; (d) 1s.	47
Figure 3.8: Overflow granulometric efficiency and cumulative volume fraction of fine particles for (a) configuration 1; (b) configuration 2; (c) configuration 3; (d) configuration 4.	50
Figure 3.9: Comparison of turbulence models for (a) granulometric underflow efficiency; (b)cumulative volume fraction; (c) axial velocity; (d) tangential velocity....	51
Figure 3.10: Effect of inlet pressure on (a) fine particles volume fraction at the overflow; (b) inlet mass flow rate and velocity.	54
Figure 3.11: Scale-up analysis: (a) Cumulative volume fraction in the over flow; (b) recovery to underflow comparison with Plitt model.....	57
Figure 4.1: Configuration of a gas cloud after a jet release (adapted from IEC 60079-10-1).....	63
Figure 4.2: Assessment of the degree of dilution (IEC 60079-10-1).....	63
Figure 4.3: Hazardous area classification into zones (IEC 60079-10-1).....	64
Figure 4.4: Estimation of hazardous area extent (IEC 60079-10-1).	64

Figure 4.5: Geometry definitions: (a) schematic three-dimensional geometry; (b) dimensions.	67
Figure 4.6: Generated mesh.....	69
Figure 4.7: Model verification with experimental data from Papanikolaou et <i>al.</i> (2012).	70
Figure 4.8: Concentration profile along the release axis for wind in the jet direction for hydrogen.	71
Figure 4.9: Concentration profile along the release axis for wind in the jet direction for methane.	71
Figure 4.10: Concentration profile along the release axis for wind in the jet direction for propane.	72
Figure 4.11: Hazardous extent for the hydrogen leakage: (a) to LFL; (b) to ½ LFL; (c) to ¼ LFL.	73
Figure 4.12: Hazardous extent for the methane leakage: (a) to LFL; (b) to ½ LFL; (c) to ¼ LFL.	73
Figure 4.13: Hazardous extent for the propane leakage: (a) to LFL; (b) to ½ LFL; (c) to ¼ LFL.	74
Figure 4.14: Hydrogen profiles along the release axis for wind in the opposite direction of the jet: (a)molar fraction; (b)mixture velocity magnitude.	75
Figure 4.15: Methane profiles along the release axis for wind in the opposite direction of the jet: (a)molar fraction; (b)mixture velocity magnitude.	75
Figure 4.16: Propane profiles along the release axis for wind in the opposite direction of the jet: (a)molar fraction; (b)mixture velocity magnitude.	75
Figure 4.17: Hazardous volume for the hydrogen leakage: (a) to LFL; (b) to ½ LFL; (c) to ¼ LFL.	77
Figure 4.18: Hazardous volume for the methane leakage: (a) to LFL; (b) to ½ LFL; (c) to ¼ LFL.	78
Figure 4.19: Hazardous volume for the propane leakage: (a) to LFL; (b) to ½ LFL; (c) to ¼ LFL.	78

Figure 4.20: Methane gas cloud at $\frac{1}{4}$ LFL for airspeed equals to (a)-10m/s; (b)10m/s; (c)-8m/s; (d)8m/s; (e)-6m/s; (f)6m/s; (g)-4m/s; (h)4m/s; (i)-2m/s; (j)2m/s.	79
Figure 5.1: Two-phase release.....	87
Figure 5.2: SMD as a function of the degree of superheat (Kay et <i>al.</i> , 2010).....	92
Figure 5.3: Dimensions of the computational domain.....	94
Figure 5.4: Isometric view of the constructed geometry.	95
Figure 5.5: Constructed grid for a three-dimensional two-phase flow release.....	97
Figure 5.6: Two-phase release model verification: (a)velocity profile; (b)temperature profile.	100
Figure 5.7: Propane gas cloud at $\frac{1}{4}$ LFL for the Equilibrium two-phase jet simulation.	102
Figure 5.8: Propane gas cloud at $\frac{1}{4}$ LFL for the Non-equilibrium jet simulation.	102

List of tables

Table 2.1: Constant values for Shear Stress Transport model.....	27
Table 2.2: RSM turbulence model constants.	29
Table 3.1: Volume fraction of the particles in the feed.	40
Table 3.2: Boundary conditions for the hydrocyclone study case.	41
Table 3.3: Configuration of the simulations.....	42
Table 3.4: CFD model verification against experimental data ($R_7=6\text{mm}$, $R_8=3\text{mm}$, $P=3\text{bar}$).	48
Table 3.5: CFD model verification against experimental data ($R_7=6\text{mm}$, $R_8=3\text{mm}$, $P=4\text{bar}$).	48
Table 3.6: CFD model verification against experimental data ($R_7=6\text{mm}$, $R_8=5\text{mm}$, $P=3\text{bar}$).	49
Table 3.7: CFD model verification against experimental data ($R_7=6\text{mm}$, $R_8=5\text{mm}$, $P=4\text{bar}$).	49
Table 3.8: Predicted volume fraction of the fine particles and their mean diameters in the overflow.	52
Table 3.9: Predicted reduced granulometric efficiency in the overflow.	55
Table 4.1: Zone type definition for hazardous area classification	61
Table 4.2: Storage and leakage conditions.....	66
Table 4.3: Boundary condition definition.....	68
Table 4.4: Grid Independence test (methane, $P_s=100\text{bar}$, $d_o=1\text{mm}$, $T_s=300\text{K}$, $u_w=0\text{m/s}$).	69
Table 4.5: Comparison between CFD results and IEC 60079-10-1(2015) for hydrogen.	80
Table 4.6: Comparison between CFD results and IEC 60079-10-1(2015) for methane.	81

Table 4.7: Comparison between CFD results and IEC 60079-10-1(2015) for propane.	82
Table 5.1: Two-phase release regions.....	87
Table 5.2: Definition of the boundary conditions.	96
Table 5.3: Inlet boundary conditions.	96
Table 5.4: Grid independence test.....	97
Table 5.5: Sensitivity analysis of the number of computational particles.	98
Table 5.6: Boundary condition values.....	99
Table 5.7: Hazardous extent and volume.	101
Table 5.8: Comparison between CFD and IEC 60079-10-1(2015) results for hazardous extent.	103

List of symbols

C_p	Specific heat capacity at constant pressure
C_D	Drag coefficient
C_S	Solid concentration
d_p	Particle diameter
d_o	Orifice diameter
d_{25}	Particle diameter with 25% separation efficiency
d_{50}	Cut size diameter
d_{75}	Particle diameter with 75% separation efficiency
D_i	Kinematic diffusivity of component i
D_f	Diameter of the inlet
D_o	Diameter of the overflow
D_u	Diameter of the underflow
E_T	Global efficiency
E'_T	Reduced global efficiency
E_G	Granulometric efficiency
E'_G	Reduced granulometric efficiency
F_R	Resultant force
g	Gravitational acceleration
H	Free vortex height
h_{tot}	Total enthalpy
L	Nozzle length
MW_C	Molecular weight of component
MW_g	Molecular weight of gas mixture
m_p	Particle mass
Nu	Nusselt number
n	Size distribution spread parameter
P	Pressure
Q_f^L	Feed volumetric flow of the liquid phase
Q_u^L	Underflow volumetric flow of the liquid phase
R_L	Liquid ratio

Re	Reynolds number
S	Volume split
Sh	Sherwood number
S_M	Momentum source
S_{MS}	Mass source
S_E	Energy source
t	Time
T	Temperature
u	Velocity
u_w	Wind velocity
W_u	Underflow mass flow rate of solid particles
W_f	Feed mass flow rate of solid particles
We	Weber number
x_u	Underflow mass fraction of particles larger than a given diameter
x_f	Feed mass fraction of desired particles larger than a given diameter
X_V	Cumulative volume fraction of fine particles
Y_i	Mass fraction of component i
α	Sharpness of separation
ρ	Density
λ	Thermal conductivity
μ	Dynamic viscosity
σ	Surface tension coefficient
ΔH^{vap}	Enthalpy of vaporization
ΔT_{sh}	Superheat temperature
$\Gamma_{M_{eff}}$	Effective molecular diffusion coefficient

Contents

Introduction.....	19
1.1 Motivation.....	19
1.2 General background.....	19
1.3 Outline of the thesis.....	20
1.4 Publications.....	21
Computational Fluid Dynamics.....	22
2.1 Pre-processing.....	22
2.2 Hydrodynamic equations.....	22
2.3 Multiphase flows.....	23
2.3.1 <i>Particle tracking</i>	23
2.3.1.1 <i>Particle displacement</i>	23
2.3.1.2 <i>Momentum transfer</i>	24
2.3.1.3 <i>Heat transfer</i>	24
2.3.1.4 <i>Mass transfer</i>	25
2.3.2. Free surface model.....	25
2.3.3 Particle model.....	25
2.4 Turbulence model.....	26
2.4.1. Shear Stress Transport.....	26
2.4.2. Reynolds Stress Model.....	28
2.4.3. Large Eddy Simulation.....	29
2.5 Post-processing.....	31
Liquid-solid flow in hydrocyclones.....	32
3.1 Study case background.....	32
3.1.1 Hydrocyclone fundamentals overview.....	34
3.1.2 Air Core.....	36
3.1.3 Plitt model.....	36
3.1.4 Scale-up.....	37
3.2 Experimental setup.....	38
3.3 CFD model.....	40
3.3.1 Air core prediction model.....	42
3.3.2 Geometry.....	42
3.3.3 Grid independence study.....	43
3.4 Results.....	45
3.4.1 Air core results.....	45

3.4.2 CFD model verification.....	47
3.4.3 CFD model utilization.....	51
3.4.4 Scale-up analysis.....	55
3.5 Final considerations	58
Wind effect on gas jets for hazardous area classification.....	59
4.1 Study case background.....	59
4.1.1 Hazardous area classification overview	61
4.1.2 Gas jet release.....	65
4.2 CFD model.....	66
4.2.1 Grid independence study	68
4.2.1 CFD model verification.....	69
4.3 Results	70
4.4 Final considerations	83
Two-phase jets for hazardous area classification.....	85
5.1 Study case background.....	85
5.1.1 Two-phase jet overview	86
5.1.2 Storage condition.....	89
5.1.3 Release condition	89
5.1.3.1 <i>Equilibrium two-phase jet</i>	89
5.1.3.2 <i>Non-equilibrium jet</i>	90
5.1.4 After-expansion condition.....	91
5.1.4.1 <i>Droplet size</i>	92
5.3 CFD model.....	94
5.3.1 Grid independence study	96
5.3.2 Particle number independence study	98
5.3.3 Model verification	98
5.4 Results	100
5.5 Final considerations	104
References	105

Chapter 1

Introduction

This chapter of the master thesis gives an overview of the present work, including a general motivation and a brief discussion of conducted studies.

1.1 Motivation

Numerical experiments are largely used to obtain reliable results. For instance, Computational Fluid Dynamics (CFD) is an alternative to real experiments for many areas of study. In chemical engineering, CFD may apply to reaction systems, phase separation, heat transfer, and other cases. The wide range of applications allows rigorous analysis of specific scenarios, especially when real experiments are unfeasible. Therefore, this thesis evaluates fluid interactions using different approaches and provides straightforward guidance concerning the models used in each case.

1.2 General background

Computational Fluid Dynamics is an important tool to provide a detailed analysis of fluid flows. It contributes to understand complex phenomena such as multiphase flows by encompassing the governing equations from the conservation laws (Blazek, 2015). However, it also requires a deeper knowledge concerning model selection for specific scenarios.

The CFD simulation complements experimental data and analytical studies, generally implying in time and cost reduction regarding project development when compared to the experimental approach. Also, it can be a powerful tool in finding numerical solutions, especially when the analytical approach is prone to failure due to cumbersome expression evaluation or even when analytical expressions are missing.

Tu et al. (2018) mention that the reliance on the computational approach, especially when it involves complex fluids, is increasing even though analytical and experimental methods continue to be performed. For instance, a particular process can be evaluated using CFD to understand how the variables are expected to behave, which enables cost-effective design optimization studies and simulation of unfeasible experiments.

This work aims to discuss about CFD modeling and simulation applied to three different study cases: particle separation in a hydrocyclone, gas-wind interaction, and two-phase flow emission. It covers an analysis of each study case, as well as a brief description of recommended models. This thesis also illustrates different processing results and contributes to enhance the understanding of CFD simulation for specific applications.

1.3 Outline of the thesis

Chapter 2 describes the models used in the study cases in this work, including governing equations, turbulence models, and multiphase approaches. It also has a brief introduction to the simulation steps using commercial software.

Chapter 3 gives an overview of liquid-solid CFD simulations using the study case of a clay purification through a hydrocyclone process. It introduces the background of the study case and describes the different scenarios concerning design and process conditions to be evaluated. The Eulerian-Eulerian approach for multiphase flow is discussed, as well as the complete specifications and models. The CFD results are compared to experimental results, and further analyses of the equipment performance are carried out.

Chapter 4 describes a gas-gas interaction exemplified by a flammable gas emission in an open environment (gas-wind). It gives an overview of calculations for critical boundary conditions and performs several numerical experiments. These experiments vary wind speed and process variables for different flammable gases to obtain a detailed analysis of the interaction between gas-wind, which is further studied in terms of hazardous area classification.

Chapter 5 introduces gas-liquid simulations considering mass, heat, and momentum transfer between phases. This condition is exemplified by a two-phase flammable leakage, which requires the Eulerian-Lagrangian approach for multiphase flow. Particle tracking and phase interactions are addressed in this chapter. Also,

different discharge scenarios are evaluated, such as equilibrium and non-equilibrium releases.

1.4 Publications

The case studies in this work generated the following research articles:

GAMA, A.J.A.; NEVES, G.A.; BARROS, P.L.; NETO, A.T.P.; ALVES, J.J.N. Hydrocyclone performance for bentonite clay purification. *Chemical Engineering Research and Design*, v.161, p. 168-177, 2020. DOI: [10.1016/j.cherd.2020.07.005](https://doi.org/10.1016/j.cherd.2020.07.005)

BARROS, P.L.; LUIZ, A.M.; NASCIMENTO, C.L.; NETO, A.T.P.; ALVES, J.J.N. On the non-monotonic wind influence on flammable gas cloud from CFD simulations for hazardous area classification. *Journal of Loss Prevention in the Process Industries*, v.68, 104278, 2020. DOI: [10.1016/j.jlp.2020.104278](https://doi.org/10.1016/j.jlp.2020.104278)

Chapter 2

Computational Fluid Dynamics

Computational fluid dynamics is a research area where the main issue boils down to mathematical modeling of flow equations to predict fluid behaviors. The pre-processing, governing equations and models, and post-processing are briefly described in this chapter. It is important to mention that this work uses Ansys CFX as a software tool, therefore, some nomenclatures may be different elsewhere.

2.1 Pre-processing

Pre-processing is the initial step to develop a flow model. It covers the construction of the geometry and mesh. The geometry itself represents the computational domain, while the mesh is the subdivision of the domain into a finite number of control volumes. Meshing the geometry is of primary importance for solving CFD simulations because the quality of the mesh influences the accuracy and the stability of the solution. This work uses Ansys Design Modeler and Ansys Meshing to build geometry and grid, respectively.

2.2 Hydrodynamic equations

Governing equations for continuous phases are presented as following. They describe global mass conservation (Equation 2.1), momentum (Equation 2.2), and energy (Equation 2.3) (ANSYS CFX, 2015).

$$\frac{\partial \rho}{\partial t} + \nabla \cdot (\rho \vec{u}) = 0 \quad (2.1)$$

$$\frac{\partial(\rho \vec{u})}{\partial t} + \nabla \cdot (\rho \vec{u} \otimes \vec{u}) = -\nabla P + \nabla \cdot \mu(\nabla \vec{u} + (\nabla \vec{u})^T) + S_M \quad (2.2)$$

$$\frac{\partial(\rho h_{tot})}{\partial t} + \nabla \cdot (\rho \vec{u} h_{tot}) = \frac{\partial P}{\partial t} + \nabla \cdot (\lambda \nabla T) + \nabla \cdot \left(\mu \nabla \vec{u} + \nabla \vec{u}^T - \frac{2}{3} \nabla (\vec{u} \delta \vec{u}) \right) + S_E \quad (2.3)$$

For multicomponent scenarios, the individual mass conservation and mass fraction of component i (Y_i) are given by Equations 2.4 and 2.5, respectively. Also, Equation 2.6 represents a constraint in which the mass fractions must sum to unity.

$$\frac{\partial(\rho Y_i)}{\partial t} + \nabla \cdot (\rho \vec{u} Y_i) = \nabla \cdot (\Gamma_{M_{i_{eff}}} \nabla Y_i) + S_{MSi} \quad (2.4)$$

$$Y_i = \frac{\rho_i}{\rho} \quad (2.5)$$

$$\sum_{i=A,B,C}^{N_c} Y_i = 1 \quad (2.6)$$

2.3 Multiphase flows

Multiphase models are described by Eulerian-Eulerian (E-E) or Eulerian-Lagrangian (E-L) approaches. The main difference between them is that particulates are tracked throughout the fluid flow in E-L, also called as Lagrangian Particle Tracking model. This occurs by solving a set of ordinary differential equations in time for each computational particle and generating source terms that denote the particle influence on the continuous phase. The computational particles describe the average behavior of the dispersed phase by representing a sample of the actual number of particles and, consequently, avoiding extra computational time. The E-E approach, in turn, solves hydrodynamic equations for each phase, which may be continuous or dispersed. Therefore, it calculates complete global information for all phases, but it can be time-consuming for many particle sizes. In addition, the E-E multiphase model is preferred for simulations with a high concentration of particulates (ANSYS CFX, 2015).

2.3.1 Particle tracking

2.3.1.1 Particle displacement

The Lagrangian tracking encompasses the integration of particle paths through the discretized domain, and the generation of source terms to fluid mass, momentum, and energy equations. Particle displacement is calculated by the explicit Euler time stepping approach as shown in Equation 2.7 (ANSYS CFX, 2015):

$$x^i = x^{i-1} + u_p^{i-1} \delta t \quad (2.7)$$

where, u_p is particle velocity, δt is the time step, and i is the iteration number.

2.3.1.2 Momentum transfer

The particle momentum equation is calculated from the force balance that act on each particle, as stated by Newton's Second Law of motion (Equation 2.8):

$$m_p \frac{du_p}{dt} = F_R \quad (2.8)$$

where F_R is the resultant force on the particle. Throughout this work, two main forces are considered, namely buoyancy force (F_B) due to gravity and drag force (F_D).

$$F_B = \frac{1}{6} \pi d^3 (\rho_p - \rho_f) g \quad (2.9)$$

$$F_D = \frac{1}{2} \rho_f C_D A_F |u_f - u_p| (u_f - u_p) \quad (2.10)$$

A_F is the projected area of the particle in the direction of the flow, which is given by Equation 2.11.

$$A_F = \frac{1}{4} \pi d_p^2 \quad (2.11)$$

C_D is the drag coefficient, which is - in this work - calculated by Schiller Naumann model for sparsely distributed dispersed particles, as following:

$$C_D = \begin{cases} \frac{24}{Re} (1 + 0.15 Re^{0.687}), & \text{if } Re < 1000 \\ 0.44, & \text{if } Re > 1000 \end{cases} \quad (2.12)$$

$$Re = \frac{\rho_f |u_f - u_p| d_p}{\mu_f} \quad (2.13)$$

2.3.1.3 Heat transfer

This work takes into consideration the convective heat transfer, and latent heat transfer due to mass transfer as presented in Equation 2.14:

$$m_p C_p \frac{dT_p}{dt} = \pi d_p \lambda Nu (T_f - T_p) + \Delta H^{vap} \frac{dm_p}{dt} \quad (2.14)$$

where Nu is the Nusselt number given by Equation 2.15.

$$Nu = 2 + 0.6Re^{0.5} \left(\mu \frac{Cp}{\lambda} \right)^{1/3} \quad (2.15)$$

2.3.1.4 Mass transfer

The Liquid Evaporation Model is used in this study to describe the mass transfer from liquid to vapor phase. This model consists of two correlations (Equations 2.16-2.17) that depend on the particle thermodynamic condition in terms of the boiling point. For that matter, the particle is boiling if the vapor pressure (P_{vap}) is higher than the gaseous pressure (P_g).

$$\frac{dm_p}{dt} = - \frac{\pi d_p \lambda Nu (T_f - T_p)}{\Delta H^{vap}}, \quad se P_{vap} \geq P_g \quad (2.16)$$

$$\frac{dm_p}{dt} = \pi d_p \rho D Sh \frac{MW_c}{MW_g} \log \left(\frac{1 - X}{1 - X_g} \right), \quad se P_{vap} < P_g \quad (2.17)$$

Here X and X_g are the molar fractions in the droplet surface and in the gas phase.

2.3.2. Free surface model

This model is available for the Eulerian-Eulerian multiphase approach, and it is adequate for simulation where there is a well-defined interface between the phases. Hence, it is designed for two or more immiscible fluids. The momentum, mass, and heat transfer through the interface depend on the surface area of contact between the phases per unit volume ($A_{\alpha\beta}$). Equation 2.18 presents the interfacial area density between two phases for the free surface model:

$$A_{\alpha\beta} = |\nabla r_\alpha| \quad (2.18)$$

where r_α is the volume fraction of phase α .

2.3.3 Particle model

This model is also available for the Eulerian-Eulerian multiphase approach, and considers a continuous phase and a dispersed phase (dispersed fluid or solid) treated as an equivalent spherical particle. Therefore, the interfacial area density is given by the corresponding area of a spherical particle divided by its volume, which results in Equation 2.19.

$$A_{\alpha\beta} = \frac{6r_{\beta}}{d_{\beta}} \quad (2.19)$$

2.4 Turbulence model

CFD studies mainly focus on turbulent flows since it represents the majority of naturally occurring flows. These turbulent flows are inherently three-dimensional and unsteady while encompassing a wide range of scale motions (Zhiyin, 2015). In that way, direct numerical simulation (DNS) is the most accurate turbulent approach, which directly solves time-dependent Navier-Stokes equations combining it with a very fine mesh to capture all large and small scales. However, it requires a high computational effort, and it is normally not used for most engineering applications. On the other hand, Reynolds-averaged Navier-Stokes (RANS) considers averaged quantities, which are based on a statistical averaging procedure that describes a quantity by the sum of its mean value and a fluctuating term (Reynolds decomposition). This approach enables evaluating the fluid flow in the steady-state regime, and also allows considering two-dimensional domains. In Ansys CFX, the RANS turbulence models are classified as eddy viscosity models ($k - \varepsilon$, $k - \omega$, Shear Stress Transport) or Reynolds stress models. An alternative turbulence approach is large eddy simulation, which solves time-dependent Navier-Stokes equations for large eddies and models eddies smaller than the mesh by filtering in space.

2.4.1. Shear Stress Transport

Shear Stress Transport (SST) turbulence model is part of a set of two-equation models: one solves the turbulent kinetic energy, and the other determines the dissipation rate of turbulent kinetic energy. The main purpose of the SST model is to accurately predict the behavior of the boundary layer under a severe pressure gradient by accounting for the transport of turbulent shear stress (Menter, 2009). This turbulence model introduces blending functions that combine elements of $k - \varepsilon$ and $k - \omega$ models through a unified formulation, where $k - \omega$ is used close to the wall while $k - \varepsilon$ is used far from the wall. The transport equations are presented below:

$$\frac{\partial(\rho k)}{\partial t} + \nabla(\rho \vec{u}k) = \nabla \left[\left(\mu + \frac{\mu_t}{\sigma_{k3}} \right) \nabla k \right] + P_k - \beta' \rho k \omega \quad (2.20)$$

$$\frac{\partial(\rho\omega)}{\partial t} + \nabla(\rho\vec{u}\omega) = \nabla\left[\left(\mu + \frac{\mu_t}{\sigma_{\omega 3}}\right)\nabla\omega\right] + (1 - F_1)2\rho\frac{1}{\sigma_{\omega 2}\omega}\nabla k\nabla\omega + \alpha_3\frac{\omega}{k}P_k - \beta_3\rho\omega^2 \quad (2.21)$$

where P_k is the turbulence production due to viscous and buoyancy forces, μ_t is the turbulent viscosity given by Equation 2.22, and the coefficients of the new model are calculated by a linear combination of its corresponding coefficients as demonstrated by Equation 2.23. These coefficients of the turbulence model are defined in Table 2.1 (ANSYS CFX, 2015).

$$\mu_t = \frac{\rho a_1 k}{\max(a_1\omega, SF_2)} \quad (2.22)$$

$$\Phi_3 = F_1\Phi_1 + (1 - F_1)\Phi_2 \quad (2.23)$$

Table 2.1: Constant values for Shear Stress Transport model.

Constant	Value
β'	0.09
α_1	5/9
α_2	0.44
β_1	0.075
β_2	0.0828
σ_{k1}	2
σ_{k2}	1
$\sigma_{\omega 1}$	2
$\sigma_{\omega 2}$	1/0.856

The formulation of blending functions is of major importance for the success of SST turbulence model. These functions are based both on flow variables and the distance towards the closest surface (y), as presented below (ANSYS CFX, 2015):

$$F_1 = \tanh(\arg_1^4) \quad (2.24)$$

$$\arg_1 = \min\left(\max\left(\frac{\sqrt{k}}{\beta'\omega y}, \frac{500\nu}{y^2\omega}\right), \frac{4\rho k}{CD_{k\omega}\sigma_{\omega 2}y^2}\right) \quad (2.25)$$

$$CD_{k\omega} = \max\left(2\rho\frac{1}{\sigma_{\omega 2}\omega}\nabla k\nabla\omega, 1 \times 10^{-10}\right) \quad (2.26)$$

$$F_2 = \tanh(\arg_2^2) \quad (2.27)$$

$$\arg_2 = \max\left(\frac{2\sqrt{k}}{\beta'\omega y'}, \frac{500\nu}{y^2\omega}\right) \quad (2.28)$$

Curvature correction may also be applied to account for relevant curvature effects. This technique offers comparable accuracy to Reynolds Stress models with less computational effort for swirl dominated flows. The curvature correction for SST turbulence model (SST-CC) uses a production correction that acts as modifying the production term in curved surfaces.

2.4.2. Reynolds Stress Model

The Reynolds Stress Model (RSM) turbulence models solve transport equations for all six components of the Reynolds stress tensor ($\overline{\rho \mathbf{u} \otimes \mathbf{u}}$) and dissipation rate, which is based on the ε -equation in Ansys CFX (ANSYS CFX, 2015). These models may account for complex interactions in the flow field, such as the modeling of stress anisotropies. Anisotropic turbulence leads to average properties that depend on position and direction; hence, turbulent fluctuations may have directional preferences. The transport equation that calculates the individual Reynolds stresses ($\overline{\rho u_i u_j}$) is presented in Equation 2.29 for an isotropic formulation of the diffusion coefficients, and in Equation 2.30 for preserving the anisotropic diffusion coefficients.

$$\frac{\partial(\overline{\rho u_i u_j})}{\partial t} + \frac{\partial(U_k \overline{\rho u_i u_j})}{\partial x_k} = P_{ij} + \phi_{ij} + \frac{\partial}{\partial x_k} \left[\left(\mu + \frac{2}{3} c_s \rho \frac{k^2}{\varepsilon} \right) \frac{\partial \overline{u_i u_j}}{\partial x_k} \right] - \frac{2}{3} \delta_{ij} \rho \varepsilon \quad (2.29)$$

$$\frac{\partial(\overline{\rho u_i u_j})}{\partial t} + \frac{\partial(U_k \overline{\rho u_i u_j})}{\partial x_k} = P_{ij} + \phi_{ij} + \frac{\partial}{\partial x_k} \left[\left(\mu \delta_{kl} + c_s \rho \frac{k}{\varepsilon} \overline{u_k u_l} \right) \frac{\partial \overline{u_i u_j}}{\partial x_l} \right] - \frac{2}{3} \delta_{ij} \rho \varepsilon \quad (2.30)$$

P_{ij} is the index notation of \mathbf{P} that is the exact production term, ϕ_{ij} is the pressure-strain correlation, and ε is the dissipation rate calculated by Equation 2.31 for isotropic diffusion coefficients or Equation 2.32 for anisotropic formulation.

$$\frac{\partial(\rho \varepsilon)}{\partial t} + \frac{\partial(U_k \rho \varepsilon)}{\partial x_k} = \frac{\varepsilon}{k} (c_{\varepsilon 1} P - c_{\varepsilon 2} \rho \varepsilon) + \frac{\partial}{\partial x_k} \left[\left(\mu + \frac{\mu_t}{\sigma_\varepsilon} \right) \frac{\partial \varepsilon}{\partial x_k} \right] \quad (2.31)$$

$$\frac{\partial(\rho \varepsilon)}{\partial t} + \frac{\partial(U_k \rho \varepsilon)}{\partial x_k} = \frac{\varepsilon}{k} (c_{\varepsilon 1} P - c_{\varepsilon 2} \rho \varepsilon) + \frac{\partial}{\partial x_k} \left[\left(\mu \delta_{kl} + c_\varepsilon \rho \frac{k}{\varepsilon} \overline{u_k u_l} \right) \frac{\partial \varepsilon}{\partial x_l} \right] \quad (2.32)$$

The exact production term is written as following:

$$\mathbf{P} = -\rho(\overline{\mathbf{u} \otimes \mathbf{u}}(\Delta \mathbf{U})^T + (\Delta \mathbf{U})\overline{\mathbf{u} \otimes \mathbf{u}}) \quad (2.33)$$

The pressure-strain correlation is expressed based on the formulation below:

$$\phi_{ij} = \phi_{ij1} + \phi_{ij2} \quad (2.34)$$

$$\phi_{ij1} = -\rho\varepsilon \left(C_{s1} \mathbf{a} + C_{s2} \left(\mathbf{a}\mathbf{a} - \frac{1}{3} \mathbf{a} \cdot \mathbf{a} \delta \right) \right) \quad (2.35)$$

$$\begin{aligned} \phi_{ij2} = & -C_{r1} P \mathbf{a} + C_{r2} \rho k \mathbf{S} - C_{r3} \rho k \mathbf{S} \sqrt{\mathbf{a} \cdot \mathbf{a}} + C_{r4} \rho k \left(\mathbf{a} \mathbf{S}^T + \mathbf{S} \mathbf{a}^T - \frac{2}{3} \mathbf{a} \cdot \mathbf{S} \delta \right) \\ & + C_{r5} \rho k (\mathbf{a} \mathbf{W}^T + \mathbf{W} \mathbf{a}^T) \end{aligned} \quad (2.36)$$

$$\mathbf{a} = \frac{\overline{\mathbf{u} \otimes \mathbf{u}}}{k} - \frac{2}{3} \delta \quad (2.37)$$

$$\mathbf{S} = \frac{1}{2} (\nabla \mathbf{U} + (\nabla \mathbf{U})^T) \quad (2.38)$$

$$\mathbf{W} = \frac{1}{2} (\nabla \mathbf{U} - (\nabla \mathbf{U})^T) \quad (2.39)$$

where \mathbf{a} is the anisotropy tensor, \mathbf{S} is the strain rate and \mathbf{W} is the vorticity. Ansys CFX presents some variant models as Launder-Reece-Rodi (LRR) and Speziale-Sarkar-Gatski (SSG). The available standard Reynolds stress models are LRR-IP (LRR Reynolds Stress), LRR-QI (QI Reynolds Stress), and SSG, to which different model constants are applied (Table 2.2). Here, IP means Isotropisation of Production, and QI means Quasi-Isotropic (ANSYS CFX, 2015).

Table 2.2: RSM turbulence model constants.

Model	c_s	$c_{\varepsilon 1}$	$c_{\varepsilon 2}$	C_{s1}	C_{s2}	C_{r1}	C_{r2}	C_{r3}	C_{r4}	C_{r5}
LRR-IP	0.22	1.45	1.9	1.8	0	0	0.8	0	0.6	0.6
LRR-QI	0.22	1.45	1.9	1.8	0	0	0.8	0	0.873	0.655
SSG	0.22	1.45	1.83	1.7	-1.05	0.9	0.8	0.65	0.625	0.2

2.4.3. Large Eddy Simulation

Large eddy simulation (LES) is an inherently time-dependent approach that directly solves large eddies from filtered Navier-Stokes equations and models small scales. Most of the momentum transfer and turbulent mixing is due to the turbulent energy of large eddies, which are captured in detail from LES (Zhiyin, 2015). According

to Ansys CFX documentation, LES is mostly applied for research purposes and mainly for single-phase, single component, and non-reacting flow. It requires a high grid resolution and small timestep; thus, it is not practical for many engineering calculations (ANSYS CFX, 2015). The decomposition of flow variables here is in terms of resolved and unresolved parts, as written below:

$$f = \bar{f} + f' \quad (2.40)$$

where f is any flow variable, \bar{f} is the large scale part (filtered), and f' is the small scale part. The filtered Navier-Stokes equation is presented in Equation 2.41.

$$\frac{\partial(\rho\bar{U})}{\partial t} + \frac{\partial(\rho\bar{U}_i\bar{U}_j)}{\partial x_j} = -\frac{\partial\bar{p}}{\partial x_i} + \mu\frac{\partial^2\bar{U}_i}{\partial x_j\partial x_j} - \frac{\partial(\rho\tau_{ij})}{\partial x_j} \quad (2.41)$$

The sub-grid scale stresses, τ_{ij} , is given by Equation 2.42.

$$\tau_{ij} = \overline{u_i u_j} - \bar{U}_i \bar{U}_j \quad (2.42)$$

$$\overline{u_i u_j} = \bar{U}_i \bar{U}_j + \overline{\bar{U}_i u'_j} + \overline{\bar{U}_j u'_i} + \overline{u'_i u'_j} \quad (2.43)$$

This residual stress tensor must be modeled to achieve closure of the equations. Therefore, the Smagorinsky model relates the sub-grid scale tensor to the filtered strain rate (\bar{S}_{ij}), as presented in Equation 2.44.

$$\tau_{ij} = -2\nu_{SGS} \cdot \bar{S}_{ij} \quad (2.44)$$

The sub-grid scale viscosity, ν_{SGS} , is expressed in terms of length scale determined by the grid size ($\Delta = Vol^{1/3}$), and the velocity scale. This results in Equation 2.45 for the viscosity:

$$\nu_{SGS} = (C_s \Delta)^2 |\bar{S}| \quad (2.45)$$

$$|\bar{S}| = (2\overline{\bar{S}_{ij}\bar{S}_{ij}})^{1/2} \quad (2.46)$$

where Vol is the grid volume, and C_s is the Smagorinsky constant, which is an *a priori* input and changes depending on the flow type. This constant ranges from 0.065 to 0.25, and a value of 0.1 is often used (ANSYS CFX, 2015).

2.5 Post-processing

Post-processing is the final step of numerical simulations where fluid flow visualization takes place. A huge advantage of using CFD tools is covered in this step, which is to obtain data that cannot be measured in a real experiment. Here, several flow visualization studies can be done depending on the objective of the process: streamlines, plane profiles, contours, volume rendering, and charts are some of the possible analyses during post-processing.

Chapter 3

Liquid-solid flow in hydrocyclones

This chapter comprises a CFD modeling and simulation of liquid-solid flow in hydrocyclones. This study case evaluates the performance of a hydrocyclone for removing contaminant larger particles (silt fraction) in bentonite clays, which improves its commercial value. The CFD simulation enables a more comprehensive analysis of the hydrocyclone operation, subjecting it to different geometric configurations and operational conditions to improve the clay purification process. Also, the outcomes illustrate a complete flow visualization of the flow throughout the equipment, allowing the evaluation of variables that cannot be measured experimentally.

The study case aims to evaluate a steady-state Eulerian-Eulerian CFD model and compare the predicted results with experimental data. The model can be further used to analyze the clay purification for different conditions obtaining an empirical correlation that calculates the clay volume fraction as a function of the pressure drop. The simulations also provide a scale-up analysis to calculate the characteristic constant parameter of the hydrocyclone family.

3.1 Study case background

Clays are defined as natural, earthy, and low-granular materials that exhibit characteristic plasticity when they are moistened with water and harden when dried or fired (Guggenheim and Martin, 1995). Their chemical composition consists of aluminum, iron, and magnesium silicates. Furthermore, the physical properties vary according to their components and arrangement of the chemical groups. For this reason, there are a lot of denominations of clays depending on their applications, origins, and primary constituents, such as bentonite, china clay, fire clay, and refractory clay (Bergaya and Lagaly, 2006).

Bentonites, in turn, are described as sedimentary clays formed by devitrification followed by a chemical change in volcanic ashes, substantially composed of montmorillonite (Bergaya and Lagaly, 2006). Several varieties of bentonite clay are currently almost depleted, and newly discovered deposits contain bentonites with very high impurity content (silt fraction). In terms of size, the maximum equivalent diameter of clay fraction is $2\mu\text{m}$, while the silt fraction equivalent diameter varies between 2 to $20\mu\text{m}$, according to the International Soil Science Society (Murano et al., 2015).

Several industrial applications require a specific chemical composition that can only be achieved with decontamination processes (Favero et al., 2016). As the clay fraction (fine particles) becomes higher in the powder, the more significant is its commercial value, enhancing some of bentonite's physical properties that include cation-exchange capacity, free swelling volume, and apparent viscosity (Ozgen et al., 2009). Different separation process types have been studied for bentonite clay purification. At this point, it is worth mentioning that hydrocyclones are designed to separate solid particles over a size range of 4 to $500\mu\text{m}$ (Towler and Sinnott, 2013). This range indicates that hydrocyclone is recommended to obtain particles smaller than $4\mu\text{m}$ in the overflow stream, which suggests the usage of this equipment for clay purification by removing larger particles.

Hydrocyclone finds applications in many processes, and the effect of operating conditions on separation performance is evaluated by several researchers, as presented by Sabbagh et al. (2017), Cui et al. (2017), and Yang et al. (2019). Ni et al. (2019) state that enhanced-separation hydrocyclone technologies can be categorized into groups based on optimizing geometric parameters, which include: cylindrical section, inlet, vortex finder, underflow pipe, conical section, hydrocyclone inclination angle, and multi-hydrocyclone arrangement. These groups hold hydrocyclone parameters that are also essential for clay purification and are further studied to improve equipment performance (Wang and Yu, 2006; Ni et al., 2017).

The technique of computational fluid dynamics is widely employed to evaluate the separation efficiency of a hydrocyclone, and it is a valuable tool when experimental setup is unfeasible (Mokni et al., 2019). Typically, CFD simulations of hydrocyclones are performed to predict the flow field, understand the separation phenomena, and optimize geometric parameters of the equipment (Vakamalla et al., 2017). Further details concerning the CFD modeling of hydrocyclones have been widely discussed in the literature (Hong et al., 2015; Zhang et al., 2017). Ji et al. (2019) numerically

investigated the effect of feed inlet configurations for mitigating particle misplacement in hydrocyclones. Zhu et al. (2012) used direct numerical simulation with a Lagrangian multiphase flow model to study the influence of inlet velocities on the cut size, d_{50} , and separation efficiency in a mini-hydrocyclone. The equipment performance was also analyzed by Ye et al. (2019) varying the conical geometry and feed solids concentration, and resulting in an improved design and a reduced particle misplacement. Vakamalla et al. (2014) determined the effect of inclination to the vertical plane on the cut size diameter and efficiency curves based on numerical and experimental methods. Tang et al. (2015) presented an optimal configuration of the vortex finder to obtain a high separation sharpness through a design of experiments. Zhang et al. (2019) determined the hydrocyclone separation performance by varying underflow diameter and feed size distribution to evaluate their interaction, ensuring that adverse effects due to inlet disturbances are mitigated.

3.1.1 Hydrocyclone fundamentals overview

Hydrocyclones have been designed for mechanical separation of dispersed particles in a fluid, and they are an alternative process for bentonite purification. This equipment has a low maintenance cost, high market availability, and great versatility. There are two output streams in the hydrocyclone: the overflow, which concentrates lighter particles, and the underflow that concentrates coarser particles (Figure 3.1). Particle classification is governed by a balance between gravitational, centrifugal, and drag forces (Cullivan et al., 2004). The tangential feed intensifies the centrifugal force causing the particles to experience a strong outward radial acceleration. Centrifugal force pushes the heavier particles to the wall, and the gravitational force promotes a downward-swirl movement towards the bottom of the equipment (apex). The drag force pulls the lighter particles upwards, and the particles flow out through the hydrocyclone vortex finder (Swain and Mohanty, 2013). The particle movement in the radial direction due to centrifugal forces determines the separation efficiency of coarse particles, and the recovery of fine particles is mostly controlled by the reversion flow effect.

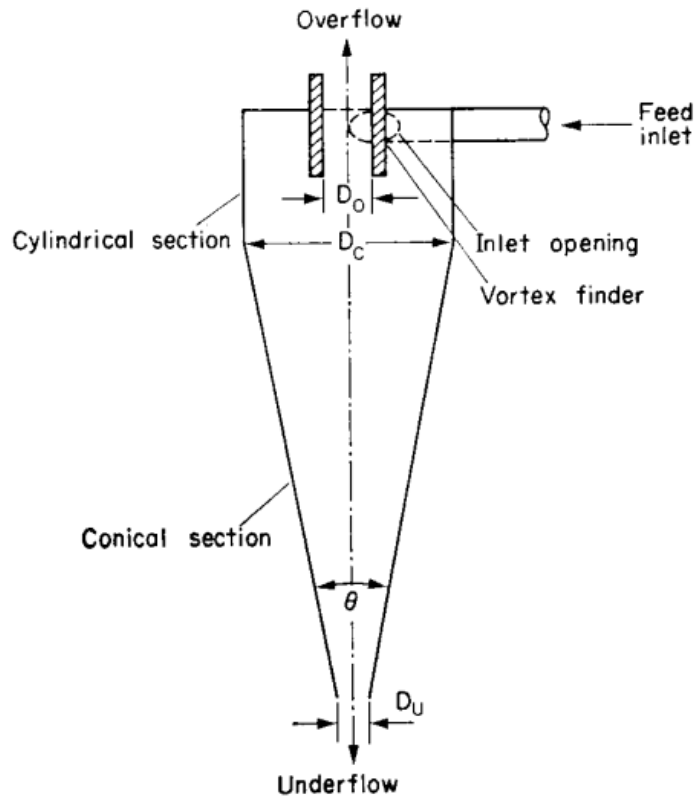


Figure 3.1: Principal features of the hydrocyclone (Bradley, 1965)

The global separation efficiency is defined as the fraction of particles fed to the hydrocyclone that are collected in the underflow, and so is the granulometric efficiency for a given particle size. These are important parameters for hydrocyclone performance evaluation and are calculated according to Equations 3.1 and 3.2 (Silva *et al.*, 2009). Moreover, the reduced global efficiency, defined by Equation 3.3, is used to evaluate the global separation performance eliminating the liquid-split effect (Equation 3.4) (Svarovsky, 1984). Analogously, the reduced grade efficiency can be calculated from Equation 3.5 to evaluate the hydrocyclone separation efficiency.

$$E_T = \frac{W_u}{W_f} \quad (3.1)$$

$$E_G^i = E_T \frac{dx_u}{dx_f} \cong E_T \left(\frac{x_u^{i+1} - x_u^i}{x_f^{i+1} - x_f^i} \cdot \frac{d^{i+1} - d^i}{d^{i+1} - d^{i-1}} + \frac{x_u^i - x_u^{i-1}}{x_f^i - x_f^{i-1}} \cdot \frac{d^i - d^{i-1}}{d^{i+1} - d^{i-1}} \right) \quad (3.2)$$

$$E_T' = \frac{E_T - R_L}{1 - R_L} \quad (3.3)$$

$$R_L = \frac{Q_u^L}{Q_f^L} \quad (3.4)$$

$$E_G^{i'} = \frac{E_G^i - R_L}{1 - R_L} \quad (3.5)$$

As a matter of fact, the hydrocyclone process purpose may be varied. One of them is the solids classification aiming at achieving particles at the overflow below a specific diameter. In general, this measurement is related to the hydrocyclone cut diameter. Cut diameter is defined as the particle diameter for which the grade efficiency is 50%, and it is an important parameter to analyze the equipment performance. An additional performance variable is the sharpness of separation, α , which indicates the degree of particle separation (Equation 3.6). It means that for a separation sharpness equals 1, the equipment splits perfectly with respect to the cut size diameter.

$$\alpha = \frac{d_{75}}{d_{25}} \quad (3.6)$$

3.1.2 Air Core

The swirling movement inside the hydrocyclone creates a low-pressure zone in the center of the equipment, sucking air from the open exits and creating an air core. This leads to hydrocyclone inefficiency, which requires a higher inlet pressure to maintain an adequate particle separation. For instance, air-core may exist as a continuous or semicontinuous liquid-air interface, and it can even do not occur. Ghodrati et al. (2013) show that these scenarios mainly depends on geometrical parameters and solids' concentration. Their results indicate that for small hydrocyclones, geometrically proportional to experimental studies from Hsieh and Rajamani (1988), there is no air-core formation. Instead, a small amount of air entrains from the overflow for low solids' concentration operation. The present work also investigates the potential air-core formation from a transient water-air simulation, which will be discussed later in this chapter.

3.1.3 Plitt model

Empirical correlations such as Plitt or Lynch models are presented in the literature to provide an analysis of the equipment performance (Swarovsky, 1984).

These models may be applied to obtain information about the hydrocyclone operation without additional experimental data. Plitt model, in fact, was obtained from experiments of equipment with specific design proportions, thus, it may not accurately represent all hydrocyclones (Swarosvky, 2001). The following equations define the reduced cut size diameter, pressure drop, and volume split according to Plitt's empirical correlation.

$$d'_{50} = \frac{50.5 D_H^{0.46} D_f^{0.6} D_o^{1.21} \mu^{0.5} \exp(0.063 C_s)}{D_u^{0.71} H^{0.38} Q^{0.45} (\rho_s - \rho)^{0.5}} \quad (3.7)$$

$$\Delta P = \frac{1.88 Q^{1.78} \exp(0.0055 C_s)}{D_H^{0.37} D_f^{0.94} H^{0.28} (D_u^2 + D_o^2)^{0.87}} \quad (3.8)$$

$$S = \frac{1.9 \left(\frac{D_u}{D_o}\right)^{3.31} H^{0.54} (D_u^2 + D_o^2)^{0.36} \exp(0.0054 C_s)}{H^{0.24} D_H^{1.11}} \quad (3.9)$$

Here, D_H , D_f , D_o , D_u , H (cm) are geometric parameters, Q (l/min), P (kPa), C_s (%) are inlet conditions, ρ_s and ρ (g/cm³) are physical properties. The reduced grade efficiency follows Rosin-Rammler distribution and can be described by Equation 3.10.

$$E_G^{i'} = 1 - \exp\left(-\ln(2) \left(\frac{d_i}{d'_{50}}\right)^m\right) \quad (3.10)$$

$$m = 1.08 \exp\left(0.58 - 1.58 \left(\frac{S}{S+1}\right) \left(\frac{D_H^2 H}{Q}\right)^{0.15}\right) \quad (3.11)$$

3.1.4 Scale-up

Obtaining scale-up parameters allows making rapid predictions concerning hydrocyclone design and performance. Therefore, to extend the results of the micro-hydrocyclone to any hydrocyclone from the same family (same geometry proportions), the constant K of a semi-theoretical design equation must be determined from Equation 3.12 (Bradley, 1965). Here, the solids' concentration is small so that its effect is not considered, and K is specific for each hydrocyclone family ($K_{\text{industrial}}=K_{\text{prototype}}$). Moreover, scaled-up hydrocyclones also may present dynamic similarity, which implies equal particle separation so that $d_{50\text{industrial}}=d_{50\text{prototype}}$.

$$\frac{d'_{50}}{D_H} = K \left(\frac{D_H \mu}{Q_F (\rho_p - \rho_L)} \right)^{1/2} \quad (3.12)$$

From the dimensionless analysis, the product between the Stokes and Euler's numbers is constant, and Equation 3.13 is obtained as a result (Ortega-Rivas, 2012):

$$D_{HI} = D_{HM} \left(\frac{Q_I}{Q_M} \right)^{\frac{1}{3}} \quad (3.13)$$

where D_{HI} and D_{HM} are the industrial and prototype hydrocyclone diameter, respectively. Q_I and Q_M are the volumetric flow rate for industrial and prototype equipment.

Empirical correlations, as previously demonstrated, can also represent the hydrocyclone family. In this case, if the correlation is adequate, more information can be obtained about the hydrocyclone operation, such as the reduced cut size diameter, pressure drop, volume split, and efficiency curve.

3.2 Experimental setup

The flowchart in Figure 3.2 shows an overview of the experimental setup used as a source of comparison in this study. The clay was initially processed by drying, crushing, milling, and screening, as discussed by Gama et al. (2018). Physical and mineral characterization of the bentonite sample was carried out at the Materials Engineering Department's Laboratory of Characterization at the Federal University of Campina Grande. The characterization was obtained by analyses of X-ray diffraction, energy-dispersive X-ray spectroscopy, and laser diffraction spectroscopy.

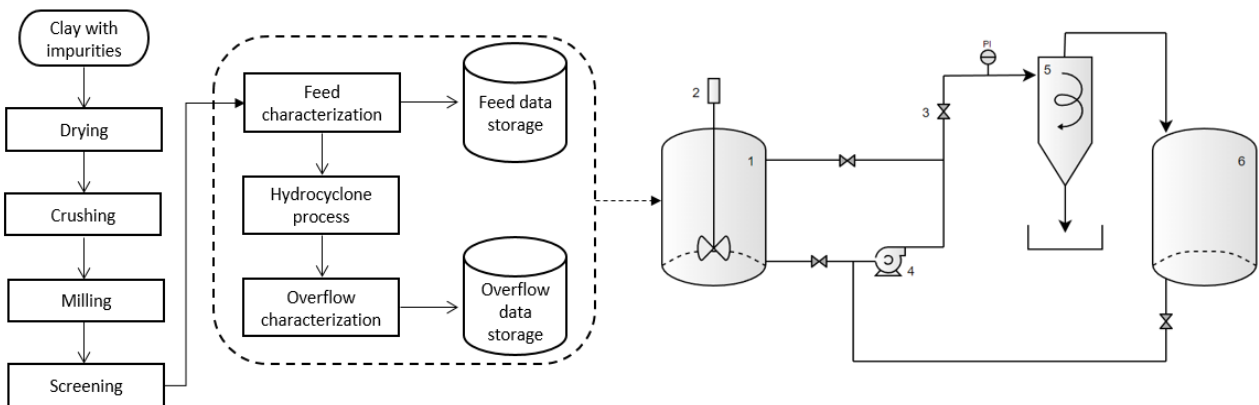


Figure 3.2: Flow diagram for the experiment and experimental setup. 1) Reservoir containing the feed clay, 2) stirrer, 3) pressure valve control, 4) centrifugal pump, 5) hydrocyclone, and 6) reservoir containing the overflow product.

The setup of the hydrocyclone experiment includes the following elements – 1) a reservoir that contains the clay dispersion to be treated, 2) a stirrer to ensure good feed mixing, 3) a valve for inlet pressure adjustment, 4) a centrifugal pump, 5) a hydrocyclone, and 6) a reservoir for the dispersion obtained in the overflow. The feed clay sample consisted of 4 wt.% of solids dispersed in water ($\rho_L=997 \text{ kg m}^{-3}$ and $\mu_L=8.9 \times 10^{-4} \text{ Pa s}$). The granulometric analysis indicated 13 particles of different mean diameters with individual feed volume fraction stated in Table 3.1. Also, from Table 3.1, the calculated volume average particle size in the feed is $5.67 \mu\text{m}$.

The chemical composition in the feed consists mostly of SiO_2 and Al_2O_3 . SiO_2 is present in the tetrahedral sheet of clay minerals as well as free silica in feldspar and mica, which is encountered mainly in silt particles. Al_2O_3 , which is primarily found in clay particles, comes from tetrahedral and octahedral layers, and accessory minerals, such as mica and feldspar. Feed analysis also indicated the presence of MgO and CaO , which are derived from dolomite and calcium carbonate, respectively, and iron oxide (Fe_2O_3) derived from smectite tetrahedral layers, goethite, ilmenite, and smectite clay minerals. According to this information, the density of solid particles in the range of $0 \mu\text{m} < d_p \leq 2 \mu\text{m}$ was estimated at around 2420.0 kg/m^3 , whereas the density of solid particles with diameters larger than $2 \mu\text{m}$ was set to 2650.0 kg/m^3 .

Table 3.1: Volume fraction of the particles in the feed.

Particle diameter (μm)	Volume fraction ($\times 10^5$)	Cumulative volume fraction (%)
0.04	1.47	0.05
0.07	1.87	0.18
0.10	7.42	0.28
0.25	19.23	1.09
0.50	32.84	2.64
0.75	48.09	5.12
1.00	128.53	8.54
2.00	195.27	20.89
3.00	194.70	32.50
4.00	191.20	44.78
5.00	352.08	55.96
10.00	358.93	87.98
20.00	97.96	100.00

3.3 CFD model

The mathematical model is based on the laws of conservation of mass and linear momentum for each phase considering isothermal heat transfer at a steady-state regime, solved by ANSYS® CFX 16.1 package. The Eulerian-Eulerian approach in which both the continuous and dispersed phases are considered fully interpenetrating was used, and also particle model for the dispersed fluids was applied. Water was defined as the continuous phase, and the dispersed phases consisted of 13 dispersed fluids of different equivalent diameters, resulting in a total of 14 phases in the simulations. This model considered the interphase momentum transfer due to buoyancy and drag force, and the drag coefficient was calculated by the Schiller Naumann model (ANSYS, 2015).

The dispersed phases were assumed to be inviscid, and particle-particle interactions were neglected due to low solid concentration. A primary comparative analysis between turbulence models was performed to verify the flow field results and to determine an adequate model for this study. For instance, it was analyzed isotropic and anisotropic turbulence models, which concerns to capture the asymmetries due to

high turbulent flow. Shear-stress transport (SST), SST with curvature correction (SST-CC), Reynolds stress model (RSM-LRR), and large eddy simulations (LES) were considered in this study.

Table 3.2 presents the boundary conditions used in this study. Regarding solution setup, it was used the high resolution advection scheme, a physical time step of 0.01s, and a residual target of 1×10^{-4} for global root mean square (RMS).

Table 3.2: Boundary conditions for the hydrocyclone study case.

Location	Boundary Condition
Tangential inlet	Inlet: Pressure (every phase share the same inlet pressure) and volume fraction of each phase were specified at this boundary
Hydrocyclone Wall	Wall: Non-slip condition for the liquid phase and free slip condition for particle phases
Underflow and Overflow	Outlet: Pressure was specified at this boundary (atmospheric pressure), and a flow direction normal to boundary condition was determined.

A set of configurations varying geometric parameters and inlet pressure (Table 3.3) was used for the numerical simulations. Configurations 1 to 4 were used for model verification, configurations 5 to 9 to evaluate the inlet pressure effect, and configurations 10 to 13 to analyze the effect of overflow and underflow diameters at a constant inlet pressure.

Table 3.3: Configuration of the simulations.

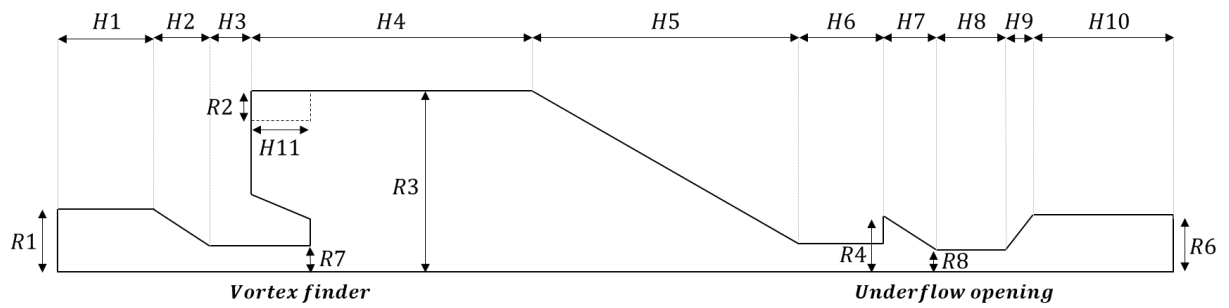
Configuration	Underflow opening (mm)	Vortex finder diameter (mm)	Inlet pressure (bar)
1	3.0	6.0	3.0
2	3.0	6.0	4.0
3	5.0	6.0	3.0
4	5.0	6.0	4.0
5	5.0	6.0	10.0
6	5.0	6.0	12.5
7	5.0	6.0	15.0
8	5.0	6.0	20.0
9	5.0	6.0	30.0
10	2.0	6.0	30.0
11	6.0	6.0	30.0
12	6.0	4.5	30.0
13	6.0	2.0	30.0

3.3.1 Air core prediction model

The CFD model to evaluate the air core formation used a free surface model to predict the liquid-air interface. Both water and air were set as continuous phases, and the presence of the solid particles was neglected. As the air core is inherently time-dependent, a transient regime was set with a time step of 0.01s, which is approximately 10 times less than the hydrocyclone residence time. For the turbulence model, it was used large eddy simulation (LES), which solves large eddies. Also, the boundary condition at the underflow and overflow was changed to an opening condition to account for the possible air entrainment from the open exits.

3.3.2 Geometry

The RWK-42L hydrocyclone model manufactured by Netzsch AWK is used in this study case. Figure 3.3 presents the dimensions of the hydrocyclone model, including its hopper. The hydrocyclone geometry was generated by a sketch revolution using ANSYS DesignModeler® (Figure 3.4). The vortex finder diameter (R7) and underflow opening (R8) were varied to search for a design that results in a higher volume fraction of particles smaller than or equal to $2\mu\text{m}$ (clay fraction) in the overflow.



Dimension	H1	H2	H3	H4	H5	H6	H7	H8	H9	H10	H11
Value (mm)	50	60	12.5	55	55	15	30	75	25	50	7.5

Dimension	R1	R2	R3	R4	R5	R6
Value (mm)	7.5	2.5	10	6	2	6

Figure 3.3: RWK-42L hydrocyclone dimensions.

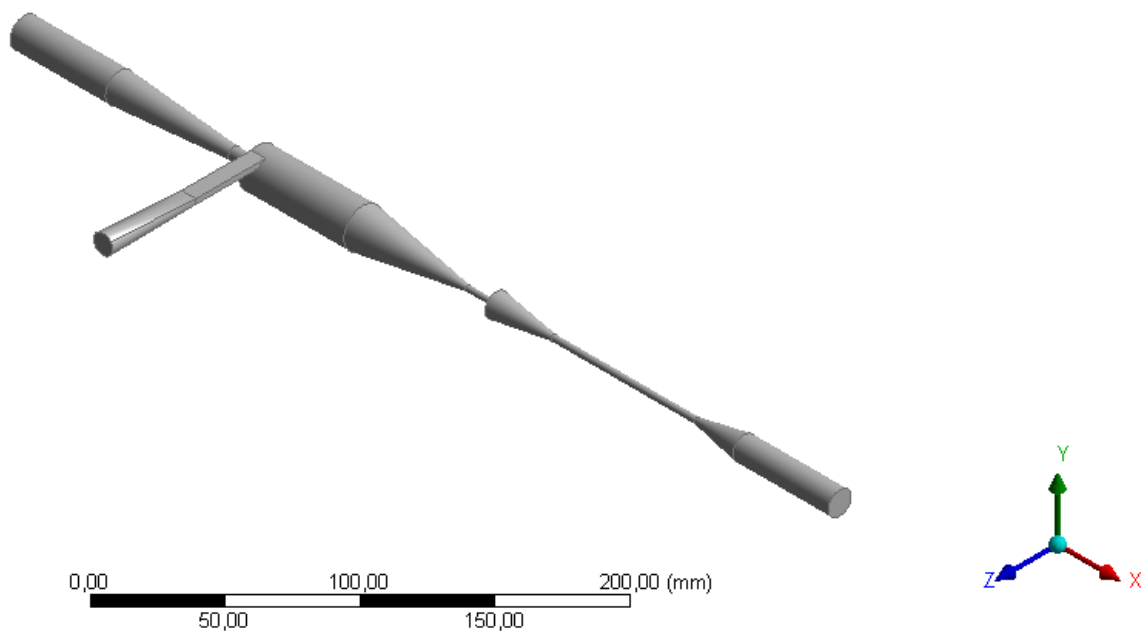
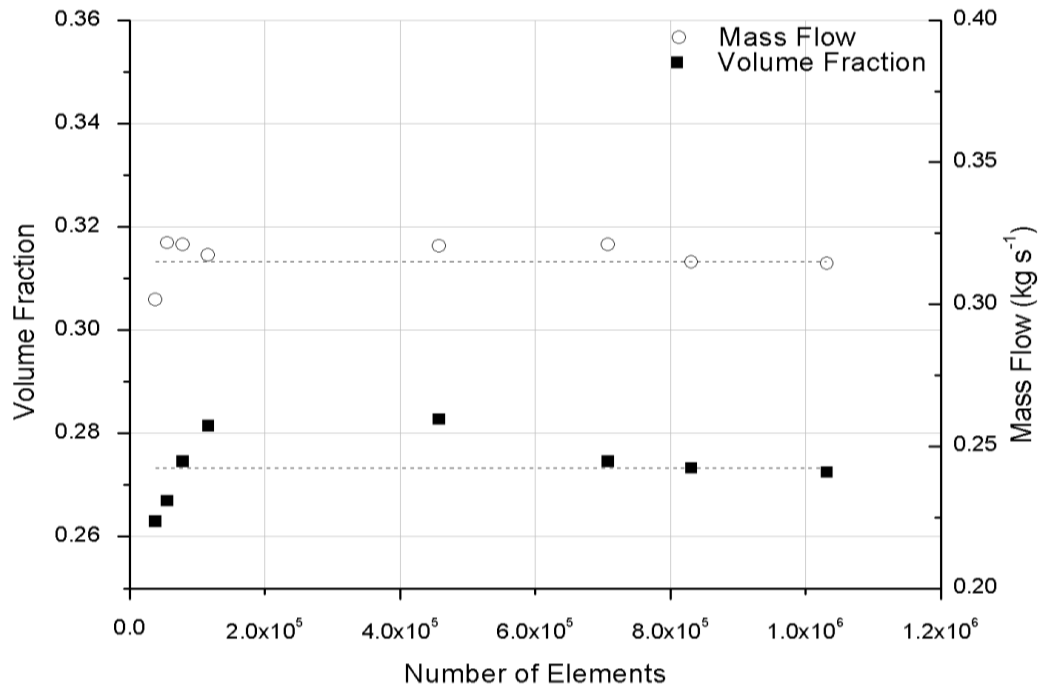


Figure 3.4: Isometric view of the geometry.

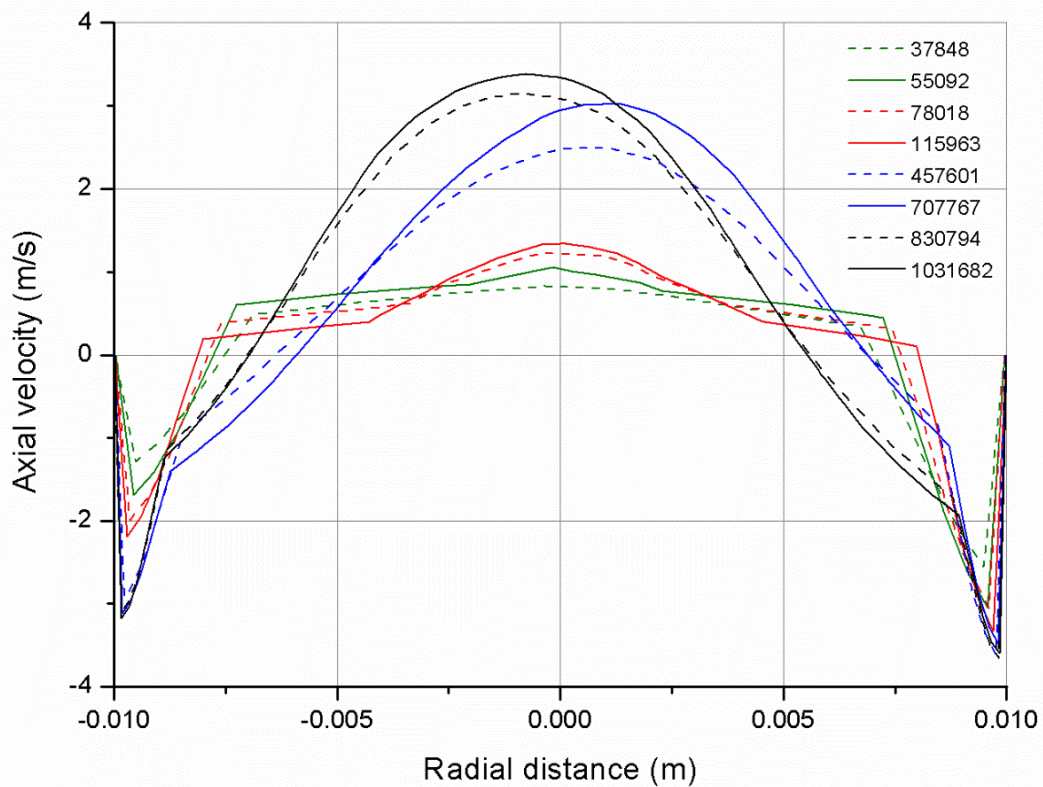
3.3.3 Grid independence study

ANSYS Meshing[®] package was used for mesh generation, and a mesh-independency study was performed by constructing different mesh refinements in the range of 37,848-1,031,682 elements. The predicted recovery of fine particles in the overflow and feed mass flow for each unstructured grid is presented in Figure 3.5(a). The last three simulation results of volume fraction and mass flow are sufficiently close (difference<3%), which means that the results for mesh grids greater than 707,767 are

already independent of the number of elements. Figure 3.5(a) also shows that the mass flow rate is less sensitive to mesh refinement than volume fraction; it happens because the mass flow calculated at the hydrocyclone inlet depends on pressure drop, which is constant for the base case scenario used in the mesh-independency study while the recovery of fine particles depends on internal flow structure. Figure 3.5(b) presents the grid independence study in terms of the flow field in an axial position at the cylindrical part of the hydrocyclone. The mesh with 830,794 elements shows a similar axial velocity profile compared to the most refined grid, therefore it is used in the present simulations.



(a)



(b)

Figure 3.5: Grid independence test for (a) volume fraction in the overflow and feed mass flow; (b) axial velocity profile.

3.4 Results

3.4.1 Air core results

Firstly, the results from the air core prediction are necessary to determine if this phenomenon has a significant influence on the hydrocyclone analyzed in the present study. The geometry was considered both with and without the hopper to evaluate its effect. Figures 3.6 and 3.7 show the axial plane profiles of air volume fraction at different times for each geometry. Figure 3.5 demonstrates that air is entrained from both exits into the equipment but does not create a continuous liquid-air interface throughout the hydrocyclone. Figure 3.7, in turn, illustrates that when the hopper is absent, there is no air in the underflow area whatsoever. These outcomes are in accordance with the literature (Ghodrat *et al.*, 2013), in which only a small amount of air is observed in the overflow area for simulations without hopper.

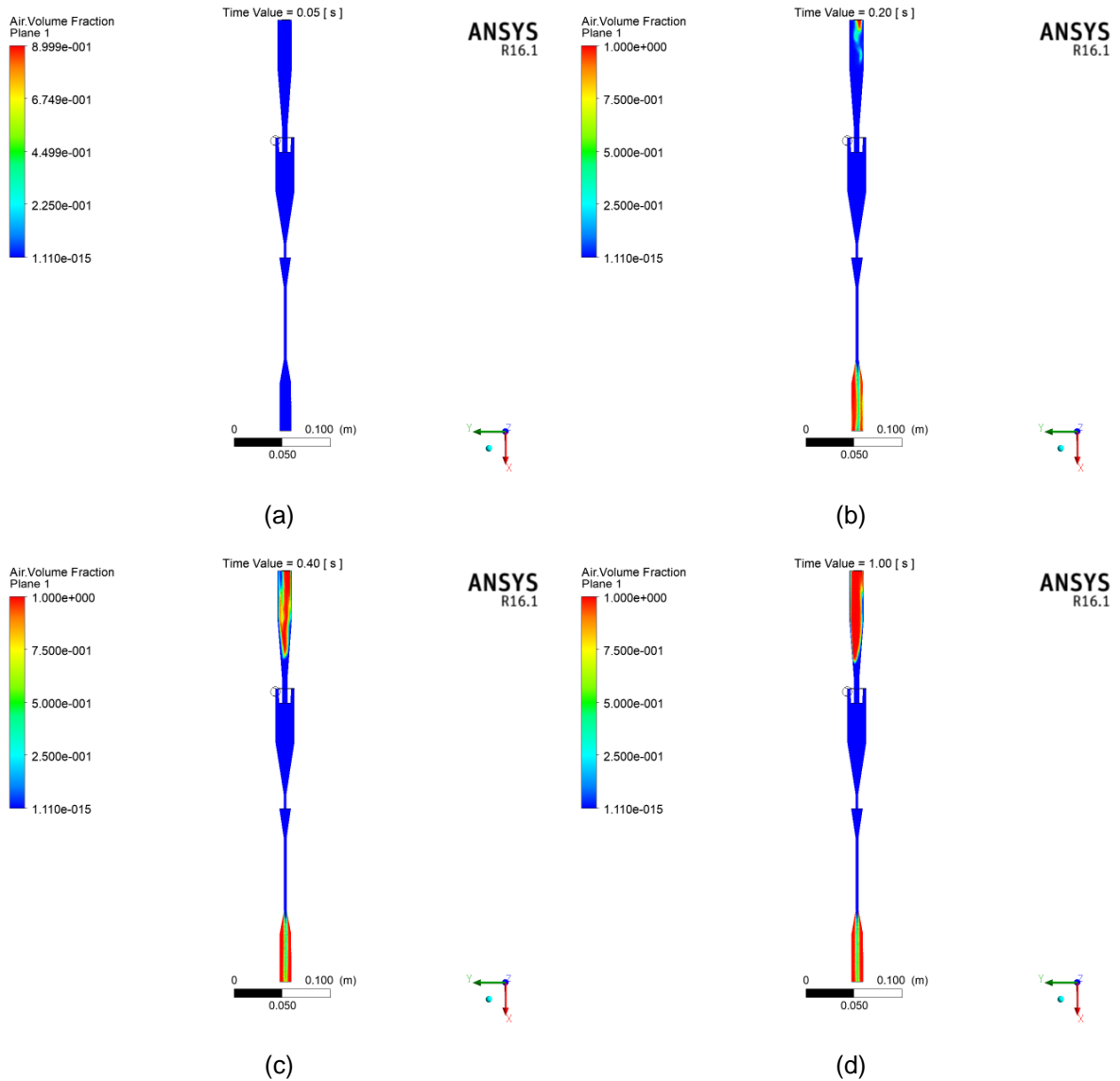
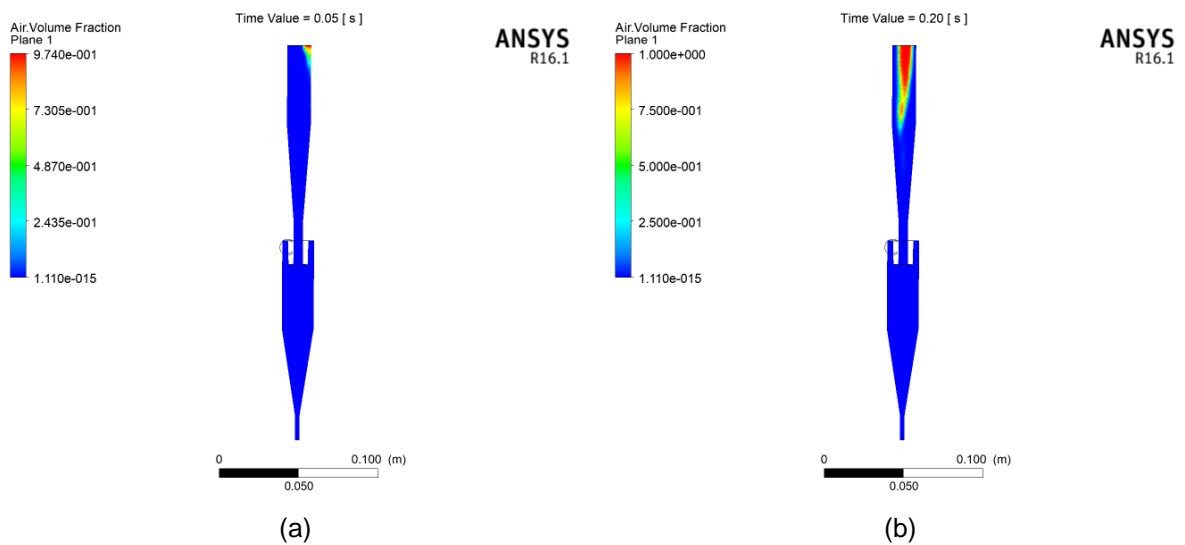


Figure 3.6: Air volume fraction profile for hydrocyclone with an attached hopper at (a) 0.05s; (b) 0.2s; (c) 0.4s; (d) 1s.



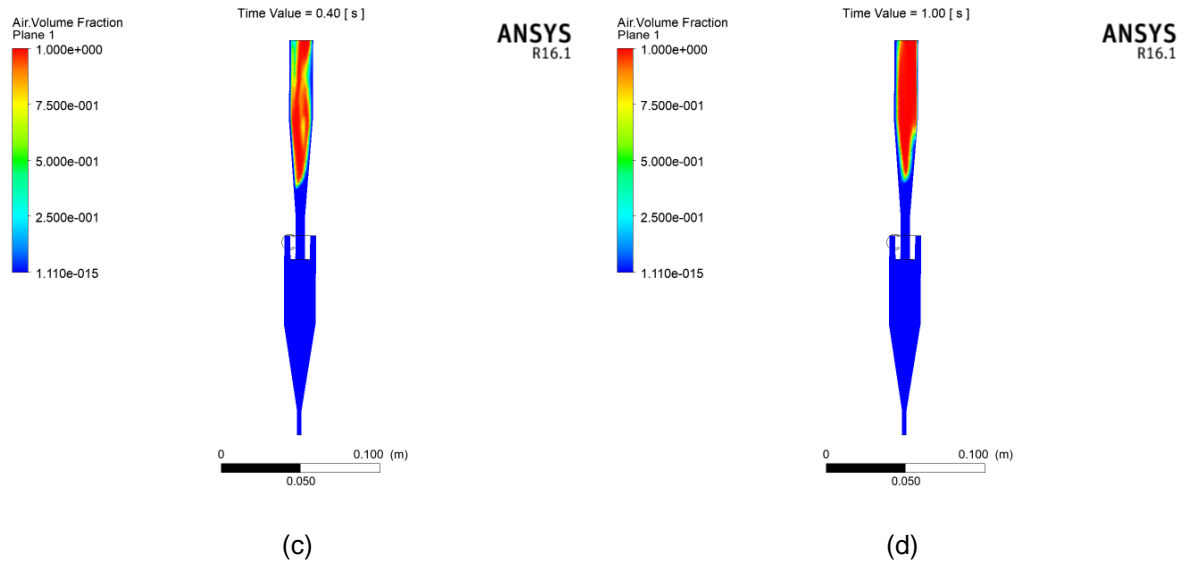


Figure 3.7: Air volume fraction profile for hydrocyclone without an attached hopper at (a) 0.05s; (b) 0.2s; (c) 0.4s; (d) 1s.

In the experiment setup conducted by Gama *et al.* (2018), the overflow is not an open exit. In fact, it is sealed with water in a reservoir. Therefore, the air core can be further neglected in the simulations.

3.4.2 CFD model verification

Experimental granulometric analyses by Gama *et al.* (2018) were used to verify the CFD model of the hydrocyclone. The concentration of solids at the inlet was kept constant at 4 wt.%, which was the same value used in experimental tests. The measured volume fraction values of particles in the overflow were compared to the predicted values from CFD simulations. Tables 3.4-3.7 show the volume fraction results and the relative error between experiments and CFD outcomes for configurations 1-4 from Table 3.3. Although it can be observed a high relative error in some cases, the granulometric curves (Figure 3.8) resulting from these data illustrate comparable results between them. This is emphasized by including a 95% confidence interval, represented by the dashed lines. Moreover, Figure 3.8 presents predicted overflow efficiency results for each case, as well as the liquid ratio. From these outcomes, it can be observed a high reduced cut size diameter, which is not as effective for clay purification. Thus, other configurations must indeed be analyzed.

Table 3.4: CFD model verification against experimental data ($R_7=6\text{mm}$, $R_8=3\text{mm}$, $P=3\text{bar}$).

Particle diameter (μm)	Predicted volume fraction (%)	Experimental volume fraction (%)	Relative error (%)
0.04	0.09	0.13	28.7
0.07	0.11	0.16	29.2
0.1	0.45	0.61	26.3
0.25	1.17	1.55	24.8
0.5	1.99	2.54	21.5
0.75	2.91	3.56	18.2
1	7.78	9.25	15.9
2	11.78	13.50	12.7
3	12.77	12.37	3.3
4	12.44	11.47	8.5
5	22.67	19.40	16.9
10	21.41	19.64	9.0
20	4.43	5.72	22.5

Table 3.5: CFD model verification against experimental data ($R_7=6\text{mm}$, $R_8=3\text{mm}$, $P=4\text{bar}$).

Particle diameter (μm)	Predicted volume fraction (%)	Experimental volume fraction (%)	Relative error (%)
0.04	0.09	0.13	28.4
0.07	0.11	0.16	28.9
0.1	0.45	0.62	26.6
0.25	1.17	1.58	25.7
0.5	2.00	2.59	22.9
0.75	2.92	3.64	19.6
1	7.81	9.45	17.3
2	11.82	13.87	14.8
3	12.81	12.83	0.1
4	12.45	11.87	4.9
5	22.65	19.81	14.3
10	21.20	18.86	12.4
20	4.51	4.59	1.6

Table 3.6: CFD model verification against experimental data ($R_7=6\text{mm}$, $R_8=5\text{mm}$, $P=3\text{bar}$).

Particle diameter (μm)	Predicted volume fraction (%)	Experimental volume fraction (%)	Relative error (%)
0.04	0.09	0.17	43.5
0.07	0.12	0.21	42.2
0.1	0.47	0.77	38.5
0.25	1.22	1.88	35.1
0.5	2.08	3.06	31.9
0.75	3.05	4.36	30.0
1	8.14	10.89	25.3
2	12.27	15.16	19.0
3	13.24	13.10	1.1
4	12.81	11.62	10.2
5	23.15	18.32	26.3
10	20.19	16.74	20.7
20	3.17	3.72	14.6

Table 3.7: CFD model verification against experimental data ($R_7=6\text{mm}$, $R_8=5\text{mm}$, $P=4\text{bar}$).

Particle diameter (μm)	Predicted volume fraction (%)	Experimental volume fraction (%)	Relative error (%)
0.04	0.09	0.18	47.4
0.07	0.12	0.23	47.6
0.1	0.48	0.82	41.7
0.25	1.24	2.05	39.6
0.5	2.11	3.23	34.6
0.75	3.09	4.36	29.0
1	8.26	10.88	24.1
2	12.44	15.42	19.3
3	13.39	13.37	0.1
4	12.92	11.68	10.7
5	23.26	17.88	30.1
10	19.83	16.23	22.2
20	2.76	3.65	24.2

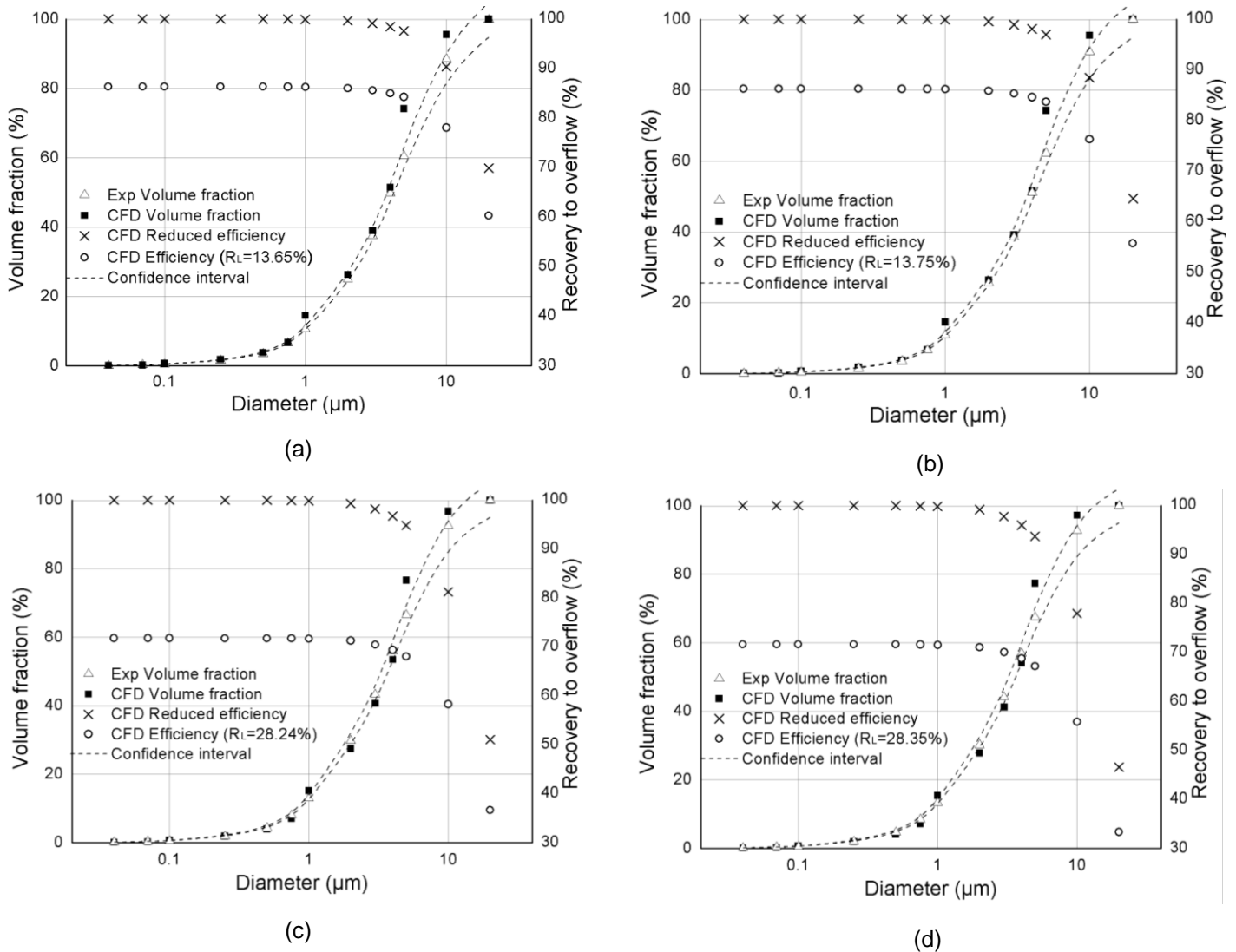


Figure 3.8: Overflow granulometric efficiency and cumulative volume fraction of fine particles for (a) configuration 1; (b) configuration 2; (c) configuration 3; (d) configuration 4.

The model was also verified in terms of turbulence models for configuration 1, as shown in Figure 3.9. Both granulometric curves and flow field profiles in a fixed axial position (157.5mm distant from the overflow exit) at the cylindrical body are similar for all turbulence models. However, the recovery to underflow presents major differences for larger particles when considering large eddy simulation. Higher efficiency for larger particles implies greater mean diameter reduction in the overflow (17.67% for LES compared to 6.23% from experimental data). Based on this, Figure 3.9(b) shows that the SST-CC turbulence model results in a mean diameter closer to the experiment (1.51% relative error) and is further considered in this work.

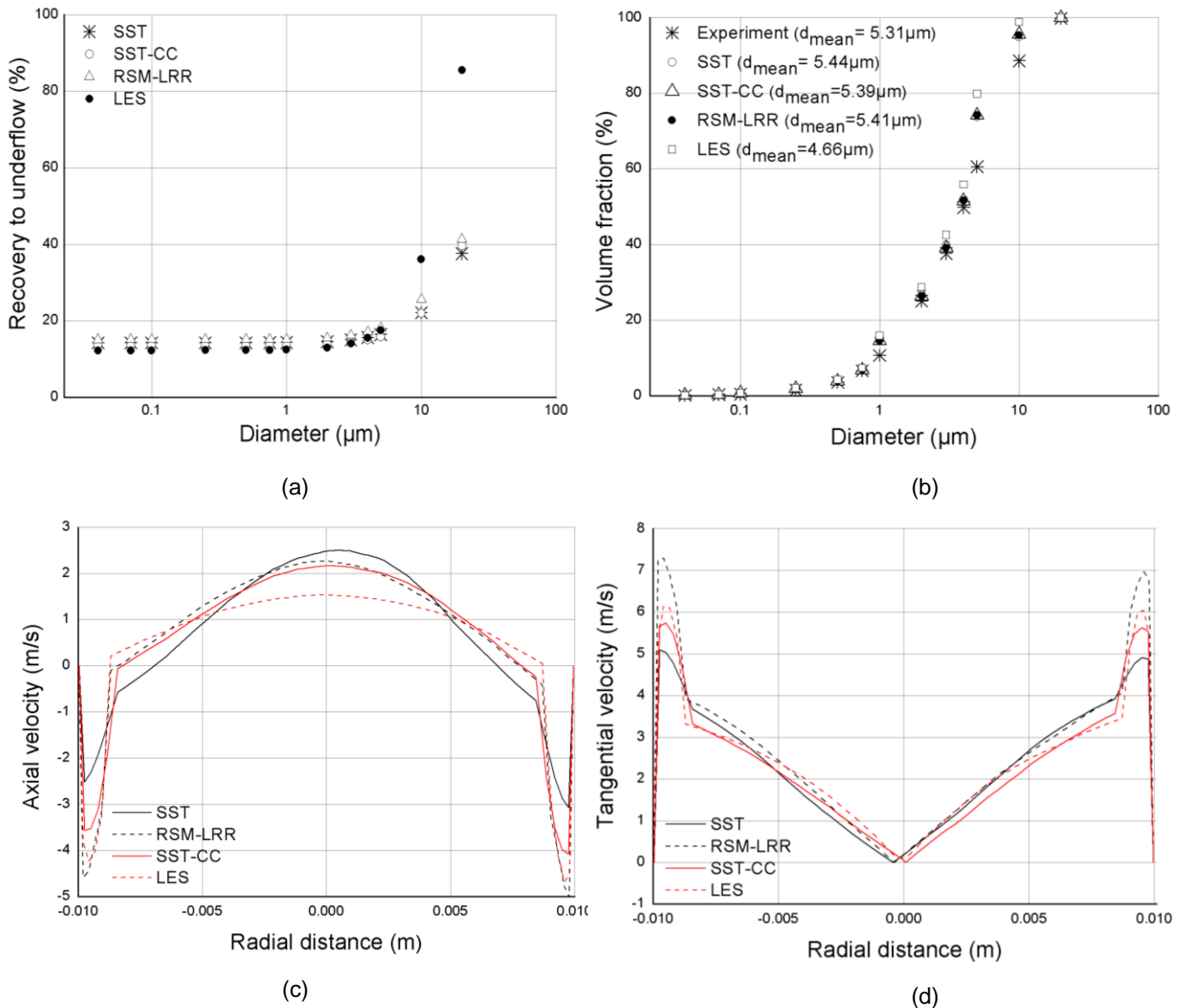


Figure 3.9: Comparison of turbulence models for (a) granulometric underflow efficiency; (b) cumulative volume fraction; (c) axial velocity; (d) tangential velocity.

3.4.3 CFD model utilization

The hydrocyclone performance was initially measured from the accumulated volume fraction of fine clay particles that reached the overflow for each configuration. It was analyzed because the higher the volume fraction of fine particles in the overflow, the more valuable is the overflow product. Table 3.8 shows these predicted results along with the mean diameters in the overflow, its reduction compared to the inlet mean diameter, and the liquid ratio.

Table 3.8: Predicted volume fraction of the fine particles and their mean diameters in the overflow.

Configuration	Accumulated volume fraction (%)	Mean diameter (μm)	Mean diameter reduction (%)	Liquid ratio (%)
1	26.28	5.389	4.88	13.65
2	26.38	5.386	4.93	13.75
3	27.44	5.085	10.25	28.24
4	27.84	4.986	12.00	28.35
5	29.28	4.666	17.65	28.63
6	29.81	4.582	19.13	28.64
7	30.53	4.442	21.59	28.65
8	31.29	4.335	23.49	28.74
9	31.97	4.264	24.75	28.80
10	27.40	5.176	8.64	8.012
11	33.99	3.963	30.04	37.13
12	35.95	3.725	34.25	48.87
13	39.94	3.390	40.16	80.29

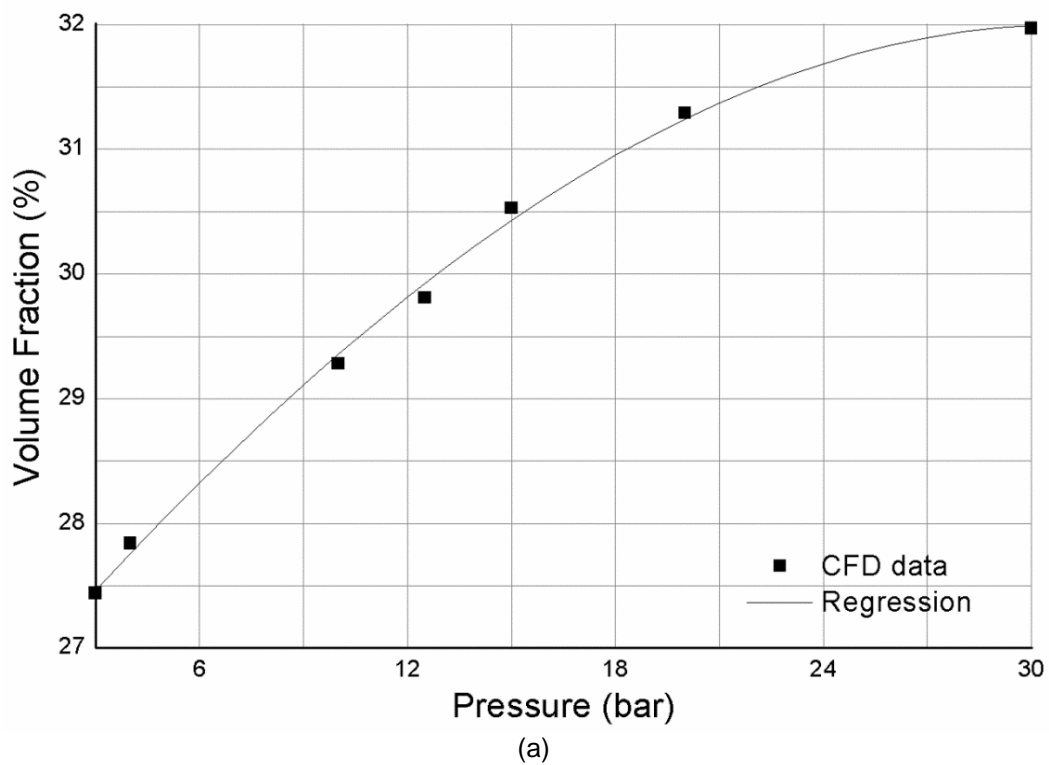
These results indicate that keeping the geometric parameters constant and increasing the inlet pressure (configurations 3 to 9) have a positive impact on the recovery of fine particles in the overflow, reducing the mean diameter. Another outcome is that increasing only the underflow opening or decreasing only the vortex finder diameter also increases the volume fraction of fine particles in the overflow and reduces its particle mean diameter. These predicted results are in agreement with the literature (Wang and Yu, 2006; Ozgen *et al.*, 2009). Hence, configuration 13 showed the highest volume fraction of fine particles in the overflow, and the lowest particle mean diameter value. However, it can also be observed a high liquid ratio for configuration 13, which means that most of the material goes towards the underflow, i.e., a small quantity of well-purified clay is obtained in the overflow.

The inlet pressure effect is illustrated in Figure 3.10(a), which shows a higher variation in the volume fraction of fine particles in the beginning; however, it demonstrates a decrease in the variation as the feed pressure approaches 30 bar. Therefore, applying pressure higher than 30 bar in the feed is not recommended as it

may not result in a significant increase in the clay volume fraction. It is also worth mentioning that for inlet pressures higher than 4bar, it was observed points of absolute pressure less than the water vapor pressure (2.3kPa) at the operating temperature (25°C), without modeling the air core formation. This means that cavitation occurs in these configurations as an undesired phenomenon, and it is not further modeled in this study. A general expression for clay volume fraction in the overflow can be formulated from the Gaussian regression line shown in Figure 3.10(a), and it is expressed in the form of Equation 3.14 with an adjusted R-square value of 0.9978.

$$X_V = 32e^{-\left(\frac{\Delta P - 31.14}{71.97}\right)^2} \quad (3.14)$$

Here, X_v is the volume fraction (%) of the clay fraction and ΔP is the pressure drop in the hydrocyclone.



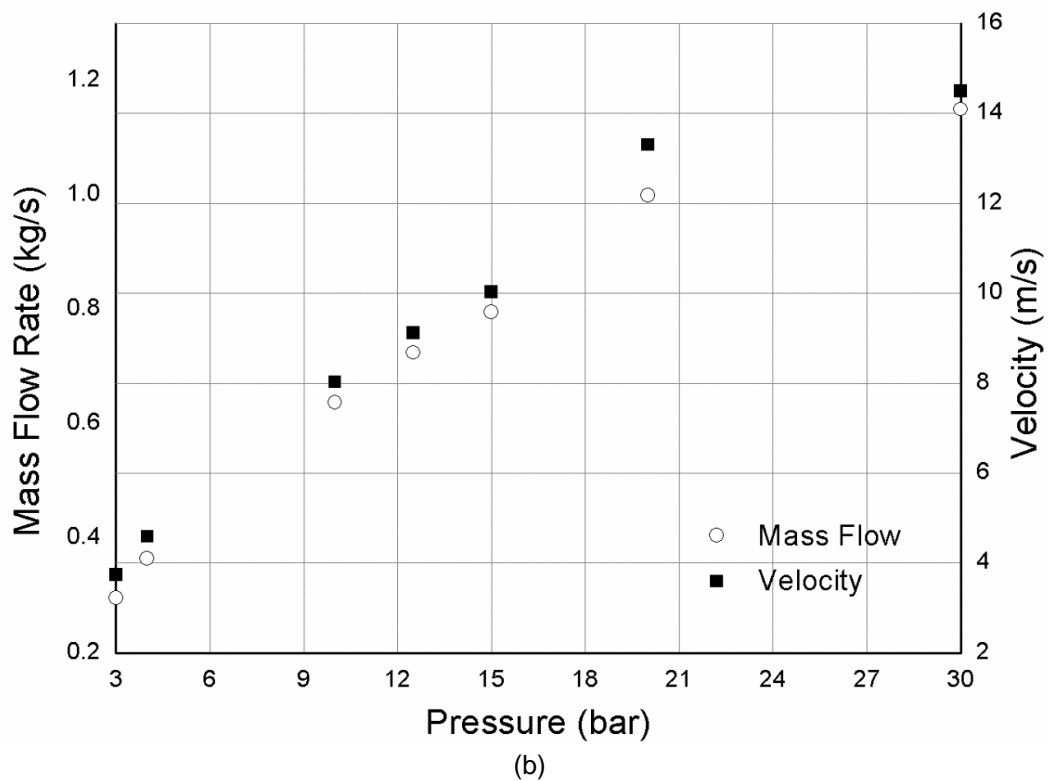


Figure 3.10: Effect of inlet pressure on (a) fine particles volume fraction at the overflow; (b) inlet mass flow rate and velocity.

The purpose of using a Gaussian function is to represent the behavior of the volume fraction of fine particles with the pressure drop. Therefore, it can rapidly give an estimation of volume fraction in the overflow for any inlet pressure between 3 and 30bar.

The inlet mass flow rate and velocity can also be obtained from the feed duct pressure, as showing in Figure 3.10(b). By increasing the pressure drop in the hydrocyclone, the inlet velocity and mass flow rate also increase. On the other hand, the fine recovery efficiency does not improve in the same proportion; therefore, in order to increase the recovery of fine particles, a parallel hydrocyclone operation is recommended instead of increasing the feed mass flow rate.

In addition, Table 3.9 shows the recovery to overflow of configurations 5 to 13, which indicates that configuration 13 results in a large amount of coarse particles in the underflow. These data corroborate that this configuration best meets the purpose of the clay purification studied in this work, even though the equipment is not quite effective. The analysis of the design parameters and operating conditions' effect from experiments and CFD simulations, as described in this study, proved to be a useful methodology for optimizing the hydrocyclone design and operating conditions. This is

clarified as we see that configurations 5 to 13 were unfeasible to perform experiments since the feed pressure could not be achieved due to a pump restriction, and the geometries were different. Therefore, as long as the CFD model is previously validated, it can be extended to other design and operating conditions.

Table 3.9: Predicted reduced granulometric efficiency in the overflow.

Particle diameter (μm)	Configuration								
	5	6	7	8	9	10	11	12	13
	Reduced Granulometric Efficiency (%)								
0.04	100.00	100.00	100.00	100.00	100.00	100.00	100.00	100.00	99.90
0.07	100.00	100.00	100.00	100.00	100.00	100.00	100.00	100.00	99.89
0.1	100.00	100.00	100.00	99.99	99.99	100.00	99.99	99.99	99.89
0.25	99.98	99.98	99.97	99.97	99.96	99.99	99.95	99.96	99.82
0.5	99.92	99.91	99.89	99.86	99.84	99.94	99.77	99.79	99.58
0.75	99.82	99.78	99.75	99.68	99.65	99.86	99.44	99.44	99.18
1	99.68	99.63	99.59	99.46	99.37	99.74	99.07	99.02	98.61
2	98.53	98.32	98.17	97.66	97.32	99.05	96.39	95.79	94.75
3	96.10	95.56	95.06	93.81	92.84	97.61	90.63	88.83	87.03
4	93.14	92.22	91.31	89.27	87.67	95.77	84.14	80.98	78.54
5	89.56	88.24	86.87	83.97	81.85	93.47	76.90	72.41	69.12
10	66.71	64.78	61.60	54.97	51.05	77.90	45.68	41.63	25.67
20	28.36	25.43	26.49	21.86	14.42	36.64	32.27	34.80	1.67

3.4.4 Scale-up analysis

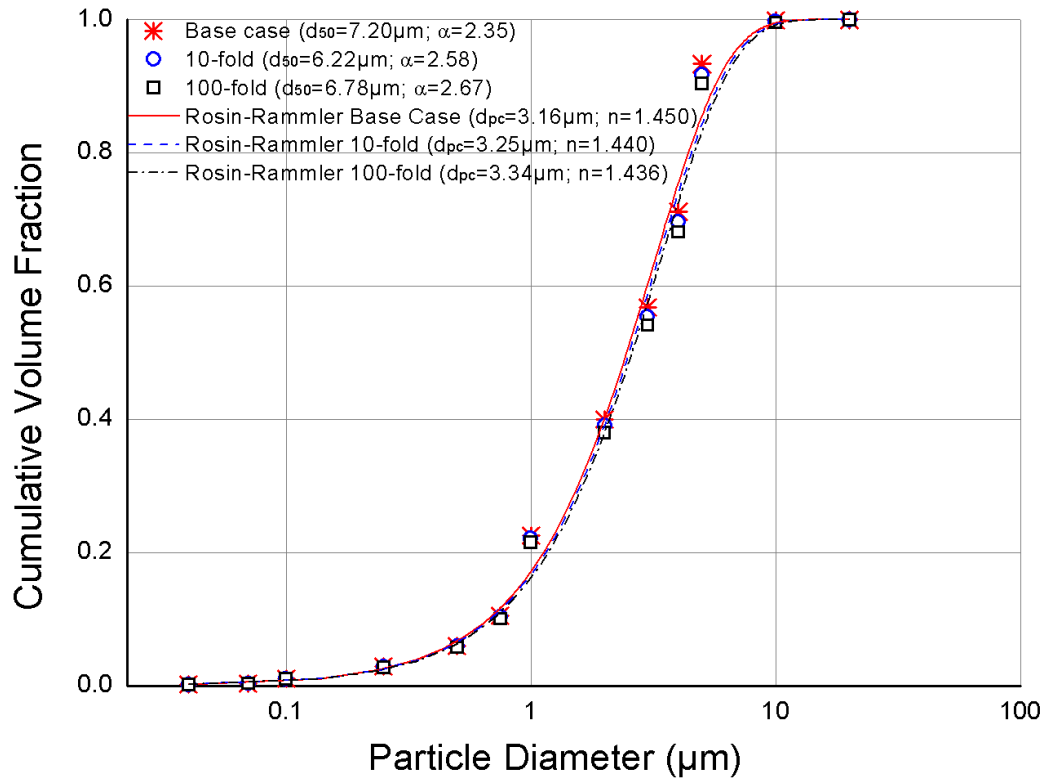
Based on the micro-hydrocyclone CFD model previously studied, feed flow was increased by a factor of 10 and 100 to obtain the cut size diameter from each simulation, verify their similarity in terms of cut size diameter, and predict the granulometric curve. Configuration 13 in Table 3.3 is the base case for this analysis since it presented the highest fine recovery in the overflow. From Equation 3.13, the ratio between the diameters of the cylindrical section is calculated, and it represents the scale-up factor for the geometry. Figure 3.11(a) shows that the hydrocyclone

simulations return comparable reduced cut size diameters, indicating that the characteristic performance of industrial hydrocyclones can be estimated from the micro-hydrocyclone model. Figure 3.11(a) also presents fitted Rosin-Rammler distribution (Equation 3.15) curves with comparable characteristic diameters (d_{pc}) and spread parameters (n).

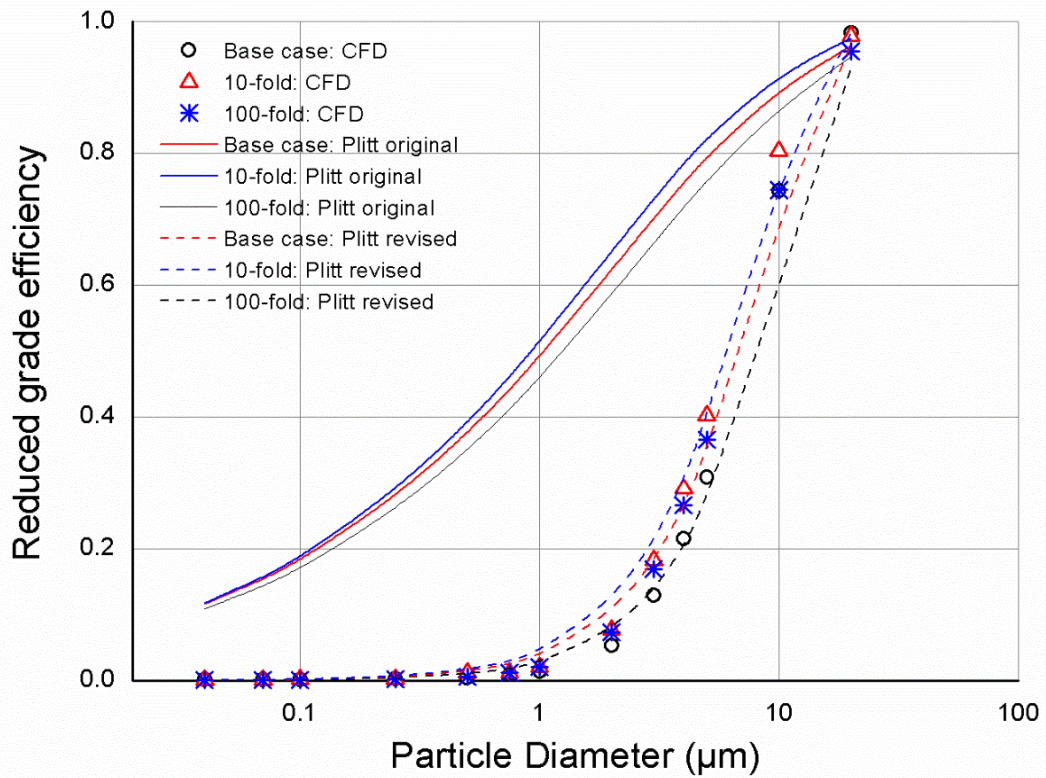
$$X_v = 1 - e^{-\left(\frac{d_p}{d_{pc}}\right)^n} \quad (3.15)$$

Since the outcomes demonstrate similarity, the value of K can be calculated from Equation 3.12 using the respective values of the base case model. It resulted in $K=0.1072$ for the AWK RWK-42L hydrocyclone, which agrees with the order of magnitude for different hydrocyclone families presented by Svarovsky (1984). The predicted results were also compared to the Plitt model to calculate hydrocyclone performance.

The efficiency curves calculated from the original Plitt model ($D_o = 2\text{mm}$ and $D_u = 4\text{mm}$) and the predicted curves from CFD simulations are shown in Figure 3.11(b). Major differences can be observed between the curves, which emphasizes the relevance of numerical analysis of hydrocyclones for scale-up studies to obtain specific models for different equipment. From the model equations, it can be noticed that the performance parameters are highly dependent on geometric design. This implies different grade efficiency curves when considering the overflow diameter after vortex finder expansion, or even considering the underflow opening rather than the apex diameter. It may lead to results closer to CFD data and get better predictions for this hydrocyclone family from the Plitt model. Figure 3.11(b) also presents revised Plitt curves taking into consideration the overflow diameter after expansion ($D_o = 15\text{mm}$) and the apex diameter ($D_u = 4\text{mm}$). The revised Plitt curves show a better agreement with the CFD results.



(a)



(b)

Figure 3.11: Scale-up analysis: (a) Cumulative volume fraction in the over flow; (b) recovery to underflow comparison with Plitt model.

3.5 Final considerations

This study case evaluated the hydrocyclone performance for bentonite clay purification by removing large contaminant particles ($d_p > 2 \mu\text{m}$) from powders. This process enables the recovery of a more valuable product at the overflow. A CFD model was verified with experimental data and was used to simulate the hydrocyclone performance for removing silt from clay fraction for several operating and geometric conditions. The simulation outcomes show that the clay volume fraction and the reduction in the mean particle diameter are increased when the following conditions are met – increase in the feed duct pressure while the geometric parameters are kept constant, and increase in the underflow opening or decrease in the vortex finder diameter at a constant pressure. In general, pressure variation has a more significant influence on the volume fraction of fine particles. However, it is not recommended to increase the feed pressure beyond 30 bar as it does not yield a more significant effect on the volume fraction of fine particles. It was also observed that, for feed pressure higher than 4 bar, undesirable cavitation was predicted to occur inside the hydrocyclone without air core modeling. An empirical correlation to predict the volume fraction of fine particles in the overflow as a function of the pressure drop in the hydrocyclone was obtained and can be further used as an initial analysis of the process. For the case study of this work, the configuration with a 6 mm underflow opening, 2 mm vortex finder diameter, and 30 bar feed duct pressure is the optimum for clay purification. These geometric parameters and operating conditions reduced the particle mean diameter by 40.16%, reaching a value of $3.39 \mu\text{m}$, along with a fine-particle volume fraction of 39.94% in the overflow. This work also presented a scale-up analysis that can be used to extend the results to any hydrocyclone of the same family, geometrically proportional to configuration 13. The numerical study provided accurate results for hydrocyclone performance by varying operating conditions to find the scenario that maximizes the clay-fine volume fraction.

Chapter 4

Wind effect on gas jets for hazardous area classification

This chapter is dedicated to study the influence of wind speed and direction on flammable gas jets for hazardous area classification from CFD simulations. The international standard IEC 60079-10-1(2015), which determines guidelines to ensure process safety, also recommends the usage of CFD tools to obtain accurate predictions of potentially explosive atmospheres formation in specific configurations such as the scenarios described in this study.

The study case aims to evaluate the extent and volume of methane, propane, and hydrogen leakages from a CFD model. For each flammable gas, the wind speed and direction are regularly varied, and the results are compared to the international standard in terms of extent and hazardous zone type. Here, numerical experiments enable considering scenarios that are not covered by empirical correlations, analytical expressions, or even by the international standard itself. Therefore, a comprehensive study of the wind influence on gas jets, as proposed here, may lead to a significant contribution to make safer decisions as an engineer.

4.1 Study case background

Hazardous area classification is a methodology that analyzes the potential risk in a flammable leak and defines the extent to which safety precautions must be taken. This technique is assessed by the international standard IEC 60079-10-1(2015) that suggests several guidelines to reduce the risk of explosion. A hazardous area is described as an area where an explosive atmosphere is or is likely to be present, and some parameters must be considered to evaluate the risk. The primary concern is the grade of release that reports the frequency of emission. The physical properties of the

substance, in turn, provide information about its flammability level, while the process variables and orifice size determine the discharge rate. In addition, the location characteristics affect the dispersion of flammable substances in the air, and the nature of emission leads to a one-phase or two-phase flow release.

Regarding gas emission, empirical and numerical models validated against experiments are presented in the literature (Alves et al., 2019). For instance, computational fluid dynamics (CFD) tools are widely used to predict gas dispersion in different scenarios, such as accidental releases (Silgado-Correa et al., 2020; Li et al., 2020(a); Li et al., 2020(b); Li et al., 2019) and fugitive emissions (Souza et al., 2018; Souza et al., 2019). Accidental release scenarios are relevant studies in the field of safety management but differ from continuous fugitive emissions that occur during normal operation from small openings, such as in pipe fittings. Hazardous area classification encompasses fugitive emissions analysis and is mainly considered at the project level. This methodology analyses the extent and volume of flammable gas clouds as a result of the interaction between storage temperature and pressure, orifice diameter, and molecular weight. The concentration of the flammable gas after the release is also directly affected by the local ventilation effectiveness, which depends on wind velocity, distribution of the ventilation, obstacles and its geometry, and leakage location (Ivings et al., 2010; Webber et al., 2011).

Moreover, the wind influence on the dispersion of flammable materials changes according to the release kinetic energy. When momentum forces predominate, the jet is characterized by a well-defined shape with entrainment of large quantities of air, which is favored by a co-flow airspeed. If buoyancy forces predominate, the leak generates a plume. In both scenarios, atmospheric turbulence represents a significant factor after the momentum or buoyancy decay, and it is important for further dispersion (Lees, 2005). Therefore, the numerical analysis of wind effects contributes meaningfully to area classification studies as it introduces this parameter for the calculations of the hazardous extent.

IEC 60079-10-1(2015) states that for areas where there is natural ventilation, the wind velocity must consist of a value that is exceeded 95% of the time. Further information about wind direction and speed at a particular location can be obtained from the wind rose, and for safety reasons, the calculations must consider the worst-case scenario. The wind velocity value and jet release rate indicate the degree of dilution of the environment, which is further combined with the availability of ventilation

and grade of release to classify the area according to the risk level (non-hazardous, Zone 0, Zone 1, or Zone 2). The hazardous classification following IEC 60079-10-1(2015), however, does not take into consideration the effect of wind direction. In that way, the international standard recommends computational modeling as an alternative approach to assess ventilation and to estimate the hazardous zone extent that results from the interaction of different variables, as written below:

“Guidance on the assessment of ventilation and dispersion is provided in Annex C. Other forms of assessment, e.g. computational fluid dynamics (CFD), may be used and may provide a good basis for assessment in some situations. Computer modelling is also an appropriate tool when assessing the interaction of multiple factors.”

4.1.1 Hazardous area classification overview

The main objective of the hazardous area classification technique is to reduce the probability of accidental ignition in explosive atmospheres. It does not take into consideration catastrophic failures; hence, it analyzes leakages that occur within the design parameters of a process plant. Good practices are outlined by the international standard IEC 60079-10-1(2015), which classifies hazardous areas as Zone 0, Zone 1, and Zone 2 (Table 4.1) according to a given degree of dilution and grade of release.

Table 4.1: Zone type definition for hazardous area classification

Zone type	Definition
Zone 0	Occurs when an explosive atmosphere is continuously present, frequent or exists for long periods of time
Zone 1	Is an area where an occasional formation of an explosive atmosphere is likely to occur
Zone 2	Occurs when the explosive atmosphere formation is not likely to occur but, if it does occur, it persists for a short period

The degree of dilution is determined based on a combination between the discharge rate of a substance and the wind velocity. For releases in an open environment, the degree of dilution is defined according to the flammable volume value (high dilution when $V_z < 0.1 \text{ m}^3$), which is significantly different from the explosive mixture results of CFD simulations, as demonstrated by Tommasini (2013). The difference in

these values may lead to a wrong zone type or inaccurate hazardous distances; as a consequence, overestimation results in additional costs, while underestimation implies a lack of safety (Zohdirad et al., 2016). The grade of release, in turn, is categorized as continuous, primary, or secondary depending on the frequency of emission during normal operation. It is classified as a continuous grade of release if the leakage is continuous or is expected to occur for long periods; primary grade of release when the emission is expected to occur periodically or occasionally; and secondary grade of release when the emission is not expected to occur or exists for a short time.

Once the zone type is defined, the extent of the hazardous area has to be determined. The hazardous extent is the distance where the concentration of flammable substance reaches the lower flammability limit (LFL) that represents the minimum volume fraction at which self-sustaining flame propagation occurs after ignition. An explosive atmosphere is present within this hazardous area, and some recommendations to manage the risk must be considered: restrict the usage of Non-Ex electrical equipment that can be an ignition source or eliminate the likelihood of an explosive gas atmosphere occurring near the source of ignition.

Different approaches to obtain the explosive mixture volume and hazardous extent are presented in the literature (Tommasini, 2013; Benintendi, 2010; Benintendi, 2011; Ewan and Moodie, 1986; Lees, 2005; McMillan, 1998; Souza et al., 2018), but the influence of wind velocity is not explicitly taken into consideration in these analyses. Ivings et al. (2010) affirm that the increase in airspeed or the change in airflow direction (varying from co-flow) leads to smaller gas cloud volume for an outdoor release without obstacles. In this case, the worst-case scenario would be low wind velocities in the leak direction, but it needs to be verified in detail since the wind affects the jet momentum, which further defines the cloud shape. It may also strongly influence the extent and volume of the released material affecting the hazardous area classification as discussed by Oliveira et al. (2019) for a two-phase flow release scenario. Figure 4.1 illustrates the configuration of a gas cloud along the release axis and shows that the concentration of the flammable substance and jet velocity approaches zero simultaneously. The location of zero velocity is highly influenced by the airflow speed and direction. Therefore, a detailed study of the wind effect on a jet release using CFD tools contributes to obtaining a safer risk assessment while avoiding the overestimation of hazardous areas.

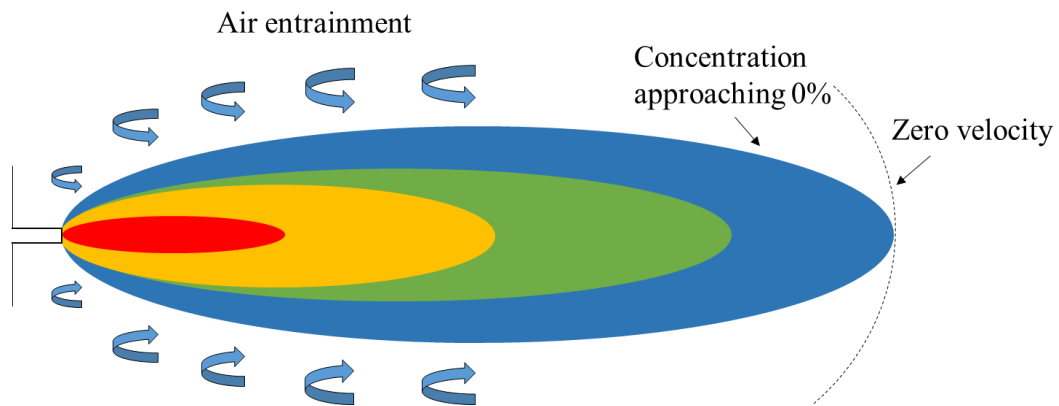


Figure 4.1: Configuration of a gas cloud after a jet release (adapted from IEC 60079-10-1).

Moreover, the methodology proposed by the international standard IEC 60079-10-1(2015) to assess hazardous areas is based on Figures 4.2-4.4. Initially, it is obtained the degree of dilution from Figure 4.2, followed by the classification into zones according to Figure 4.3, and finally, the determination of the hazardous extent as presented in Figure 4.4.

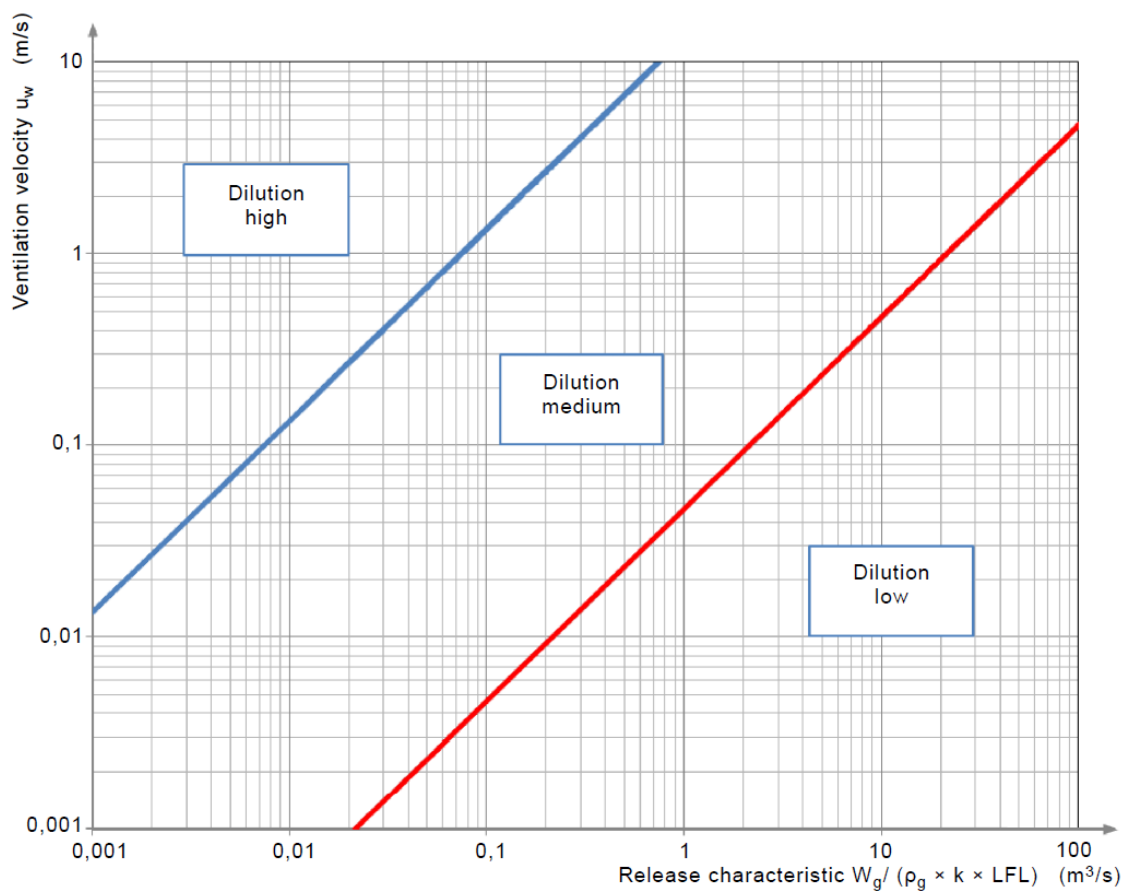


Figure 4.2: Assessment of the degree of dilution (IEC 60079-10-1, 2015).

Grade of release	Effectiveness of Ventilation						
	High Dilution			Medium Dilution			Low Dilution
	Availability of ventilation						
	Good	Fair	Poor	Good	Fair	Poor	Good, fair or poor
Continuous	Non-hazardous (Zone 0 NE) ^a	Zone 2 (Zone 0 NE) ^a	Zone 1 (Zone 0 NE) ^a	Zone 0	Zone 0 + Zone 2	Zone 0 + Zone 1	Zone 0
Primary	Non-hazardous (Zone 1 NE) ^a	Zone 2 (Zone 1 NE) ^a	Zone 2 (Zone 1 NE) ^a	Zone 1	Zone 1 + Zone 2	Zone 1 + Zone 2	Zone 1 or zone 0 ^c
Secondary^b	Non-hazardous (Zone 2 NE) ^a	Non-hazardous (Zone 2 NE) ^a	Zone 2	Zone 2	Zone 2	Zone 2	Zone 1 and even Zone 0 ^c

^a Zone 0 NE, 1 NE or 2 NE indicates a theoretical zone which would be of negligible extent under normal conditions.

^b The zone 2 area created by a secondary grade of release may exceed that attributable to a primary or continuous grade of release; in this case, the greater distance should be taken.

^c Will be zone 0 if the ventilation is so weak and the release is such that in practice an explosive gas atmosphere exists virtually continuously (i.e. approaching a 'no ventilation' condition).

'+' signifies 'surrounded by'.

Availability of ventilation in naturally ventilated enclosed spaces shall never be considered as good.

Figure 4.3: Hazardous area classification into zones (IEC 60079-10-1, 2015).

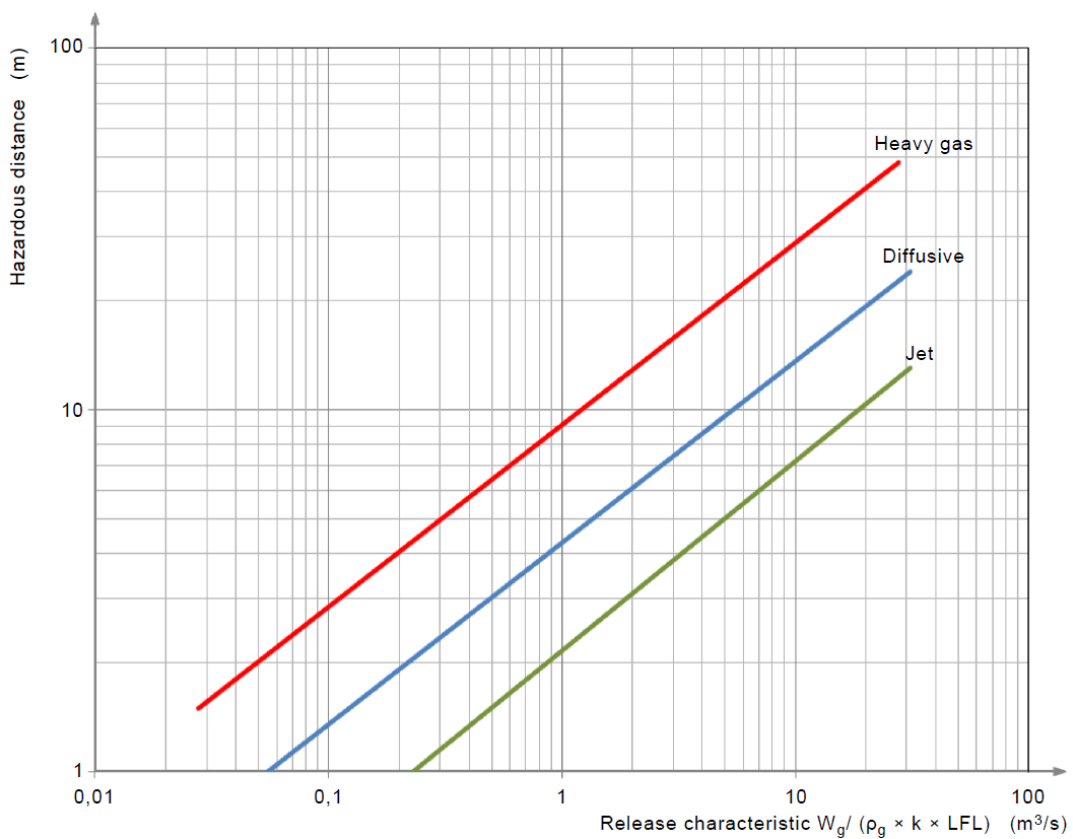


Figure 4.4: Estimation of hazardous area extent (IEC 60079-10-1, 2015).

4.1.2 Gas jet release

The gas jet release is modeled as a function of the storage conditions. The emission conditions for high momentum gas releases are calculated as a sonic flow (Mach number = 1), considering mass and energy balances for an isentropic expansion. The choked flow is characterized by the presence of a sonic barrel resulting from the expansion caused by a pressure gradient between the storage and the ambient. The pressure ratio that defines the sonic flow regime follows the condition showed in Equation 4.1 (Alves et al., 2019):

$$\frac{P_a}{P_s} \leq \left(\frac{2}{\gamma + 1} \right)^{\frac{\gamma}{\gamma - 1}} \quad (4.1)$$

Where P_a is the ambient pressure, P_s is the storage pressure, and γ is the Poisson coefficient (C_p/C_v).

Souza et al. (2019) demonstrated that the deviation from ideal behavior has a negligible influence on the hazardous extent and volume results. Therefore, once the flammable substance and storage conditions are known, this work considers a compressible flow of an ideal gas to calculate the release condition, i.e., pressure (Equation 4.2), temperature (Equation 4.3), and velocity (Equation 4.4) (Sissom and Pitts, 1972).

$$P_i = P_s \left(\frac{2}{\gamma + 1} \right)^{\frac{\gamma}{\gamma - 1}} \quad (4.2)$$

$$T_i = T_s \left(\frac{2}{\gamma + 1} \right) \quad (4.3)$$

$$v_i = \left(\frac{2\gamma}{\gamma + 1} \frac{R}{W} T_s \right)^{\frac{1}{2}} \quad (4.4)$$

Where P_i , T_i , v_i are pressure, temperature, and velocity at the orifice inlet, P_s , T_s are the storage pressure and temperature, R is the universal gas constant, and W is the molar mass of the gas.

4.2 CFD model

The CFD model for jet dispersion resulting in a flammable gas cloud is based on the conservation laws of mass, species, momentum, and energy for a non-reactive flow, as described in Chapter 2. Considering that the phenomenon treated here involves a multicomponent flow, the numerical solution is calculated by using appropriate averaged values of physical properties for each control volume.

A set of cases of high momentum gas dispersion in an open environment without obstructions was modeled using ANSYS CFX 16.1 software. The wind direction and velocity were varied to analyze the influence of these variables in the plume extent and volume. The wind velocity magnitude was regularly ranged from 0 to 10m/s in both the release direction and the opposite release direction, evaluating a total of 11 configurations for each condition in Table 4.2. Table 4.2 presents the storage and orifice inlet conditions, as well as flammable substances used in this study. Here, the conditions at the orifice inlet were calculated considering the model for a continuous gas jet release (Equations. 4.2-4.4).

Table 4.2: Storage and leakage conditions.

	Hydrogen	Methane	Propane
Storage temperature (K)	300.0	473.2	300.0
Storage pressure (bar)	100.0	60.8	8.0
Orifice diameter (mm)	1.0	1.3	0.5
Orifice velocity (m/s)	1188.6	527.8	253.1
Orifice pressure (bar)	54.2	32.5	3.4
Orifice temperature (K)	260.1	410.3	260.2

The geometry considered in this study corresponds to a 4-degree axisymmetric cylindrical slice of the ambient air surrounding a leak source in both directions, as illustrated in Figure 4.5. This approach approximates the domain to a two-dimensional analysis and, consequently, reduces the computational time (Oliveira et al., 2019). The dimensions are presented in Figure 4.5(b), in which the values are sufficiently large so that the far-field boundaries are represented by ambient conditions (1atm, 300K, and no flammable substance).

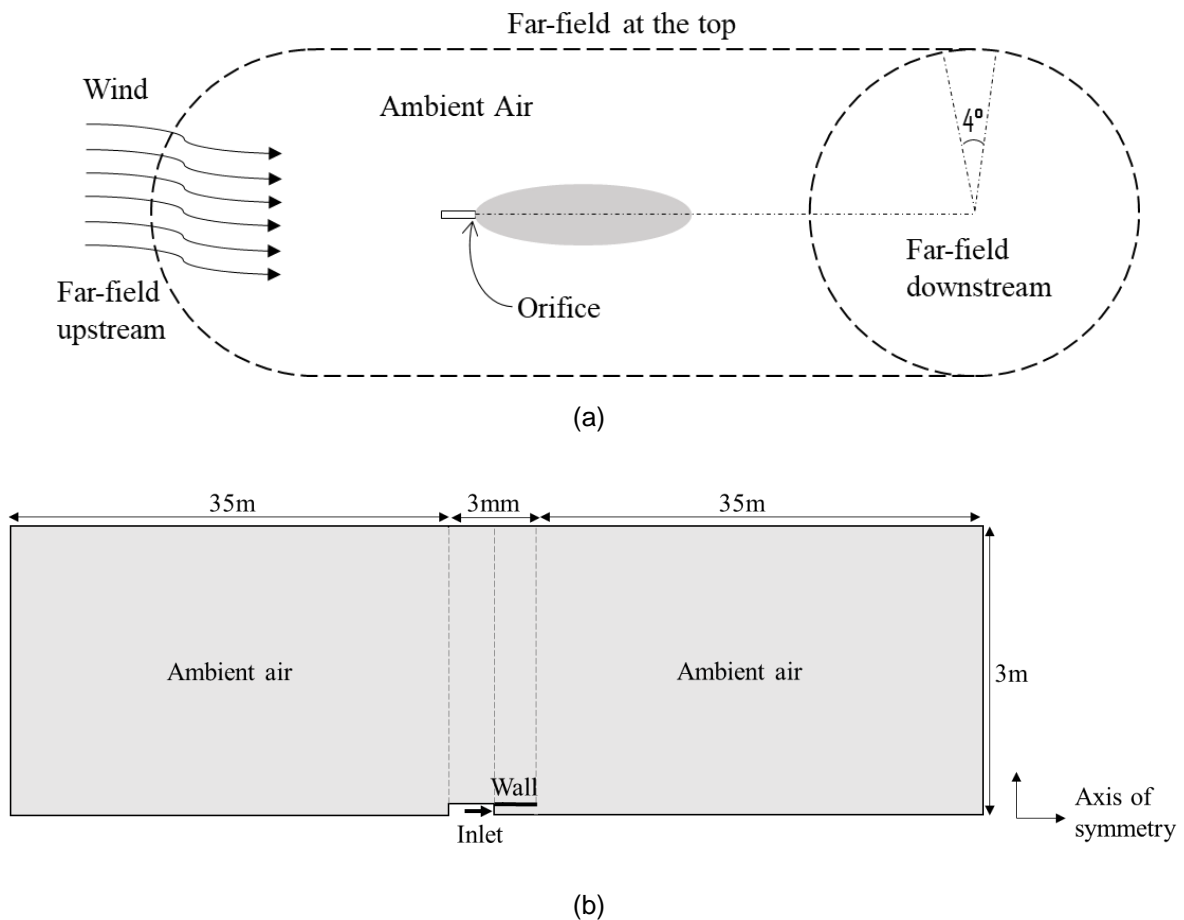


Figure 4.5: Geometry definitions: (a) schematic three-dimensional geometry; (b) dimensions.

The Shear Stress Transport (SST) turbulence model is used in this study. In addition, the total energy model was used to consider high-speed energy effects that result from the sonic velocity at the exit and also to account for the viscous effect (ANSYS CFX, 2015). The simulation also considered a compressible gas flow and neglected the gravity effect due to the axisymmetric condition. All the boundary conditions are described in Table 4.3.

The convergence criteria used in the present work were 1×10^{-5} for RMS residues and 1% for imbalance. Also, High Resolution was considered for both the advection scheme and turbulence numerics, and a fully coupled solver in which velocity and pressure are solved simultaneously was used for pressure-velocity coupling in Ansys CFX 16.1 solver.

Table 4.3: Boundary condition definition.

Location	Boundary Condition
Orifice	Inlet: Mixed flow regime; static pressure (Equation 4.2), static temperature (Equation 4.3), and normal speed (Equation 4.4) definition; zero gradient turbulence; and mass fraction (pure substance)
Far-field at the top	Opening: Ambient pressure and temperature; zero gradient turbulence; and absence of flammable substance
Far-field downstream	Opening (if $u_w > 0$) Inlet (if $u_w < 0$): Uniform velocity normal to the boundary; zero gradient turbulence; ambient temperature; and absence of flammable substance
Far-field upstream	Opening (if $u_w < 0$) Inlet (if $u_w > 0$)
Symmetry faces	Symmetry
Inlet Wall	Wall: No slip condition and adiabatic

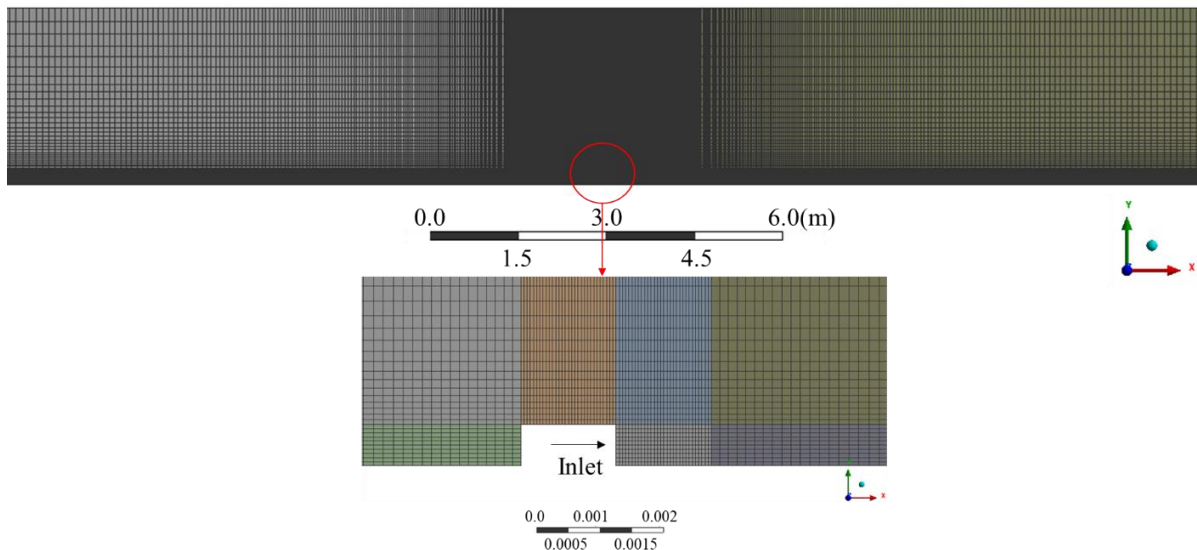
4.2.1 Grid independence study

A regular grid was created, and a higher refinement was defined near the orifice (Figure 4.6). A grid independence study was performed by varying the number of elements between 9300 and 226300, aiming to obtain an adequate mesh refinement for this study. The chosen grid must assure thorough results along with less computational time. Table 4.4 presents the mesh information of each case and the simulation results for the grid independence study.

The results from Table 4.4 show deviations in the extent values comparing cases 1 and 2, which are the coarser configurations. Also, these cases did not reach the convergence criteria. On the other hand, the hazardous extents of cases 3, 4, and 5 were close to each other. Since the outcomes did not change between cases 4 and 5, the grid represented in 4 was chosen to be used in the present work, giving accurate and numerical stable results while taking less simulation time.

Table 4.4: Grid Independence test (methane, $P_s=100\text{bar}$, $d_o=1\text{mm}$, $T_s=300\text{K}$, $u_w=0\text{m/s}$).

Mesh/Simulation Information	Case 1	Case 2	Case 3	Case 4	Case 5
Elements	9300	28300	116300	160300	226300
Nodes	18930	57130	233930	322330	459930
Number of iterations	39119	25380	5637	5659	5680
Simulation time	6h30m	6h30m	4h53m	6h41m	8h58m
Reached convergence criteria?	No	No	Yes	Yes	Yes
Extent to LFL (m)	0.878	0.848	0.837	0.836	0.836
Extent to $\frac{1}{2}$ LFL (m)	1.749	1.696	1.676	1.676	1.676
Extent to $\frac{1}{4}$ LFL (m)	3.475	3.388	3.355	3.354	3.354

**Figure 4.6:** Generated mesh.

4.2.1 CFD model verification

A previous work by Alves et al. (2019) verified the CFD model used in this study for different datasets in still air: a) with experiments for nitrogen gas in a pressure range of 20 to 100bar, and orifice diameter of 0.5 and 1mm; b) with experimental data available in the literature for neutrally buoyant gases ethylene and natural gas; c) with empirical correlations available in the literature for flow pattern verification and prediction of shock barrel formation. Moreover, the present study case verified the CFD model with three sets of experimental data for buoyant hydrogen gas releases presented by Papanikolaou et al. (2012), named HD35-37 ($P_s=53.27\text{bar}$, $T_s=287.65\text{K}$,

$d_o=1\text{mm}$), HD00-02 ($P_s=113.3\text{bar}$, $T_s=287.65\text{K}$, $d_o=0.75\text{mm}$), and HD22-24 ($P_s=162\text{bar}$, $T_s=287.65\text{K}$, $d_o=0.25\text{mm}$). Figure 4.7 shows that the CFD data adequately agree with the experiment results for concentration along the release axis, although the HD22-24 was made at high storage pressure, and it may be one of the reasons for being more distant to the model results (i.e., ideal gas correlations may not be suitable in this case). Therefore, the model was further used in this work by adding a constant airflow profile to the domain at the far-field, considering both co-flow ($u_w>0$) and counter-flow ($u_w<0$) wind velocity direction.

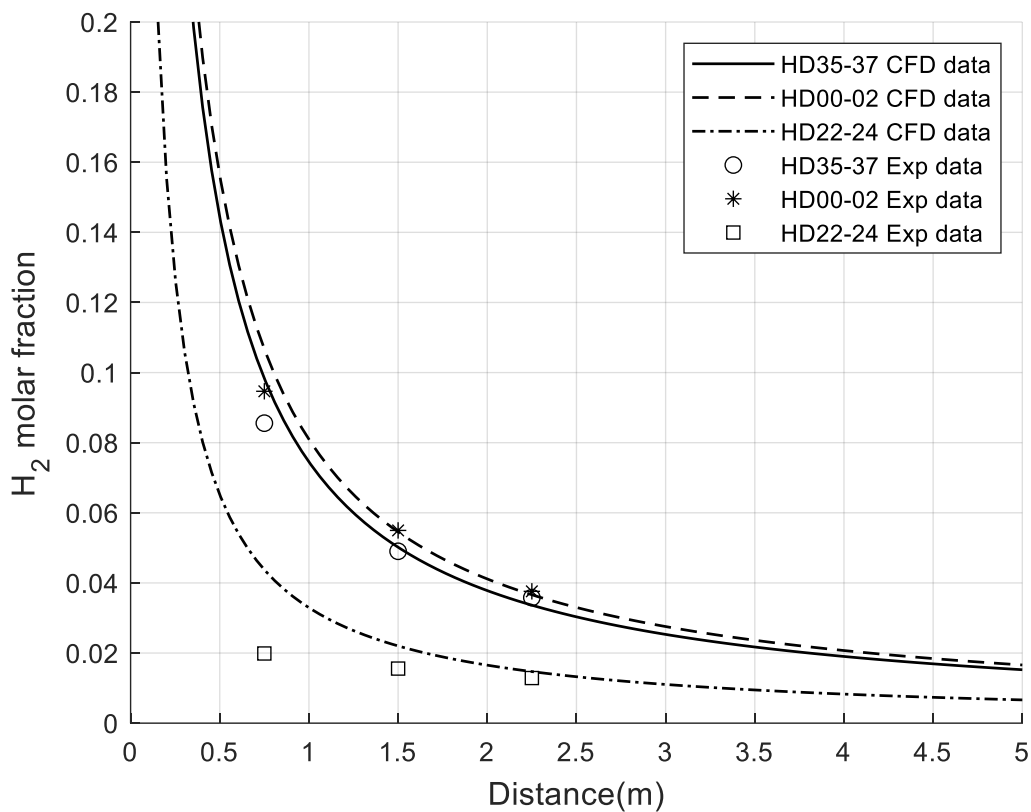


Figure 4.7: Model verification with experimental data from Papanikolaou et al. (2012).

4.3 Results

An important outcome of this study is the concentration profile of flammable gas along the release axis for different wind speed and direction. Figures 4.8-4.10 illustrate the behavior of each substance's molar fraction along the central axis, considering the wind in the jet direction. It shows that for all values of molar fraction, a higher wind speed implies a greater hazardous extent, i.e., positive wind enhances the air mixing in the jet while pushing forward the gas cloud. This increasing pattern is also observed in Figures 4.11-4.13.

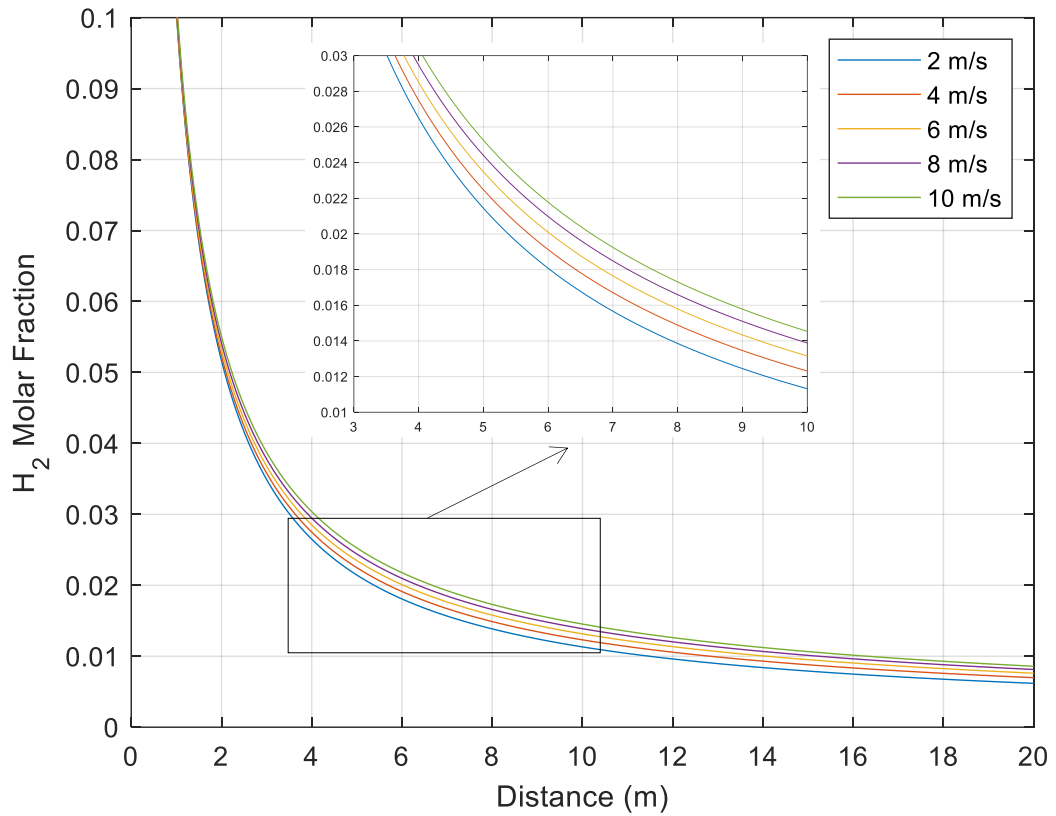


Figure 4.8: Concentration profile along the release axis for wind in the jet direction for hydrogen.

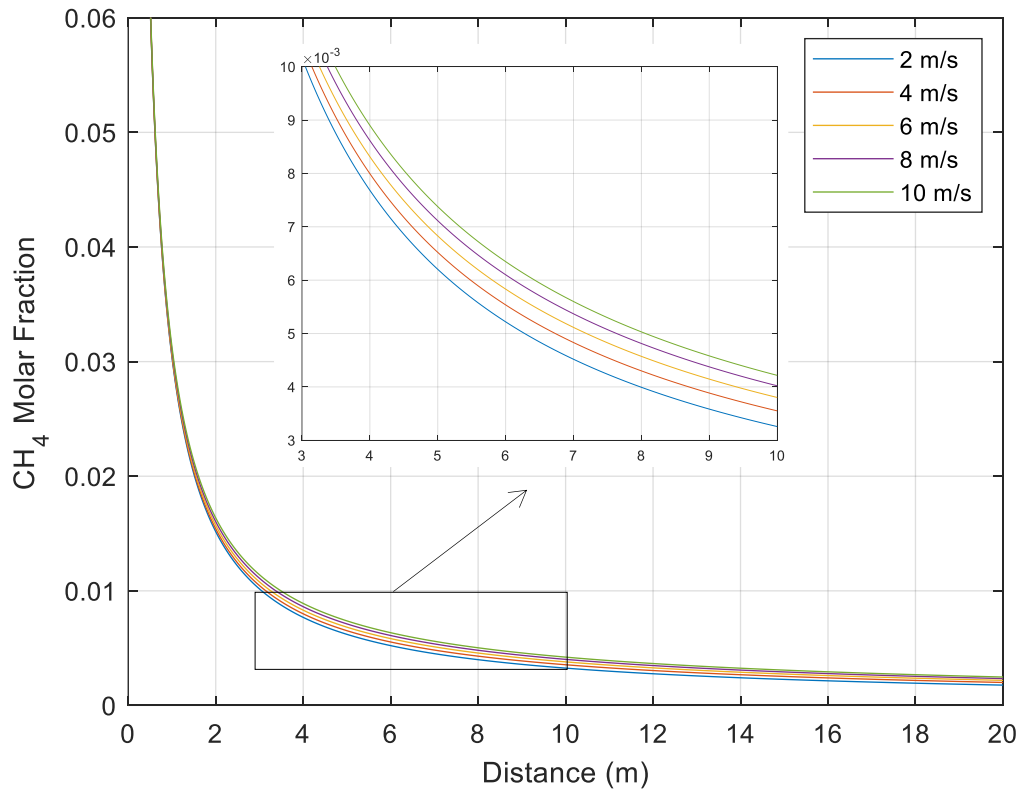


Figure 4.9: Concentration profile along the release axis for wind in the jet direction for methane.

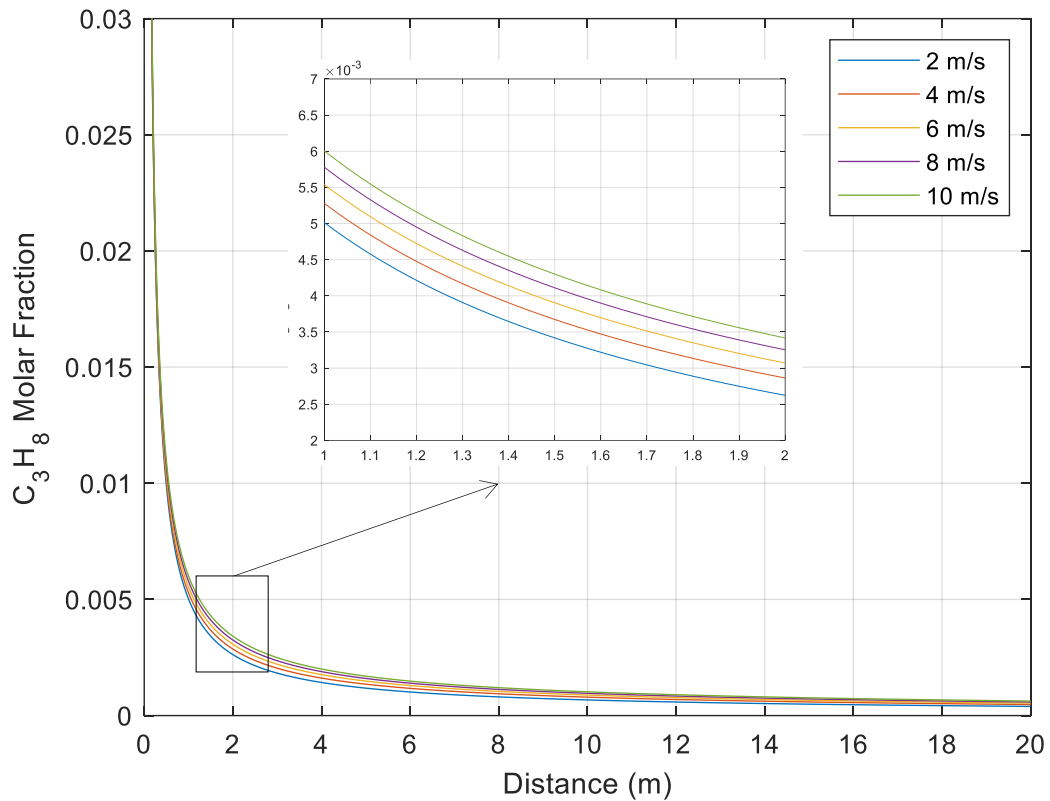
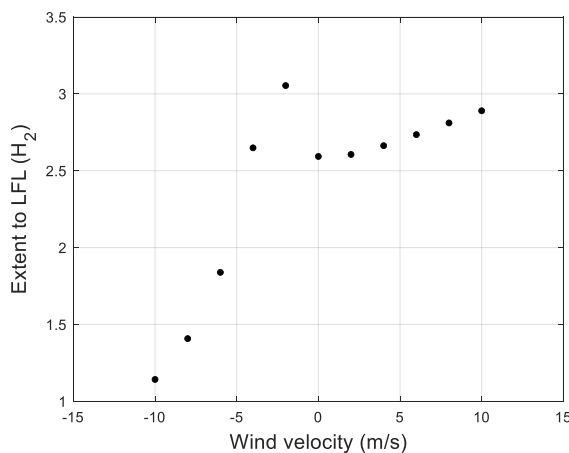
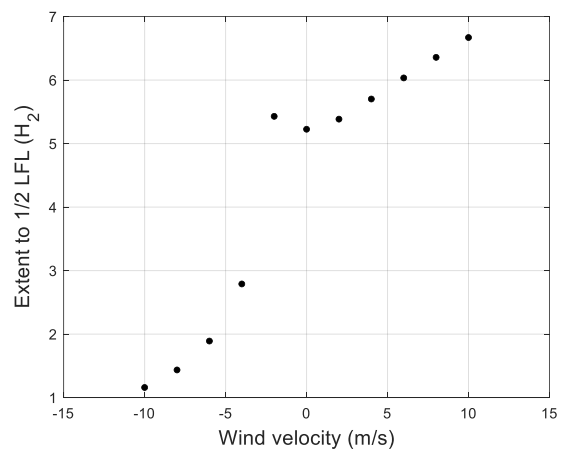


Figure 4.10: Concentration profile along the release axis for wind in the jet direction for propane.

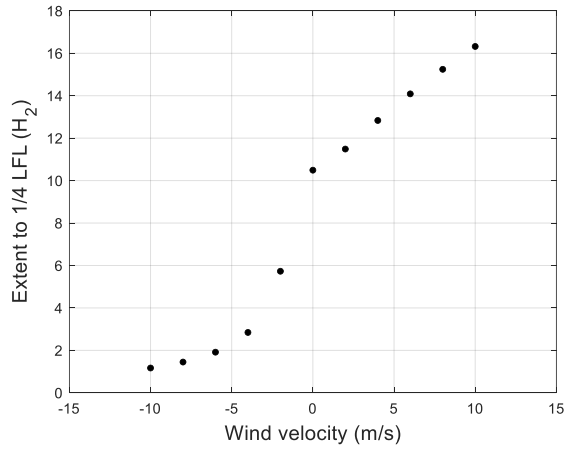
It can be observed from Figures 4.11-4.13 that both the positive and negative wind directions act with a higher intensity for hydrogen and with lower intensity for propane. It may be explained by a weaker air mixing due to the lower momentum jet of propane, compared to the other substances, and also lower mass diffusivity.



(a)

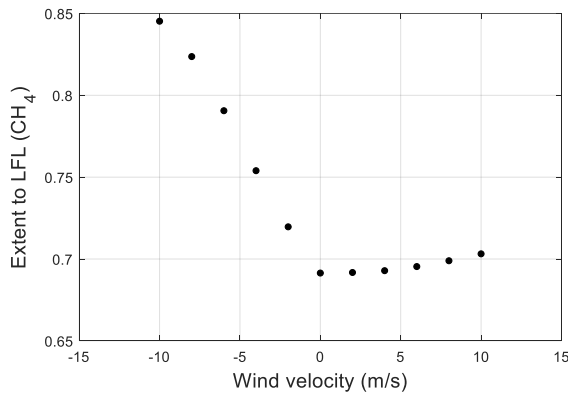


(b)

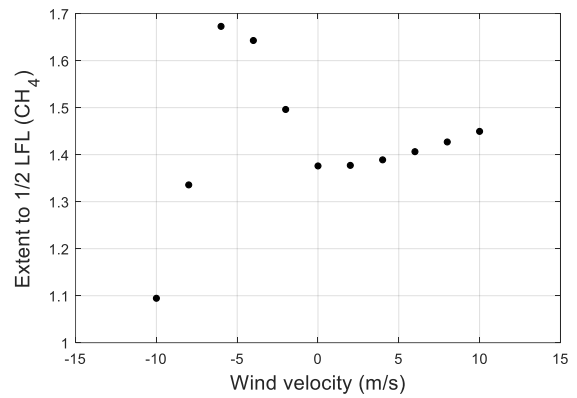


(c)

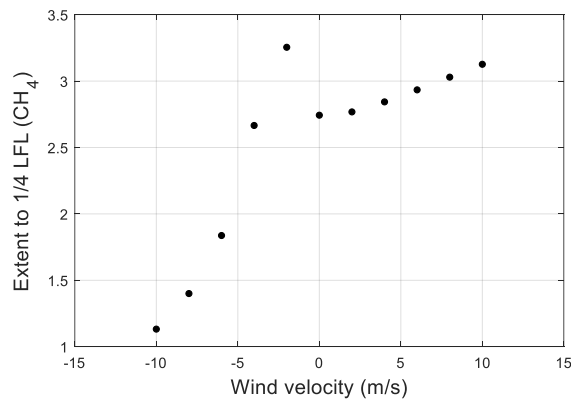
Figure 4.11: Hazardous extent for the hydrogen leakage: (a) to LFL; (b) to 1/2 LFL; (c) to 1/4 LFL.



(a)



(b)



(c)

Figure 4.12: Hazardous extent for the methane leakage: (a) to LFL; (b) to 1/2 LFL; (c) to 1/4 LFL.

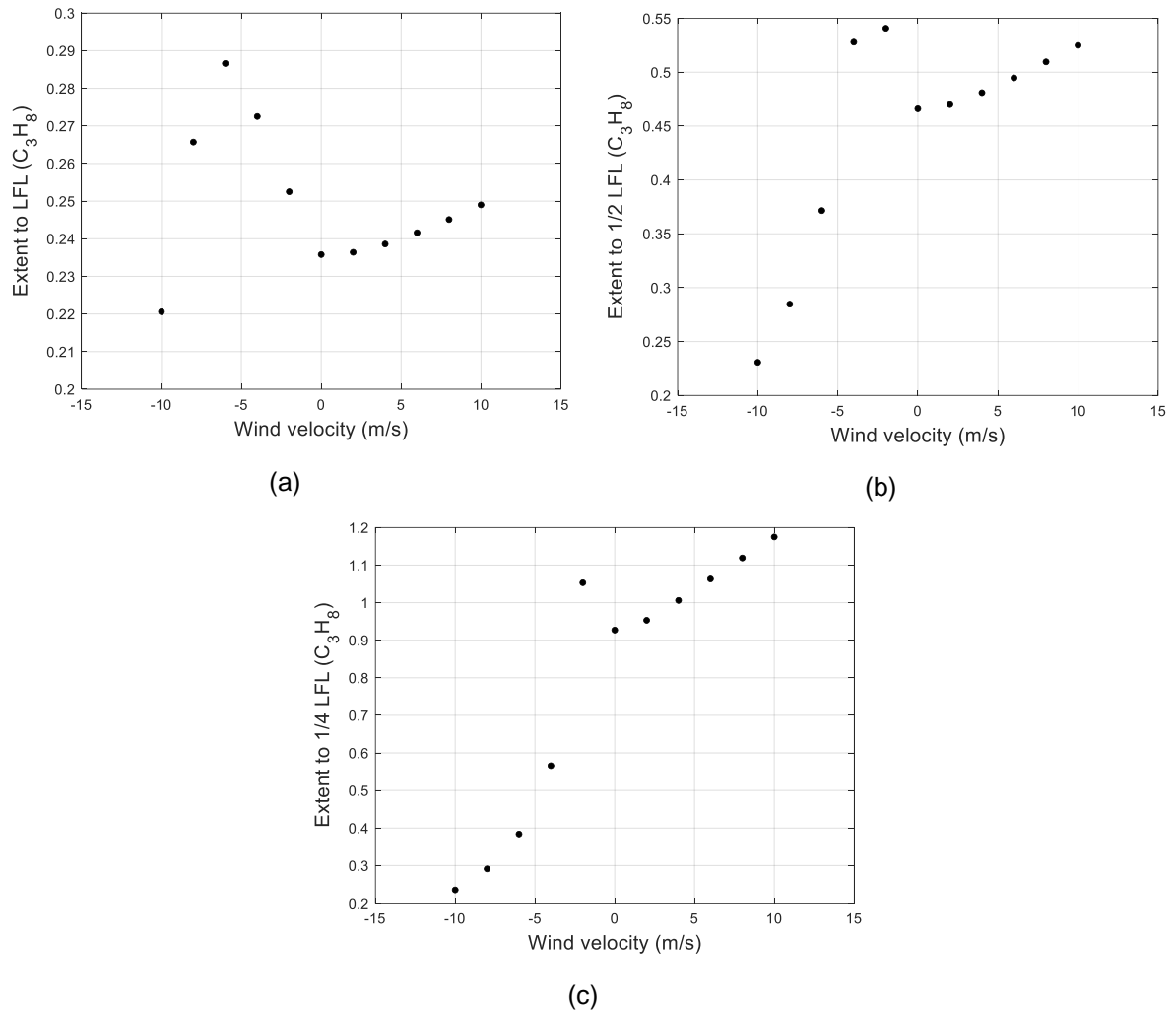


Figure 4.13: Hazardous extent for the propane leakage: (a) to LFL; (b) to $\frac{1}{2}$ LFL; (c) to $\frac{1}{4}$ LFL.

Concentration profiles for negative wind speed (opposite jet direction) show a disruption in the initial exponential behavior due to the zero relative velocity between jet and air (Figures 4.14-4.16). It means that, depending on the concentration value, the hazardous extent may not always increase for higher opposite wind speeds.

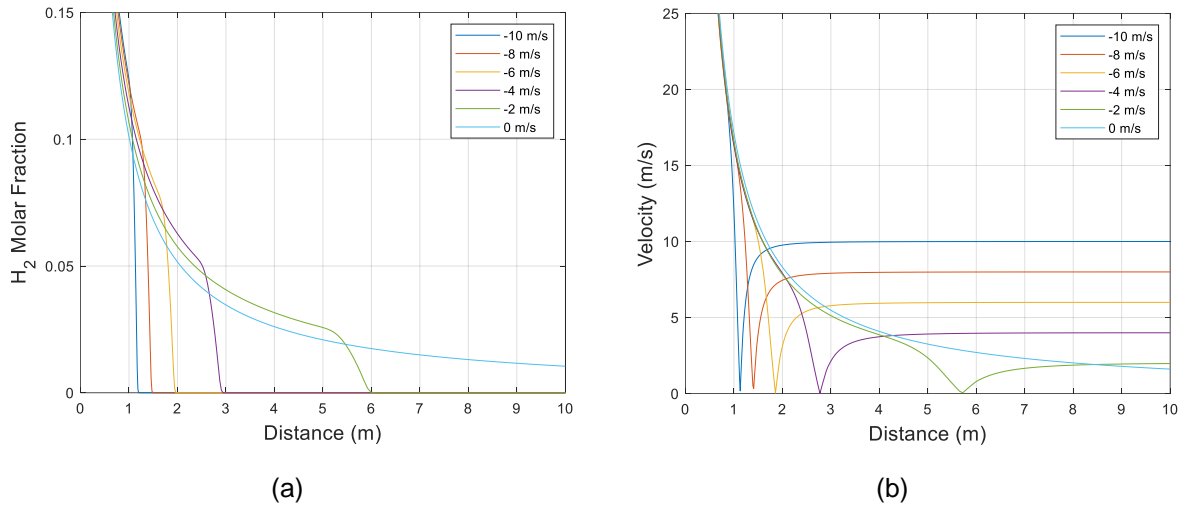


Figure 4.14: Hydrogen profiles along the release axis for wind in the opposite direction of the jet:
 (a)molar fraction; (b)mixture velocity magnitude.

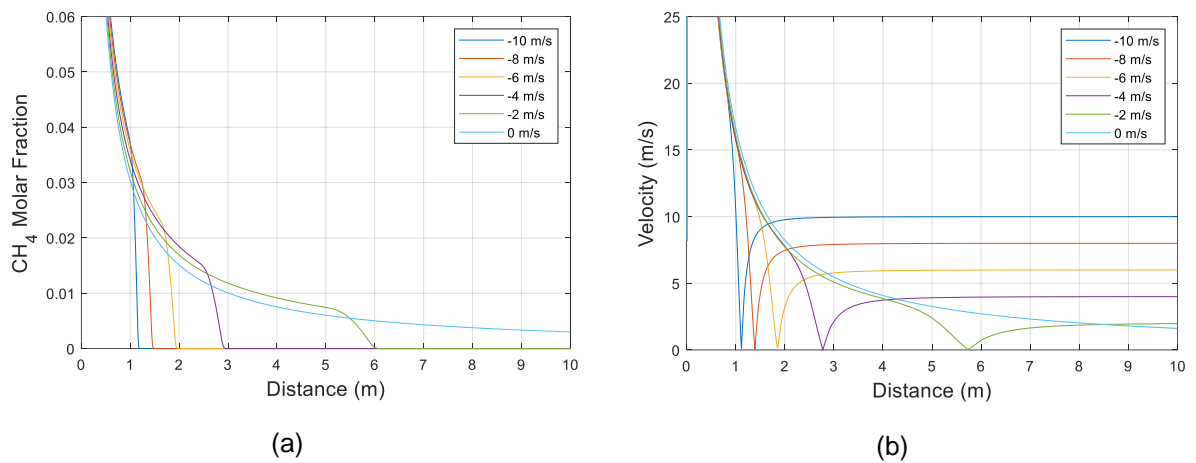


Figure 4.15: Methane profiles along the release axis for wind in the opposite direction of the jet:
 (a)molar fraction; (b)mixture velocity magnitude.

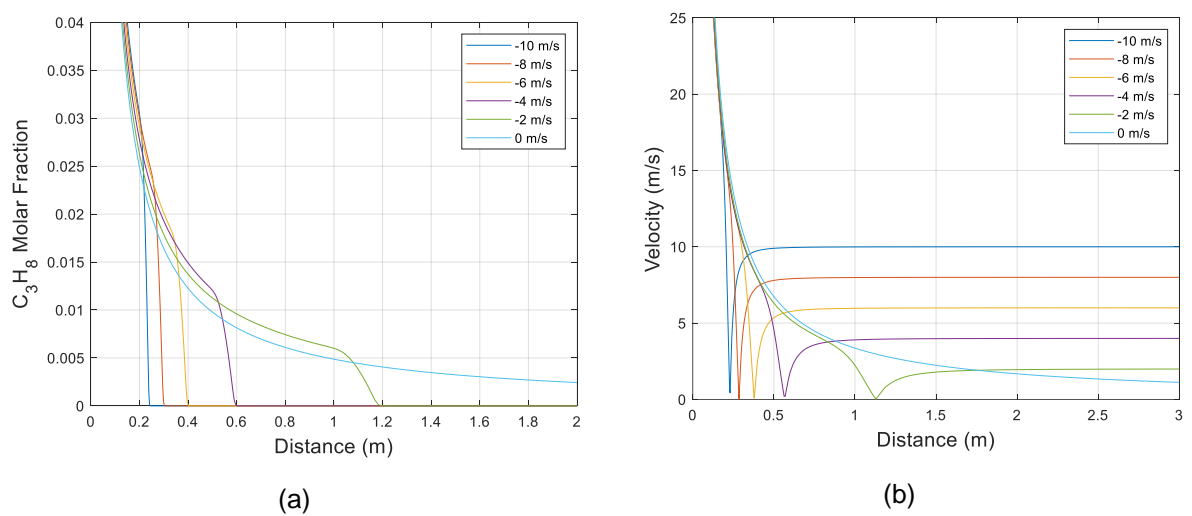
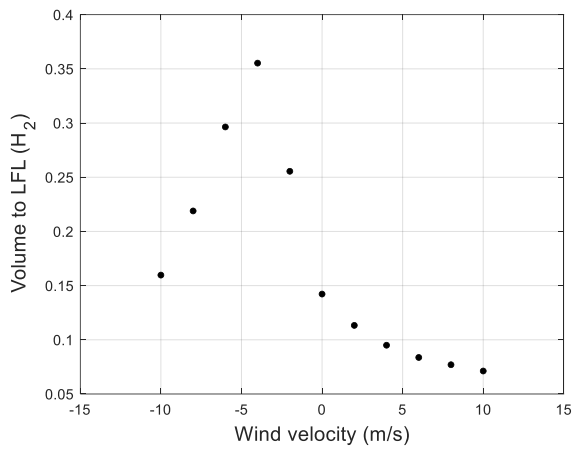


Figure 4.16: Propane profiles along the release axis for wind in the opposite direction of the jet:
 (a)molar fraction; (b)mixture velocity magnitude.

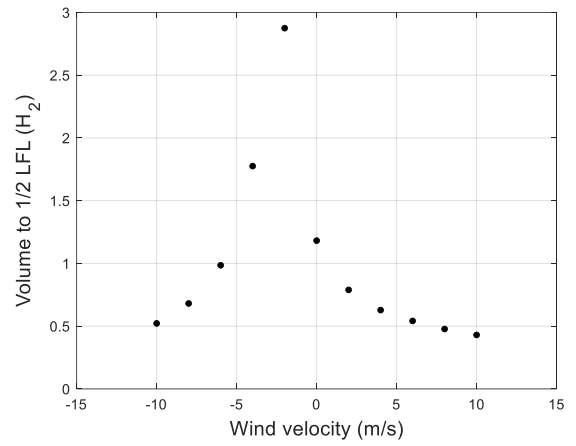
Upon inspection of Figures 4.14-4.16, it can be seen that the hazardous extent increases for greater wind speeds near the leak orifice. This is because the wind in the opposite direction of the jet concentrates the flammable substance in the near field region. However, when the relative velocity approaches zero, the gas molar fraction also reaches zero. Although the hazardous extent stops increasing in the leak direction after zero relative velocity, it may increase behind the leak orifice depending on the process conditions and flammable gas properties. Herein hydrogen and propane have a gas plume inversion that is not observed for methane, and this information is presented in Tables 4.5-4.7 for CFD extent in the jet opposite direction. It is important to notice that there is no mention in the IEC 60079-10-1(2015) about the hazardous extent's behavior regarding the wind in the opposite direction. Hence, the present results indicate a lack of information in the standard that may imply an inaccurate evaluation of the extent for an outdoor leakage scenario depending on the wind direction. Moreover, it is observed in IEC 60079-10-1(2015) that the ventilation only affects the zone type, such that the higher ventilation velocity, the more diluted is the hazardous substance in the ambient. However, the wind also influences the hazardous extent, as observed in the outcomes of this study.

The hazardous volume is also an important variable for hazardous area classification, and it is used to determine the zone type. Outdoors releases generally have good availability of ventilation, which is a present virtually continuously ventilation. Thus, for a continuous grade of release, a hazardous volume greater than 0.1m^3 means medium dilution and, consequently, Zone 0. On the other hand, a hazardous volume less than 0.1m^3 means high dilution, and a Non-hazardous area is defined. Figures 4.17-4.19 present the volume of the gas clouds for different wind velocities and directions. It can be clearly observed that the volume behavior depends both on the case simulated and the desired concentration.

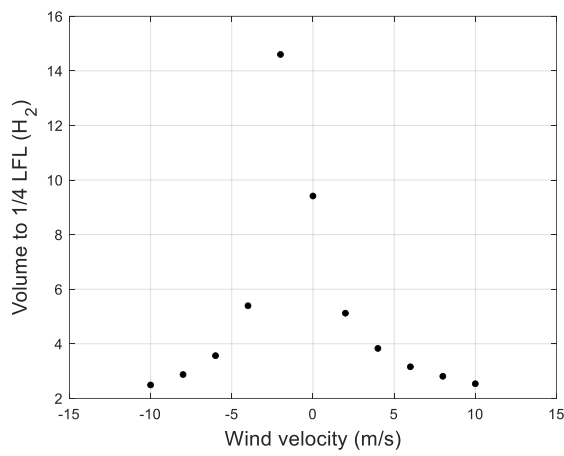
The outcomes show that the hazardous volume decreases as the wind in the jet direction increases due to higher air mixing. When the opposite airflow is evaluated, the hazardous volume generally has a non-monotonic behavior as it firstly increases with the wind velocity, and then it decreases. This change of pattern occurs when the airspeed is high enough to promote gas dispersion after concentrating the diluted gas closer to the emission point.



(a)

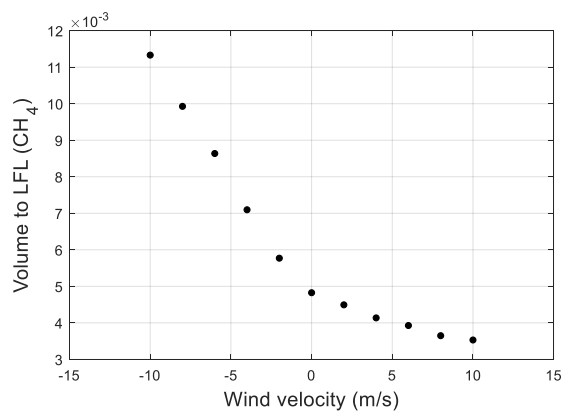


(b)

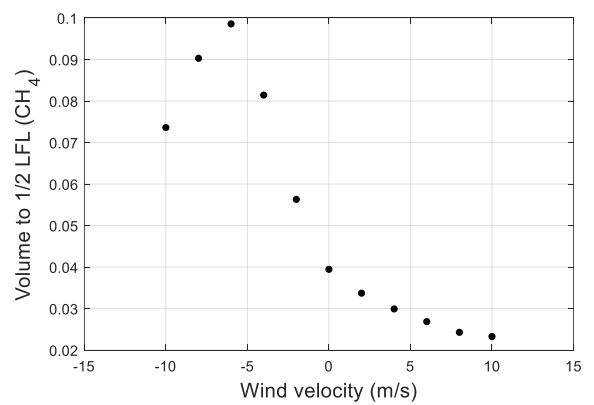


(c)

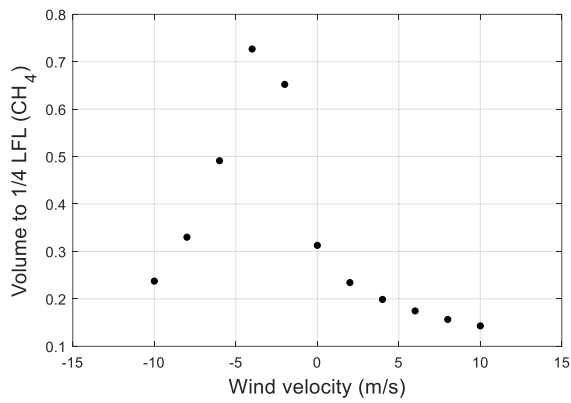
Figure 4.17: Hazardous volume for the hydrogen leakage: (a) to LFL; (b) to 1/2 LFL; (c) to 1/4 LFL.



(a)

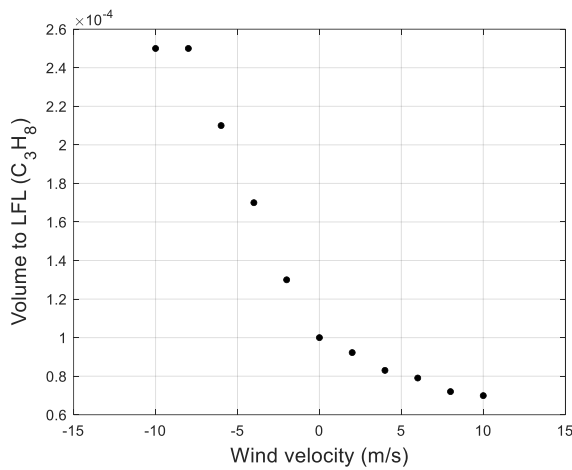


(b)

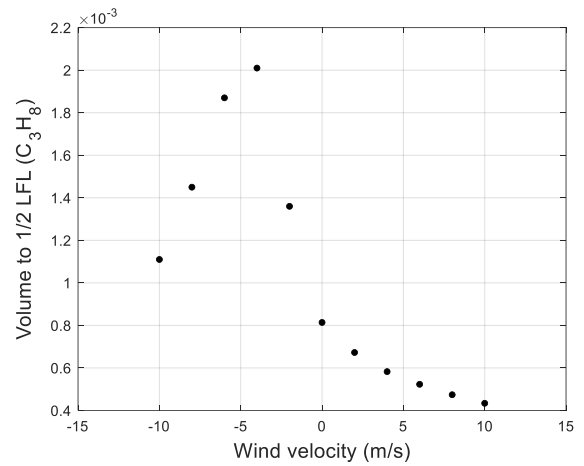


(c)

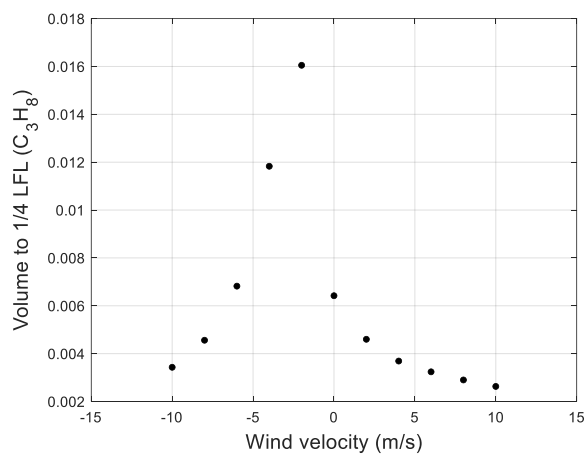
Figure 4.18: Hazardous volume for the methane leakage: (a) to LFL; (b) to 1/2 LFL; (c) to 1/4 LFL.



(a)



(b)



(c)

Figure 4.19: Hazardous volume for the propane leakage: (a) to LFL; (b) to 1/2 LFL; (c) to 1/4 LFL.

Figure 4.20 shows the predicted methane gas molar fraction profile delimited by 25% of the LFL. It visually corroborates that the worst-case scenario, i.e., greater

extent and volume, may contrast to what is found in the literature. Different concentrations lead to distinct volume patterns and plume shapes and, consequently, vary the hazardous area classification results.

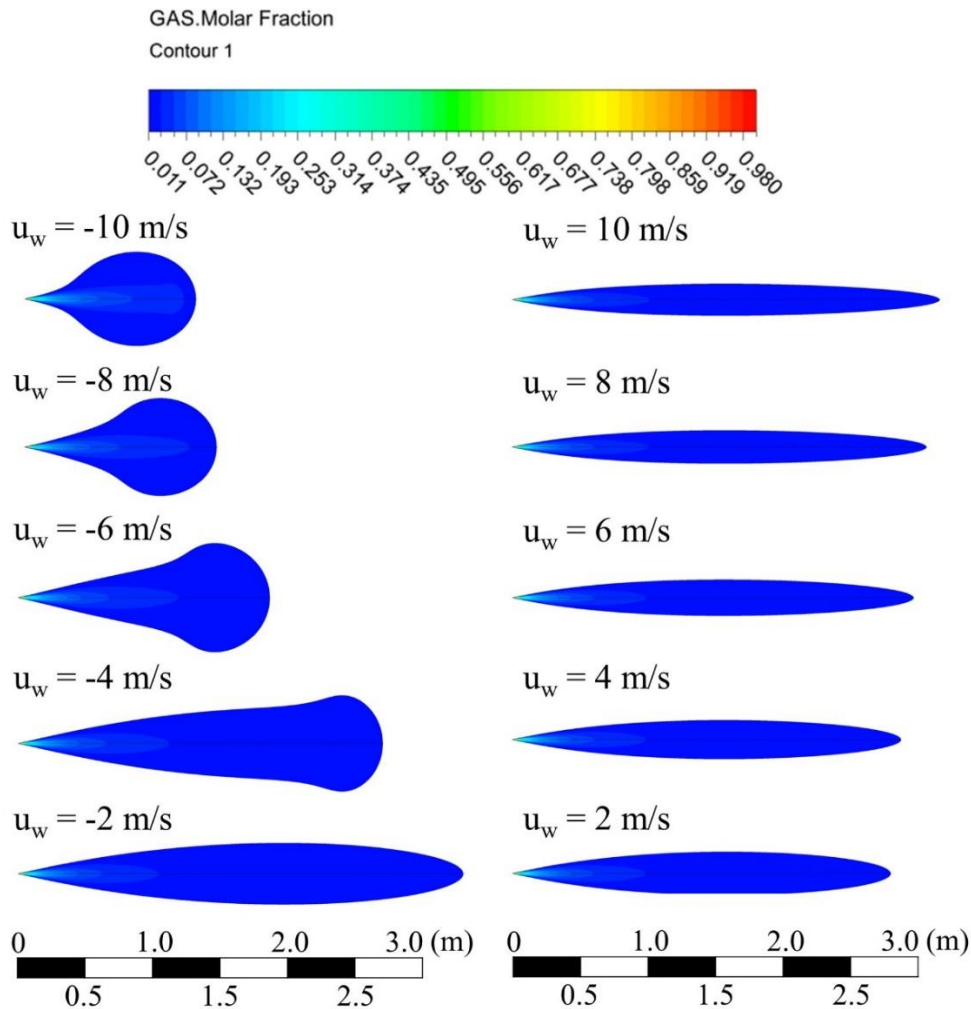


Figure 4.20: Methane gas cloud at $\frac{1}{4}$ LFL for airspeed equals to (a)-10m/s; (b)10m/s; (c)-8m/s; (d)8m/s; (e)-6m/s; (f)6m/s; (g)-4m/s; (h)4m/s; (i)-2m/s; (j)2m/s.

Tables 4.5-4.7 present the hazardous area classification results from the international standard IEC 60079-10-1(2015) and the predicted results from the CFD analyses, considering a continuous grade of release and good availability of ventilation.

Table 4.5: Comparison between CFD results and IEC 60079-10-1(2015) for hydrogen.

	Wind (m/s)	CFD extent in jet direction (m)	CFD extent in jet opposite direction (m)	CFD volume (m ³)	Predicted zone	IEC zone	IEC hazardous distance (m)
LFL	-10	1.142	-	0.160			
	-8	1.408	-	0.219			
	-6	1.839	-	0.296			
	-4	2.649	-	0.355	Zone 0		
	-2	3.054	-	0.255			
	0	2.593	-	0.142		Zone 0	2.664
	2	2.606	-	0.113			
	4	2.663	-	0.095			
	6	2.735	-	0.084	Non- hazardous		
	8	2.811	-	0.077			
	10	2.890	-	0.071			
$\frac{1}{2}$ LFL	-10	1.160	1.371	0.522			
	-8	1.436	0.584	0.681			
	-6	1.891	-	0.985			
	-4	2.790	-	1.776			
	-2	5.429	-	2.875			
	0	5.226	-	1.182	Zone 0	Zone 0	3.820
	2	5.385	-	0.789			
	4	5.702	-	0.628			
	6	6.034	-	0.542			
	8	6.358	-	0.477			
	10	6.670	-	0.430			
$\frac{1}{4}$ LFL	-10	1.169	8.272	2.491			
	-8	1.450	6.425	2.873			
	-6	1.915	4.191	3.565			
	-4	2.845	1.216	5.393			
	-2	5.729	-	14.601			
	0	10.491	-	9.415	Zone 0	Zone 0	5.478
	2	11.486	-	5.121			
	4	12.833	-	3.831			
	6	14.087	-	3.157			
	8	15.244	-	2.809			
	10	16.321	-	2.536			

Table 4.6: Comparison between CFD results and IEC 60079-10-1(2015) for methane.

	Wind (m/s)	CFD extent in jet direction (m)	CFD extent in jet opposite direction (m)	CFD volume (m ³)	Predicted zone	IEC zone	IEC hazardous distance (m)
LFL	-10	0.845	-	5.530E-03	Non- hazardous	Non- hazardous	-
	-8	0.824	-	4.910E-03			
	-6	0.791	-	4.293E-03			
	-4	0.754	-	3.619E-03			
	-2	0.720	-	3.034E-03			
	0	0.691	-	2.691E-03		Zone 0	1.332
	2	0.692	-	2.481E-03			
	4	0.693	-	2.373E-03			
	6	0.695	-	2.251E-03			
	8	0.699	-	2.129E-03		Non- hazardous	-
$\frac{1}{2}$ LFL	-10	1.095	-	4.858E-02	Non- hazardous	Zone 0	1.911
	-8	1.336	-	5.274E-02			
	-6	1.673	-	4.947E-02			
	-4	1.643	-	3.950E-02			
	-2	1.496	-	2.870E-02			
	0	1.376	-	2.103E-02			
	2	1.377	-	1.834E-02			
	4	1.389	-	1.689E-02			
	6	1.406	-	1.545E-02			
	8	1.427	-	1.404E-02			
10	1.450	-	1.348E-02				
$\frac{1}{4}$ LFL	-10	1.132	-	1.795E-01	Zone 0 Non- hazardous	Zone 0	2.740
	-8	1.400	-	2.401E-01			
	-6	1.837	-	3.375E-01			
	-4	2.666	-	4.282E-01			
	-2	3.255	-	3.113E-01			
	0	2.743	-	1.705E-01			
	2	2.768	-	1.327E-01			
	4	2.844	-	1.138E-01			
	6	2.934	-	1.006E-01			
	8	3.030	-	9.055E-02			
10	3.127	-	8.223E-02				

Table 4.7: Comparison between CFD results and IEC 60079-10-1(2015) for propane.

	Wind (m/s)	CFD extent in jet direction (m)	CFD extent in jet opposite direction (m)	CFD volume (m ³)	Predicted zone	IEC zone	IEC hazardous distance (m)
LFL	-10	0.143	-	7.049E-05	Non- hazardous	Non- hazardous	-
	-8	0.173	-	7.200E-05			
	-6	0.189	-	6.030E-05			
	-4	0.179	-	4.895E-05			
	-2	0.166	-	3.737E-05			
	0	0.154	-	2.859E-05		Zone 0	0.213
	2	0.155	-	2.559E-05		Non- hazardous	-
	4	0.156	-	2.312E-05			
	6	0.158	-	2.177E-05			
	8	0.161	-	1.993E-05			
10	0.163	-	1.934E-05				
$\frac{1}{2}$ LFL	-10	0.150	-	3.098E-04	Non- hazardous	Non- hazardous	-
	-8	0.185	-	4.023E-04			
	-6	0.241	-	5.241E-04			
	-4	0.343	-	5.667E-04			
	-2	0.356	-	3.872E-04			
	0	0.304	-	2.264E-04		Zone 0	0.306
	2	0.307	-	1.846E-04		Non- hazardous	-
	4	0.314	-	1.589E-04			
	6	0.324	-	1.438E-04			
	8	0.333	-	1.319E-04			
10	0.344	-	1.203E-04				
$\frac{1}{4}$ LFL	-10	0.152	0.098	9.308E-04	Non- hazardous	Non- hazardous	-
	-8	0.188	0.009	1.258E-03			
	-6	0.249	-	1.919E-03			
	-4	0.366	-	3.279E-03			
	-2	0.683	-	4.464E-03			
	0	0.605	-	1.785E-03		Zone 0	0.438
	2	0.622	-	1.277E-03		Non- hazardous	-
	4	0.657	-	1.028E-03			
	6	0.695	-	8.940E-04			
	8	0.733	-	8.014E-04			
10	0.770	-	7.303E-04				

The outcomes show that, aside from hazardous extent and volume, different wind velocity magnitude and direction also influences the predicted zone type. In all cases, it can be observed that the predicted hazardous volume led to equal or less severe zone type when compared to the IEC 60079-10-1(2015). This mainly occurs because the CFD modelling considers specific characteristics of the gas release phenomenon, e.g., detailed calculation of transport quantities, gas dispersion in a particular environment scenario, accurate prediction of the flammable volume and extent, and the consideration of wind velocity effects on the gas dispersion. The international standard considers that increasing the ventilation velocity speed always promotes a higher dilution and a less severe hazardous classification; however, it can be observed that it is not always true since the counter-flow wind velocity may increase the hazardous volume and also increase the hazardous extent in some scenarios. Significant differences in the hazardous extent were obtained for the hydrogen cases, and higher predicted values were observed. The hazardous extent delimitates the zone type, which means that overestimated extents are costly, while underestimated extents may lead to a lack of safety, as previously discussed in this study case. It is worth mentioning that the standard's method relies on general approximate calculations and recommends using other appropriate tools, especially CFD, to assess the interaction of multiple factors. Therefore, different outcomes from both analyses would be expected since CFD simulations give more detailed and reliable results.

4.4 Final considerations

This work studied the effect of wind speed and direction on the hazardous extent and volume considering different gas leakage conditions for hydrogen, methane, and propane. It contributed to enhancing the comprehension of different wind scenarios using computational fluid dynamics simulations as a tool.

The molar fraction profiles for wind velocity in the opposite direction of the release demonstrate a particular behavior. It decays exponentially along the release axis but rapidly reaches zero molar fraction when the relative velocity between jet and air approaches zero. The opposite wind concentrates the diluted flammable substance in the near field; thus, the hazardous extent and volume pattern vary non-monotonically with the airspeed for different desired concentrations.

Besides the wind effect on the hazardous extent and volume, the wind speed and direction also influence the zone type. This outcome is important for hazardous area classification because an overestimated zone type leads to inappropriate costs, while an underestimated zone type causes a lack of safety.

In contrast to what is found in the literature, the results show that the behavior of the gas cloud extent and volume depends on the gas concentration. Thus, an opposite wind direction may promote a greater extent and volume compared to airflow in the jet direction. This differs from the IEC 60079-10-1(2015), which indicates that a higher amount of ventilation always implies a smaller hazardous volume. These analyses must be taken into consideration in the study of hazardous area classification to obtain detailed information about the flammable region according to different wind scenarios.

This study also demonstrates that CFD is a valuable tool for hazardous area classification, in which accurate analyses for scenarios that cannot be reproduced experimentally are obtained from numerical simulations. The results presented in this study demonstrate an initial analysis of wind influence. This contribution is important because it is considered neither by the international standard nor by the literature. However, this work can also be improved by considering additional scenarios to verify if the plume behavior somehow follows a similar pattern. Analyses of wind influence indoors and considering obstacles may also be investigated, but a tridimensional domain must be considered in these scenarios due to asymmetric conditions.

Chapter 5

Two-phase jets for hazardous area classification

This chapter describes the CFD modeling of two-phase jets into the atmosphere. The study of multiphase release is of particular interest in industrial risk assessments, especially when hazardous area classification analysis is applicable. Both the behavior and the characteristics of these two-phase flow can significantly affect the hazardous zone, which means that as more accurate the flashing jet model is, the more rigorous is the definition of the hazardous area. The investigation of these release phenomena using numerical techniques is relevant since it provides reliable data, especially when physical experiments are not available. Hence, this study case aims to obtain a CFD model that predicts one-component two-phase flow to obtain the flammable cloud volume and extent as a result. It is important to mention that this type of multiphase leakage studies is not entirely understood by the literature, nor is comprehended by the international standard IEC 60079-10-1(2015). Several considerations and simplifications are described throughout this chapter, and the present study contributes with numerical analyses using a three-dimensional computational domain. Two different approaches for calculating the release conditions are evaluated, and the differences between both of them are discussed in this chapter. It also provides data comparison between the predicted hazardous extent to the respective values from the international standard.

5.1 Study case background

Two-phase leakage of flammable substances may occur as a result of different scenarios, such as the releases from stored liquefied gases or saturated liquids. The risk assessment in places where these flammable substances are handled, mainly oil

and gas industries, is one of the concerns related to multiphase jets studies. In such scenarios, hazardous area classification methods must be applied to minimize the risk of explosions, as previously explained in Chapter 4. Moreover, it must always consider worst-case scenarios to ensure safety; therefore, critical emissions are the emphasis here. For two-phase mixtures, critical emission does not refer to sonic flow as it does for gas release. It indicates that the upstream pressure is high enough to result in a choked flow, that is, the maximum flow rate (Lees, 2005).

As a matter of fact, two-phase flows have been widely studied by the literature; however, there is no comprehensive understanding regarding its modeling since it is a complex phenomenon (Giacchetta et al., 2014). As a result of this lack of understanding, the international standard IEC 60079-10-1(2015) does not specifically address two-phase leakages. This often leads to unreliable hazardous area classification. Under such scenario, CFD is an important tool to provide a better evaluation of particular situations.

When considering leakages for hazardous area classification, the orifice diameters are small (up to 5mm²). This value, together with the wall distance to the orifice (l/d_o), determines if the material might or might not have enough time to reach an equilibrium state between the phases, which requires some assumptions to determine the degree of equilibrium attained (Lees, 2005). Some of the considerations are equilibrium, non-equilibrium, and frozen flow, which directly influence the calculation of physical properties as well as the mass fraction of vapor after flashing. Moreover, flashing two-phase discharges is inherently asymmetric, and it requires an accurate prediction of droplets rainout and cloud re-evaporation (Witlox et al., 2007). The determination of the jet breakup, however, contains several uncertainties and is commonly calculated from empirical correlations (Cleary et al., 2007; Witlox and Harper, 2013). Taking these concerns into account, it can be noticed the relevance of two-phase flow studies covering several specific scenarios, which might be helpful to make well-founded decisions for hazardous area classification.

5.1.1 Two-phase jet overview

Two-phase release studies require the development of models for liquid-vapor emission to predict the jet and the gas plume formation, which may depend on the region being evaluated. Epstein et al. (1990) proposed a high momentum jet behavior in which the effects of buoyancy and atmospheric turbulence are negligible near the

release point, as shown in Figure 5.1. The flow is divided into three regions according to the emission behavior, and the definition of each zone is presented in Table 5.1.

Table 5.1: Two-phase release regions.

Region	Definition
Expansion zone	The region where there is a depressurization from orifice pressure to atmospheric pressure. Throughout the expansion, there is jet atomization. At the end of this region, both liquid droplets and gas phase are in thermodynamic equilibrium at boiling temperature.
Jet entrainment zone	In this region, the flammable gas is diluted into atmospheric air, and a secondary break-up may occur. Also, the liquid droplets absorb energy from the gas/air mixture to vaporize.
Dispersion zone	This region is where the continuous air entrainment heats the jet to reach ambient temperature, and the velocity is decreased up to the wind speed.

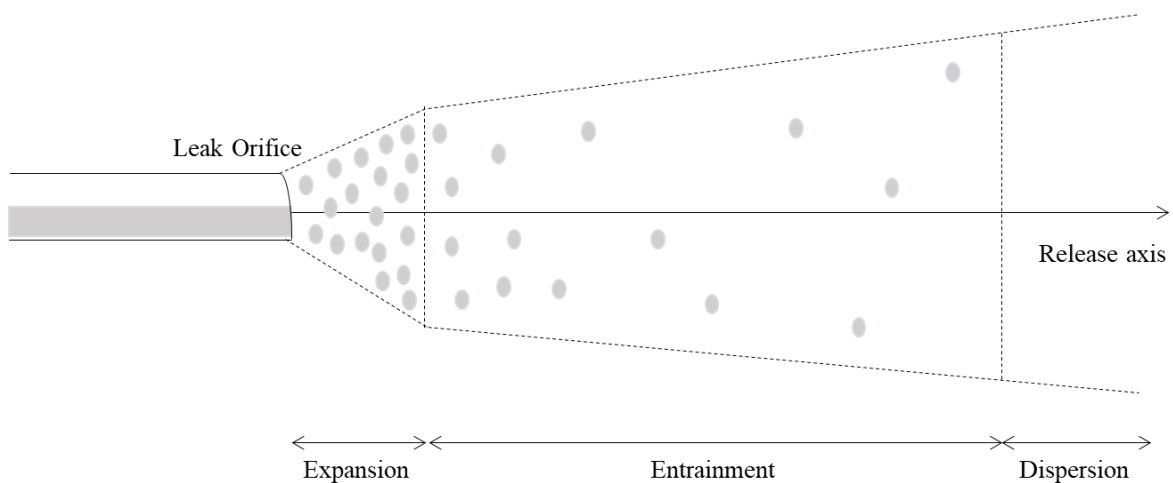


Figure 5.1: Two-phase release.

Several authors have obtained experimental data or proposed models for multiphase leakages. Allen (1998a, 1998b) presented experimental studies of two-phase propane jets using non-intrusive techniques to obtain velocity and temperature along the release axis. It was also provided particle diameter distribution information close to the orifice, where the atomization takes place. These experimental data highly contributed to validate other models.

Calay and Holdo (2008) proposed a numerical approach via Computational Fluid Dynamics to study a two-phase propane emission. The authors evaluated different analytical expressions to determine the release rate, and the results were compared with experimental data obtained by Allen (1998a, 1998b). Given the data analysis, they suggested calculating the two-phase jet release based on the liquid stagnation pressure, as well as to assume equal velocities for both phases. The model considers the emission starting from the entrainment region; thus, details regarding the expansion region are not available.

Polanco et al. (2010) presented a review of theoretical, experimental, and numerical approaches that analyses liquid-vapor emissions. They emphasize that understanding the mechanisms involved in this type of release is important, mainly because it can prevent and minimize the impacts involved in accidental leaks. Moreover, those studies consider that the nature of emission is determined by a combination of variables: temperature, pressure, and orifice geometry are some of them. However, the correlation between those variables is not fully understood by the studies presented by Polanco et al. (2010).

Specific scenarios of a two-phase flow emission have also been treated in the literature. Witlox and Harper (2013) emphasized the importance of predicting the spreading evaporating liquid pool because it contributes to increasing the flammable cloud size from the re-evaporating liquid. The authors presented experimental data of subcooled water and xylene jets, varying stored pressure and orifice diameter. From their results, they proposed a correlation for droplet size that describes the phenomenon.

Oliveira et al. (2019) presented CFD studies of horizontal flashing jets in an open and unobstructed environment to apply the results for hazardous area classification. Their two-dimensional model consisted of an Eulerian-Lagrangian approach, in which the inlet of the computational domain is also defined after the expansion zone. Their numerical study adequately agrees with experiments and demonstrates the behavior of temperature, velocity, droplet diameter, and concentration of the two-phase jet along the emission axis.

The present case study, in turn, aims to evaluate different approaches for two-phase jets release in an open and unobstructed environment and compare the results of flammable cloud formation in a tridimensional domain. Both equilibrium and non-equilibrium states at the orifice are considered and are explained in detail throughout

the next topic. Computational fluid dynamics is used here since it provides an accurate representation of such a complex phenomenon of a given scenario.

5.1.2 Storage condition

Prior to calculating the release condition of the two-phase flow, the storage condition must be specified. This work considers leakage from stored saturated liquid so that only one independent variable must be defined at the vessel: pressure (P_s) or temperature (T_s). Antoine equation (Equation 5.1) is further used to obtain the remaining variable.

$$\log_{10} P_s = A - \frac{B}{T_s + C} \quad (5.1)$$

The physical properties of the liquid in the vessel are then calculated as a function of the temperature.

5.1.3 Release condition

When the leak orifice is located below the storage interface between liquid and vapor, two different conditions at the orifice can occur and are evaluated in this study case. Equilibrium two-phase jet refers to a vapor fraction greater than one at the orifice, in which both phases are in thermodynamic equilibrium, have equal velocities, and are assumed to be homogeneous. On the other hand, a non-equilibrium jet refers to a superheated state at the orifice, considering that there is not enough time to vaporize so that only liquid is present. These considerations directly affect the mass flow calculation, which is a critical variable for determining the hazardous extent and volume, as discussed in this study.

5.1.3.1 Equilibrium two-phase jet

The orifice exit pressure condition (P_o) is initially defined as given in Equation 5.2 (Lees, 2005).

$$P_o = 0.85P_s \quad (5.2)$$

Here, the mixture is assumed to be in an equilibrium state so that the orifice exit temperature (T_o) can be calculated as follows:

$$T_o = \frac{B}{A - \log_{10} P_o} - C \quad (5.3)$$

where A , B , and C are the Antoine coefficients for the released material.

Considering an adiabatic expansion, Equation 5.4 applies to calculate the vapor mass fraction at the orifice (X_{vo}), which enables to obtain the homogeneous mixture density (ρ_{m_o}) using Equation 5.5. The density of each phase is calculated at orifice conditions, and the ideal gas law is used for the gas phase.

$$X_{vo} = \frac{C p_l}{\Delta H_{vap}} (T_s - T_o) \quad (5.4)$$

$$\rho_{m_o} = \frac{1}{X_{vo} \frac{1}{\rho_{g_o}} + (1 - X_{vo}) \frac{1}{\rho_{l_o}}} \quad (5.5)$$

Then, the mixture mass flow can be determined at the orifice by Equation 5.6 (Jones and Underwood, 1983) followed by the calculation of the release velocity, as stated below:

$$m_o = C_d A_o \sqrt{2 \rho_{m_o} (P_s - P_o)} \quad (5.6)$$

$$u_o = \frac{m_o}{\rho_{m_o} A_o} \quad (5.7)$$

where ρ_{g_o} is the gas density, ρ_{l_o} is the liquid density, C_d is the discharge coefficient, A_o is the area of release, m_o is the mass flow at the orifice, and u_o is the release velocity at the orifice.

5.1.3.2. Non-equilibrium jet

A more conservative approach to evaluate a two-phase flow flammable leakage is to consider that there is only liquid at the orifice (Equation 5.8) and that the pressure at this point is equal to the ambient pressure (Equation 5.9), which results in a higher mass flow of the substance. Here, it is assumed that the wall distance to the orifice is sufficiently short so that thermodynamic equilibrium is not reached at the orifice; therefore, the temperature of the liquid remains the same as the saturated liquid at the storage (Equation 5.10). At these conditions (T_s, P_a), the liquid is superheated.

$$X_{vo} = 0 \quad (5.8)$$

$$P_o = P_a \quad (5.9)$$

$$T_o = T_s \quad (5.10)$$

Then, the liquid mass flow and release velocity can be calculated as follows:

$$m_o = C_d A_o \sqrt{2\rho_{lo}(P_s - P_o)} \quad (5.11)$$

$$u_o = \frac{m_o}{\rho_{lo} A_o} \quad (5.12)$$

5.1.4 After-expansion condition

In general, after-expansion values are used as the inlet boundary condition in two-phase flow numerical simulations similar to the present study (Coldrick, 2016; Oliveira et al., 2019; Calay and Holdo, 2008). For both scenarios described at the orifice, it is assumed to occur a flashing jet after-expansion at thermodynamic equilibrium, considering that the pressure after-expansion (P_e) is equal to the ambient pressure (Equation 5.13). It implies that the temperature is equal to the boiling temperature (Equation 5.14), i.e., equilibrium temperature at ambient pressure. Under these conditions, the vapor mass fraction and mixture density are determined from Equations 5.15-5.16:

$$P_e = P_a \quad (5.13)$$

$$T_e = T_b \quad (5.14)$$

$$X_{ve} = \frac{C p_l}{\Delta H_{vap}} (T_o - T_e) \quad (5.15)$$

$$\rho_{m_e} = \frac{1}{X_{ve} \frac{1}{\rho_{ge}} + (1 - X_{ve}) \frac{1}{\rho_{le}}} \quad (5.16)$$

where P_a is the ambient pressure and T_b is the boiling temperature.

From the continuity equation, the mass flow remains the same. Moreover, combining both the continuity and momentum equations, velocity after-expansion (u_e) can be determined as follows:

$$u_e = u_o + \frac{P_o - P_e}{u_o \rho_o} \quad (5.17)$$

Finally, the equivalent orifice area after-expansion (A_e) can be directly calculated from the continuity equation, as shown in Equation 5.18. The equivalent diameter (d_e) is further obtained from Equation 5.19.

$$A_e = \frac{\rho_o u_o A_o}{\rho_{me} u_e} \quad (5.18)$$

$$d_e = \sqrt{\frac{4A_e}{\pi}} \quad (5.19)$$

5.1.4.1. Droplet size

The droplet size after-expansion is calculated in this work based on a correlation from the Phase III of a Joint Industry Project (JIP) on liquid jets and two-phase droplet dispersion (Kay et al., 2010; Witlox et al., 2010). The particle Sauter Mean Diameter (SMD) mainly depends on the degree of superheat (Figure 5.2), in which three regions can be identified: mechanical break-up, transition, and fully flashing.

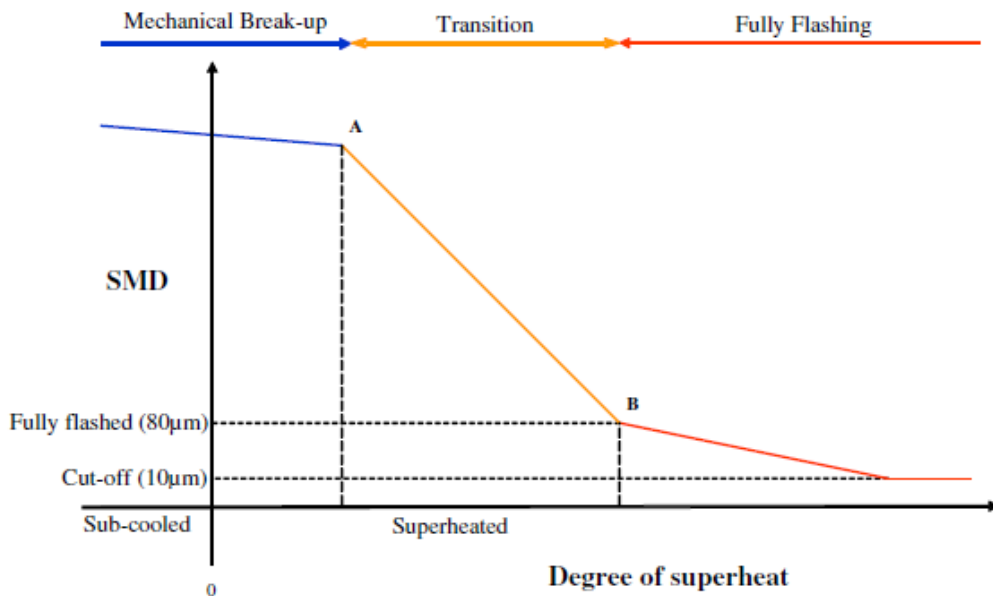


Figure 5.2: SMD as a function of the degree of superheat (Kay et al., 2010)

Points A (ΔT_{sh}^A) and B (ΔT_{sh}^B) are defined as follows (Witlox et al., 2010):

$$\Delta T_{sh}^A = \frac{48 \Delta H_{vap} \rho_{go} We_{vo}^{-\frac{1}{7}}}{Cp_{lo} \rho_{lo} \phi} \quad (5.20)$$

$$\Delta T_{sh}^B = \frac{108 \Delta H_{vap} \rho_{go} We_{vo}^{-\frac{1}{7}}}{Cp_{lo} \rho_{lo} \phi} \quad (5.21)$$

where Cp_l is the specific heat of the liquid ($J kg^{-1} K^{-1}$), ΔH_{vap} is the heat of vaporization ($J kg^{-1}$), We_{vo} is the vapor Weber number evaluated at the orifice, and ϕ is a parameter defined in Equation 5.22.

$$\phi = 1 - e^{-2300(\rho_{go}/\rho_{lo})} \quad (5.22)$$

For the mechanical break-up regime ($T_o - T_b \leq \Delta T_{sh}^A$), the particle mean diameter is calculated as stated in Equation 5.23:

$$\frac{d_p^m}{d_o} = 74 We_{lo}^{-0.85} Re_{lo}^{0.44} \left(\frac{L}{d_o}\right)^{0.114} \left(\frac{\mu_{lo}}{\mu_{H_2O,stp}}\right)^{0.97} \left(\frac{\sigma_{lo}}{\sigma_{H_2O,stp}}\right)^{-0.37} \left(\frac{\rho_{lo}}{\rho_{H_2O,stp}}\right)^{-0.11} \quad (5.23)$$

here, if $\frac{L}{d_o} < 0.1$ then $\frac{L}{d_o} = 0.1$, and when $\frac{L}{d_o} > 50$ it is considered that $\frac{L}{d_o} = 50$.

The droplet mean diameter at the transition ($\Delta T_{sh}^A < T_o - T_b \leq \Delta T_{sh}^B$) and fully flashing ($T_o - T_b > \Delta T_{sh}^B$) regimes are determined from a linear function, as shown in Equations 5.24-5.25, respectively.

$$d_p^t = d_p^m - \frac{\Delta T_{sh} - \Delta T_{sh}^A}{\Delta T_{sh}^B - \Delta T_{sh}^A} (d_p^m - 80 \times 10^{-6}) \quad (5.24)$$

$$d_p^f = \max\{10 \times 10^{-6}, 80 \times 10^{-6} - 10^{-7}(\Delta T_{sh} - \Delta T_{sh}^B)\} \quad (5.25)$$

To summarize, the droplet Sauter Mean Diameter is:

$$SMD = \begin{cases} d_p^m, & \text{if } \Delta T_{sh} \leq \Delta T_{sh}^A \\ d_p^t, & \text{if } \Delta T_{sh}^A < \Delta T_{sh} \leq \Delta T_{sh}^B \\ d_p^f, & \text{if } \Delta T_{sh} > \Delta T_{sh}^B \end{cases} \quad (5.26)$$

Moreover, the droplet diameters are represented by the Rosin-Rammler size distribution (Equation 5.27), which is widely used to describe the mass fraction among particle sizes (ANSYS CFX, 2015).

$$1 - y(d_p) = e^{-\left(\frac{d_p}{SMD}\right)^n} \quad (5.27)$$

Here, $y(d_p)$ is the cumulative mass fraction, and n is the spread parameter that indicates the dispersion of the particle sizes from the mean diameter (SMD). According to the Ansys documentation, a typical value of the spread parameter for sprays varies between 1.5 to 3. In this study, a value of $n = 2$ is used.

5.3 CFD model

The geometry constructed for the present study case represents an open environment after a material release from an expanded diameter (d_e) at 1m above the ground. Figure 5.3 presents the dimensions of the computational domain, in which the expanded diameter is specified for each simulation evaluated in this work. Figure 5.4 shows the isometric view of the geometry constructed on Ansys Design Modeler.

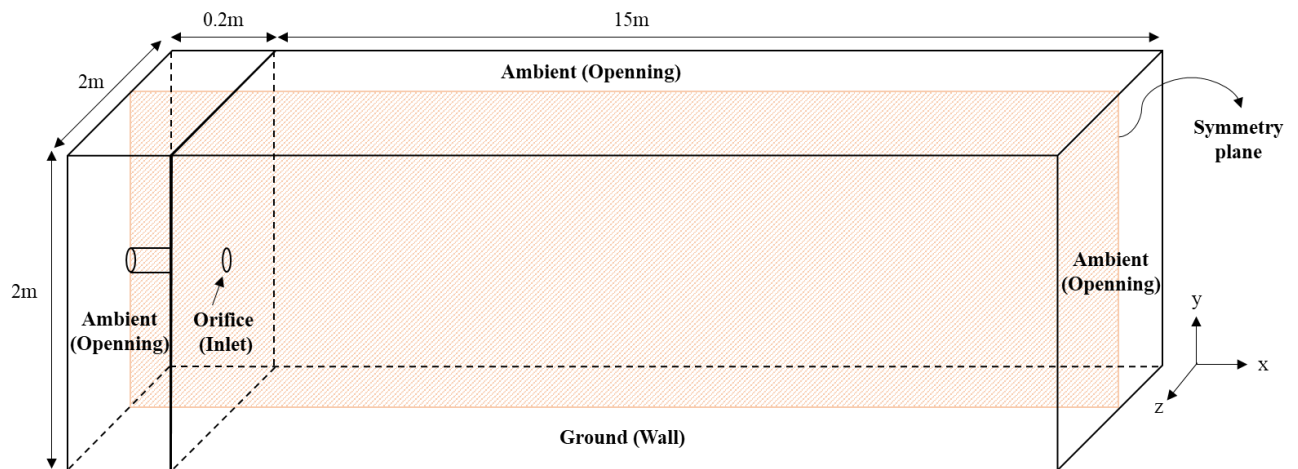


Figure 5.3: Dimensions of the computational domain.

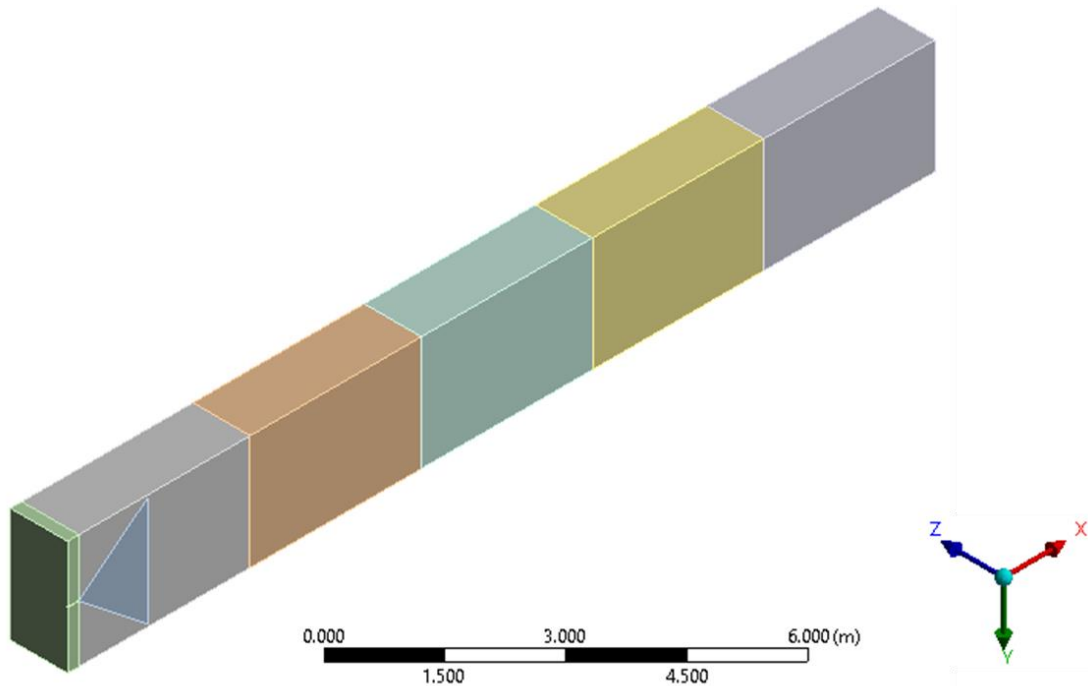


Figure 5.4: Isometric view of the constructed geometry.

The numerical model used in this study case comprehends a propane multiphase flow applying the Eulerian-Lagrangian approach. The continuous phase consists of a gas mixture (air and propane vapor), and the dispersed phase is the liquid propane defined as a particle transport fluid. The phases are fully coupled so that the droplets' momentum also affects the gas momentum. The drag coefficient is calculated by Schiller Naumann model, and the particle breakup is considered here using Reitz and Diwakar model. Liquid Evaporation model is applied to calculate the mass transfer from evaporation, and Ranz-Marshall correlation is used to obtain the interphase heat transfer coefficient. The SST turbulence model was adopted for the continuous phase, and Buoyant model is considered to accurately predict the propane cloud shape since it is a dense gas (specific gravity greater than 1). The convergence criteria were set to 1×10^{-5} for RMS residues and 1% for imbalance, it was used High Resolution for advection scheme and first order for turbulence numerics, and a pseudo time-stepping was set equal to $1 \times 10^{-5}(1 + \textit{number of iteration})$ seconds. Moreover, the definition of the boundary conditions is shown in Table 5.2.

Table 5.2: Definition of the boundary conditions.

Location	Boundary Condition
Orifice	Inlet (gas): Normal speed and static temperature definition; zero gradient turbulence; and mass fraction of propane in the gas mixture (pure substance).
	Inlet (liquid droplets): Normal speed; uniform injection; and Rosin Rammler distribution for droplet size.
Ambient (far-field)	Opening: Ambient pressure (1atm) and temperature (298.15K); zero gradient turbulence; and absence of flammable substance.
Ground	Wall (gas): Non-slip condition; and adiabatic.
	Wall (liquid droplets): Definition of the restitution coefficients (perpendicular coefficient = 0.01, parallel coefficient = 1).
Symmetry faces	Symmetry

The inlet boundary conditions were defined according to the after-expansion values for a given storage condition ($P_s=10\text{bar}$, $T_s=299.1\text{K}$), orifice diameter ($d_o=1\text{mm}$), and discharge coefficient ($C_d=1$). Table 5.3 presents the calculated values for the two configurations to be evaluated: equilibrium and non-equilibrium jet.

Table 5.3: Inlet boundary conditions.

	Equilibrium two-phase jet	Non-equilibrium jet
Velocity (m/s)	137.35	60.59
Temperature (K)	231.11	231.11
Total mass flow rate (g/s)	6.00	23.30
Liquid mass flow rate (g/s)	3.02	15.00
Droplet mean diameter (μm)	73.77	75.28
Expanded diameter (mm)	3.54	8.69

5.3.1 Grid independence study

The mesh was generated according to Figure 5.5. A refined mesh was used in the near-field to resolve the steep gradients of velocity, pressure, and concentration in

that region, while a coarser grid was used closer to the far-field. A grid independence study was performed varying the number of elements between 608163 and 1533582 to obtain a mesh refinement, which gives accurate results that do not depend on the number of elements at a lower computational time. The simulations considered the post-expansion values from Coldrick (2016) as the inlet boundary conditions, which are further used for model verification. The grid independence study evaluated the hazardous extent and volume, and computational time for each simulation, according to Table 5.4.

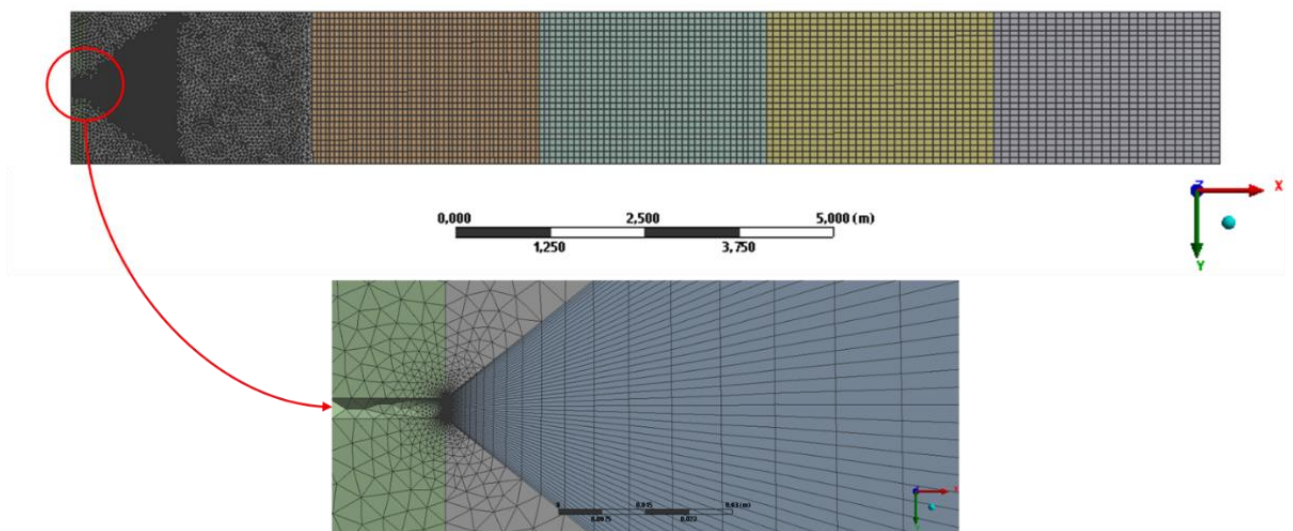


Figure 5.5: Constructed grid for a three-dimensional two-phase flow release.

Table 5.4: Grid independence test.

Mesh/Simulation information	Case 1	Case 2	Case 3	Case 4	Case 5
Elements	608163	861130	920983	1160063	1533582
Computational time	5h14m	8h57m	9h40m	12h22m	15h24m
Extent to LFL (m)	3.1	3.2	3.2	3.2	3.2
Extent to $\frac{1}{2}$ LFL (m)	6.6	6.7	6.7	6.8	6.8
Extent to $\frac{1}{4}$ LFL (m)	13.6	13.7	13.7	13.9	13.9
Volume to LFL (m ³)	0.3	0.3	0.3	0.3	0.3
Volume to $\frac{1}{2}$ LFL (m ³)	2.5	2.5	2.5	2.5	2.5
Volume to $\frac{1}{4}$ LFL (m ³)	16.2	16.2	16.3	16.5	16.3

The results in Table 5.4 show that the desired outcomes are not highly sensitive to the number of mesh elements; therefore, the grid definition in Case 2 was used as the baseline for the CFD simulations since it converges in an acceptable amount of computational time.

5.3.2 Particle number independence study

Eulerian-Lagrangian approach for multiphase flow requires the specification of the number of computational particles to represent the trajectory of all particles in the domain. Table 5.5 presents a sensitivity analysis regarding the number of computational particles, using the inlet conditions from Coldrick (2016).

Table 5.5: Sensitivity analysis of the number of computational particles.

Simulation information	Case 1	Case 2	Case 3	Case 4
Number of computational particles	100	500	1000	1500
Computational time	8h35m	8h57m	9h08m	9h04m
Extent to LFL (m)	3.166	3.166	3.166	3.166
Extent to ½ LFL (m)	6.710	6.713	6.712	6.713
Extent to ¼ LFL (m)	13.679	13.680	13.680	13.680
Volume to LFL (m ³)	0.280	0.281	0.281	0.281
Volume to ½ LFL (m ³)	2.510	2.513	2.515	2.514
Volume to ¼ LFL (m ³)	16.230	16.223	16.221	16.222

Similarly to the grid independence test, the hazardous extent and volume results are not highly sensitive to the number of computational particles. However, it was observed that the numerical stability increased for a higher number of particles; for that reason, Case 2 (500 computational particles) was chosen to be used in the CFD simulations.

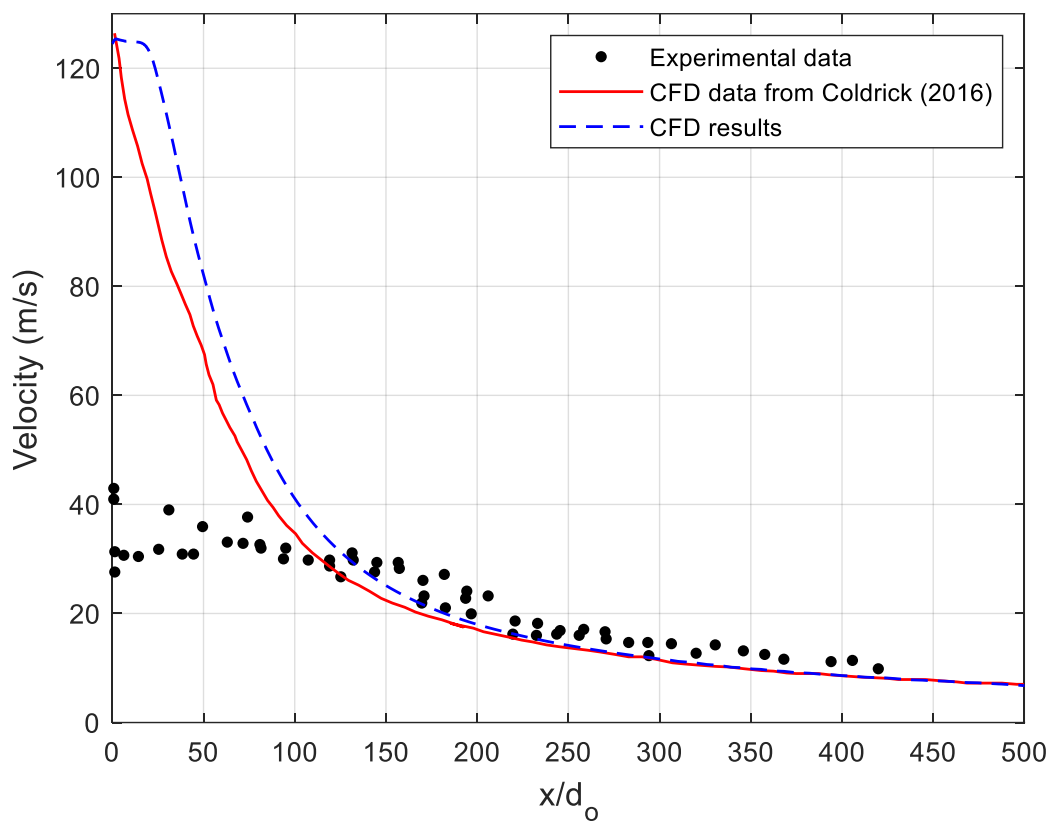
5.3.3 Model verification

The CFD model above-mentioned was verified against literature data from Coldrick (2016), which presents previous experimental data from Allen (1995) along with CFD results. The scenario consists of a propane release under 7.47bar and 288.8K at the storage, releasing from a 4mm orifice diameter. The boundary conditions

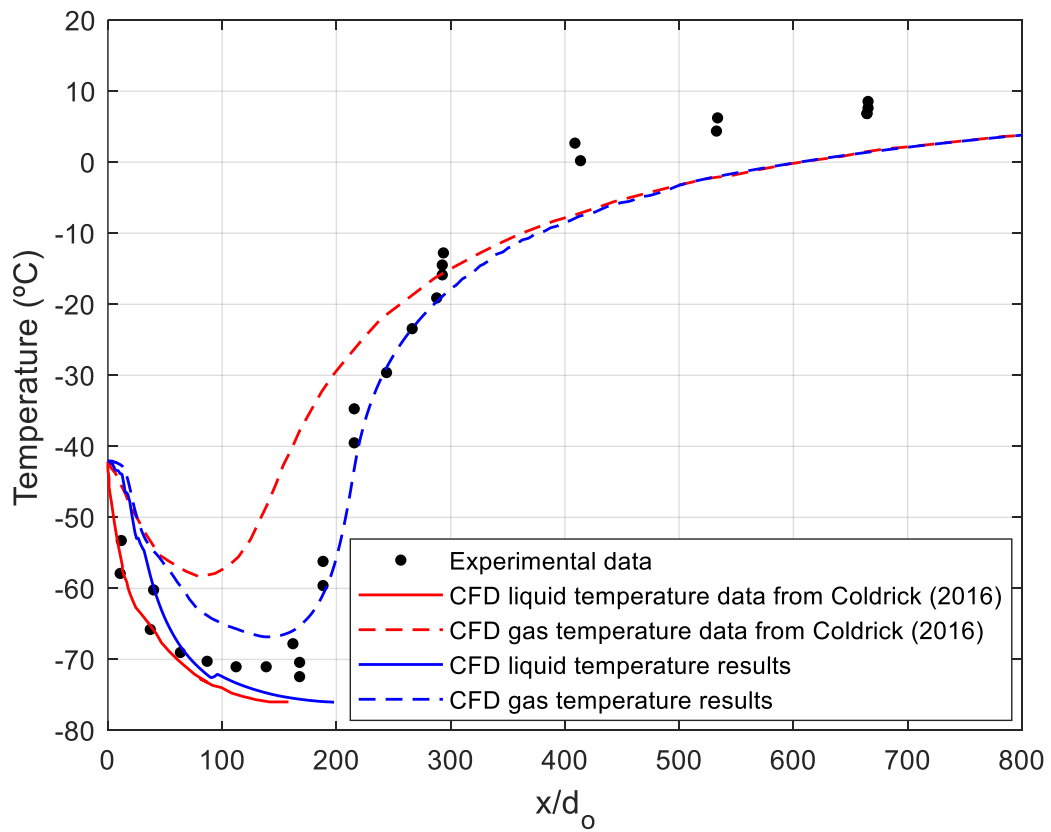
were set according to the post-expanded values in Table 5.6, and the results are compared in Figure 5.6.

Table 5.6: Boundary condition values.

Parameter	Value
Inlet velocity (m/s)	124.56
Inlet temperature (°C)	-42.07
Inlet liquid mass flow (g/s)	47.80
Expanded diameter (mm)	9.60
Droplet diameter (µm)	20.00
Ambient temperature (°C)	288.80



(a)



(b)

Figure 5.6: Two-phase release model verification: (a) velocity profile; (b) temperature profile.

Figure 5.6(a) shows that the CFD predicted results were comparable to the outcomes from Coldrick (2016), although both sets of data demonstrate a large difference in the velocity values for $x/d_o < 100$ when compared to the experimental data. Coldrick (2016) suggests that the reason for that is the uncertainty of the released material state, which directly affects the orifice velocity calculation. However, for $x/d_o > 100$, the predicted results adequately agree with the experimental data. In terms of temperature along the release axis (Figure 5.6(b)), the CFD data also agree with the experimental data, in which the temperature decay is a result of droplets evaporation.

5.4 Results

Important measurements for hazardous area classification are the hazardous volume, which indicates the zone type (as discussed in Chapter 4), and the hazardous extent. Both variables are presented in Table 5.7 for each concentration evaluated, i.e., LFL, $\frac{1}{2}$ LFL, and $\frac{1}{4}$ LFL. In this case, the lower flammable limit of propane is

0.021vol/vol. Also, the two-phase length is given below to specify the maximum horizontal distance that the liquid droplets reach in the domain.

Table 5.7: Hazardous extent and volume.

	Equilibrium two-phase jet	Non- equilibrium jet
Extent to LFL (m)	1.007	2.782
Extent to ½ LFL (m)	1.923	6.212
Extent to ¼ LFL (m)	3.709	9.601
Volume to LFL (m ³)	0.008	0.162
Volume to ½ LFL (m ³)	0.060	1.686
Volume to ¼ LFL (m ³)	0.455	6.123
Two-phase length (m)	0.540	1.989

As expected, the hazardous extent and volume results for the Non-equilibrium jet simulation are greater than the Equilibrium two-phase jet simulation. This happens due to a higher released mass flow when considering only the superheated liquid phase in the real orifice. The hazardous extents are three times greater for the Non-equilibrium jet simulation, and its hazardous volumes are large enough to be considered a hazardous area in any concentration evaluated in Table 5.7 ($V > 0.1\text{m}^3$). On the other hand, the Equilibrium two-phase jet case may only be considered a hazardous area for a vapor cloud delimited at ¼ LFL. This classification takes into consideration a good availability of ventilation (open environment) and a continuous grade of release.

Figures 5.7 and 5.8 illustrate the cloud shape for each simulation at ¼ LFL. It is worth remembering that the storage condition is the same for both cases and that the difference between them relies on the calculation of the release condition. The accurate prediction of the nature of release is one of the struggles of two-phase flow emissions, and the results show that this significantly affects the hazardous extent and volume. For instance, at ¼ LFL, the propane gas cloud does not touch the ground for the Equilibrium two-phase jet simulation in contrast with a gas cloud that already reaches the ground surface for the Non-equilibrium jet simulation. Figures 5.7 and 5.9 also show the trajectory of the computational particles in the enlarged images, and it

can be observed the longer trajectory for Non-equilibrium jet simulation compared to the Equilibrium two-phase jet simulation.

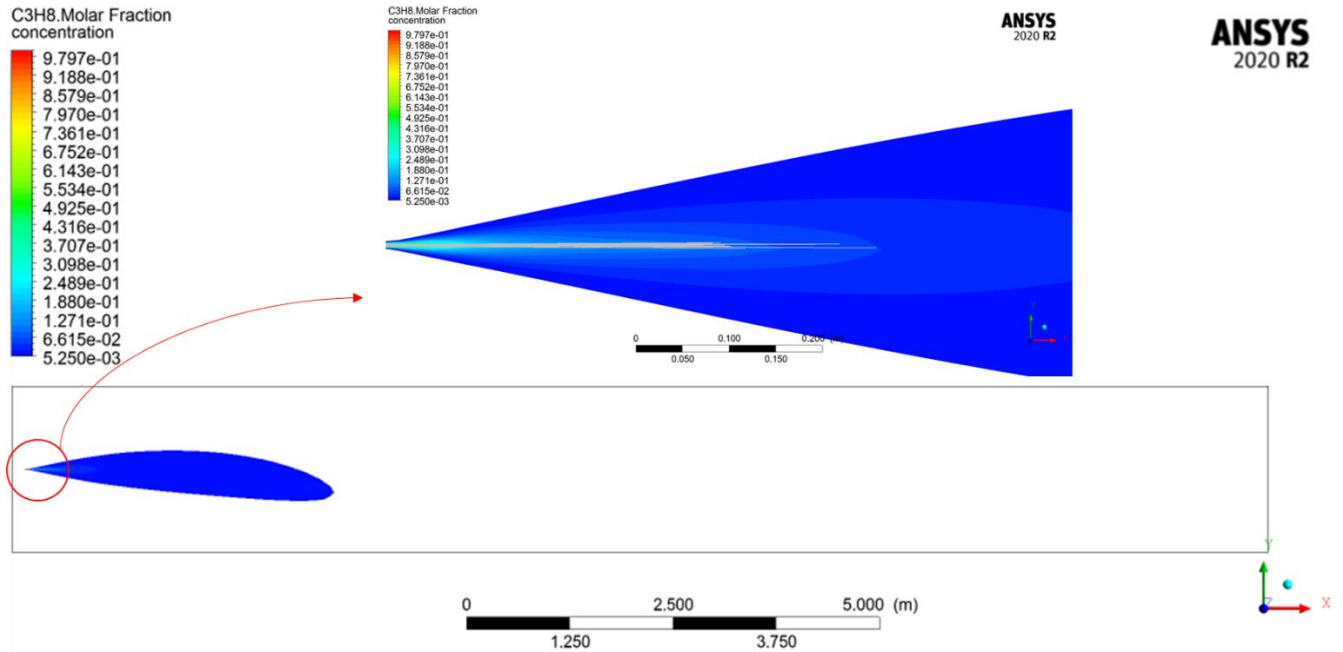


Figure 5.7: Propane gas cloud at 1/4 LFL for the Equilibrium two-phase jet simulation.

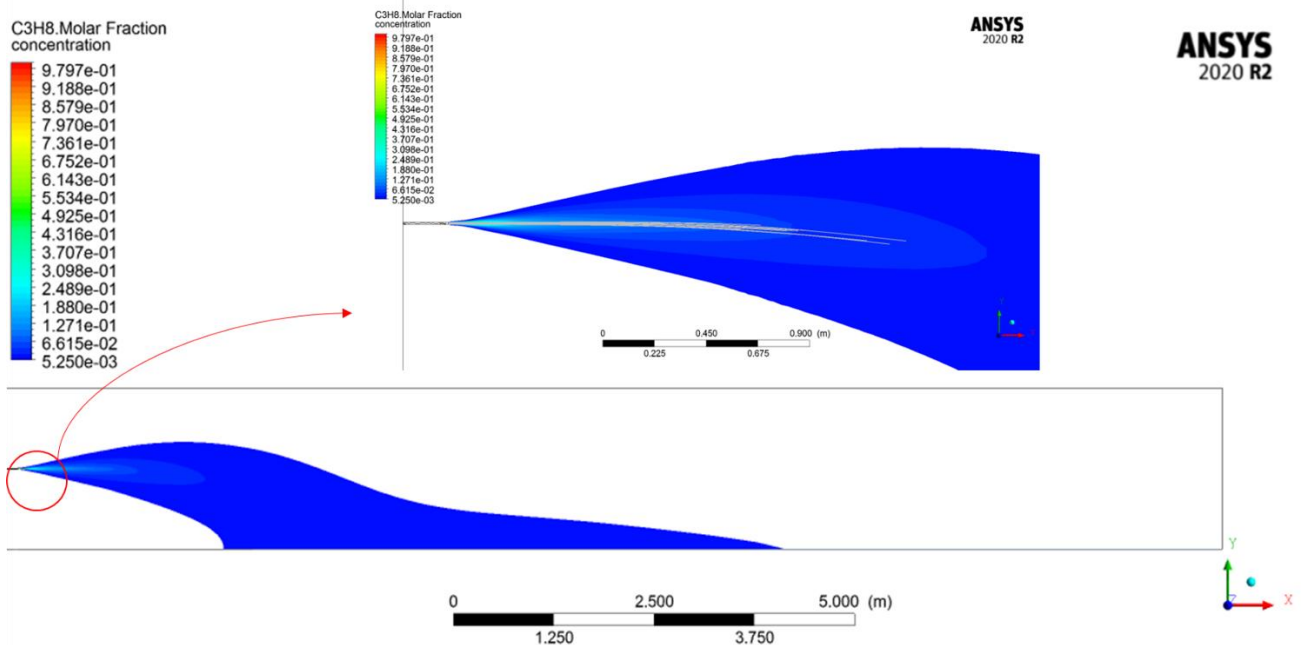


Figure 5.8: Propane gas cloud at 1/4 LFL for the Non-equilibrium jet simulation.

Since the Equilibrium two-phase jet consideration assumes a homogeneous thermal equilibrium, it is mostly applied when the ratio between the pipe length, or wall

thickness, and the orifice diameter is high enough for equilibrium to be established. Otherwise, the assumption of superheated (non-equilibrium) liquid at the orifice is more adequate. In terms of hazardous area classification, the most conservative approach is more appropriate because it implies process safety. Also, due to the considerable difference between the results and the lack of data to predict the nature of the release, the worst-case scenario of the flammable cloud formation must be addressed. Therefore, the Non-equilibrium jet simulation results should be indicated as a default/initial analysis for further hazardous area classification.

Considering that the release scenario covered in this study case is a leakage in an open and unobstructed ambient, the availability of ventilation is assumed to be good. Thus, if the hazardous volume is greater than 0.1m^3 , the zone type is classified as Zone 0, which is the case of the Non-equilibrium jet simulation. In terms of the hazardous extent, the determination from the international standard IEC 60079-10-1(2015) comes from the heavy gas line in the hazardous distance chart (Figure 4.4) since it is a propane release. Table 5.8 shows a comparison between the hazardous distance from the CFD simulation and the prediction from the international standard.

Table 5.8: Comparison between CFD and IEC 60079-10-1(2015) results for hazardous extent.

	CFD extent (m)	IEC extent (m)
LFL	2.782	3.778
½ LFL	6.212	5.343
¼ LFL	9.601	7.556

The results show that the IEC extent overestimated the hazardous extent to LFL by 35.8% but underestimated the distances for the other concentrations. One of the reasons for the underestimated outcomes is because the ground effect is not being considered by the international standard IEC 60079-10-1 (2015). When the flammable cloud reaches the ground, the hazardous extent tends to increase, which is predicted by the CFD simulation. These outcomes corroborate the statement from IEC 60079-10-1(2015) that recommends the usage of CFD tools to analyze specific scenarios, assuring process safety.

5.5 Final considerations

This work evaluated two different approaches to obtain the release conditions for two-phase flows for hazardous area classification. The first condition, called Equilibrium two-phase jet, assumed the homogeneous equilibrium model, while the Non-equilibrium jet approach assumed a superheated condition at the orifice. The main difference between them consists in the nature of release, which directly affects the leaked mass flow. These variables were used as inlet conditions in a CFD simulation to predict the flammable gas cloud formation after the discharge. Results show that the flammable mass flow significantly affects both the hazardous extent and volume, which are the most important variables for hazardous area classification. The hazardous extent was three times greater for the Non-equilibrium jet approach, while the volume was up to 28 times greater. Due to this considerable difference and the uncertainties regarding the nature of the release, it is recommended that the most conservative model should be addressed to ensure process safety. Otherwise, the engineer should be assured that an equilibrium condition satisfies that specific release scenario. This case occurs when the ratio between pipe length, or wall thickness, and orifice diameter is high enough so that the thermodynamic equilibrium is reached.

This study case reinforces the importance of CFD simulations, especially to analyze a complex two-phase flow phenomenon in specific scenarios. The numerical simulation is a reliable source for the flammable gas cloud prediction, which may support hazardous area classification to avoid overestimation of the hazardous area or to prevent underestimations that lead to unsafe conditions.

References

ANSYS CFX - Solver Theory Guide. (2015). ANSYS Inc., Canonsburg, United States.

ALLEN, J. T. Conventional temperature measurements in small scale two-phase flashing propane jet releases, HSL report IR/L/FR95/5, 1995.

ALLEN, J. T. Laser-based measurements in two-phase flashing propane jets. Part one: Velocity profiles. *Journal of Loss Prevention in the Process Industries*, v. 11, p. 291-297, 1998a.

ALLEN, J. T. Laser-based measurements in two-phase flashing propane jets. Part two: Droplet size distribution. *Journal of Loss Prevention in the Process Industries*, v. 11, p. 299-306, 1998b.

ALVES, J.J.N.; NETO, A.T.P.; ARAUJO, A.C.B.; SILVA, H.B.; SILVA, S.K.; NASCIMENTO, C.A.; LUIZ, A.M. Overview and experimental verification of models to classify hazardous areas. *Process Safety and Environmental Protection*, v. 122, p. 102-117, 2019.

BRADLEY, D. *The hydrocyclone*. Pergamon Press, London, 1965.

BENINTENDI, R. Turbulent jet modelling for hazardous area classification. *Journal of Loss Prevention in the Process Industries*, v.23, p. 373-378, 2010.

BENINTENEDI, R. Laminar jet modelling for hazardous area classification. *Journal of Loss Prevention in the Process Industries*, v. 24, p. 123-130, 2011.

BERGAYA, F.; LAGALY, G. *Handbook of Clay Science*. Volume 1; Elsevier: Amsterdam, NL, 2006.

BLAZEK, J. *Computational Fluid Dynamics: Principles and Applications*. Butterworth-Heinemann, 3 ed., 2015.

CALAY, R. K.; HOLDO, A. E. Modelling and dispersion of flashing jets using CFD. *Journal of Hazardous Materials*, v. 154, p. 1198-1209, 2008.

CLEARY, V.; BOWEN, P.; WITLOX, H. Flashing liquid jets and two-phase droplet dispersion I. Experiments for derivation of droplet atomization correlations. *Journal of Hazardous Materials*, v. 142, p. 786-796, 2007.

COLDRICK, S. Modelling Small-scale Flashing Propane Jets. *Chemical Engineering Transactions*, v. 48, p.73-78, 2016.

CUI, B.; ZHANG, C.; WEI, D.; LU, S.; FENG, Y. Effects of feed size distribution on separation performance of hydrocyclones with different vortex finder diameters. *Powder Technology*, v. 322, p. 114-123, 2017.

CULLIVAN, J. C.; WILLIAMS, R. A.; DYAKOWSKI, T.; CROSS, C. R. New understanding of a hydrocyclone flow field and separation mechanism from computational fluid dynamics. *Minerals Engineering*, v. 17, p. 651-660, 2004.

EWAN, B.C.R.; MOODIE, K. Structure and velocity measurements in under-expanded jets. *Combustion Science Technology*, v. 45, p. 275-288, 1986.

EPSTEIN, M.; FAUSKE, H. K.; HAUSER, G. M. A model of the dilution of a forced two-phase chemical plume in a horizontal wind. *Journal of Loss Prevention in the Process Industries*, v. 3, p. 280-290, 1990.

FAVERO, J. S.; PARISOTTO-PETERLE, J.; WEISS-ANGELI, V.; BRANDALISE, R. N.; GOMES, L. B.; BERGMANN, C. P.; SANTOS, V. Physical and chemical characterization and method for the decontamination of clays for application in cosmetics. *Applied Clay Science*, v. 124-125, p. 252-259, 2016.

GAMA, A.J.A.; FIGUEIREDO, J.M.R.; BRITO, A.L.F.; GAMA, M.A.; NEVES, G.A.; FERREIRA, H.C. Factorial design and statistical analysis of smectite clay treatment by hydrocyclone. *Ceramica*, v. 64, p. 57-63, 2018.

GHODRAT, M.; KUANG, S. B.; YU, A. B.; VINCE, A.; BARNETT, G. D.; BARNETT, P. J. Computational study of the multiphase flow and performance of hydrocyclones: effects of cyclone size and spigot diameter. *Industrial and Engineering Chemistry Research*, v. 52, p. 16019-16031, 2013.

GIACCHETTA, G.; LEPORINI, M.; MARCHETTI, M.; TERENCEZI, A. Numerical study of choked two-phase flow of hydrocarbons fluids through orifices. *Journal of Loss Prevention in the Process Industries*, v. 27, p. 13-20, 2014.

GUGGENHEIM, S.; MARTIN, R. T. Definition of clay and clay mineral: joint report of the AIPEA nomenclature and CMS nomenclature committees. *Clays and Clay Minerals*, v.43 (2), p. 255-256, 1995.

HONG, J.; XI, D.; JIAO, W. Numerical simulation of particle separation in a hydrocyclone. *Applied Mechanics and Materials*, v. 713-715, p. 1786-1789, 2015.

HSIEH, K. T.; RAJAMANI, K. Phenomenological Model of the Hydrocyclone: Model Development and Verification for Single-Phase Flow. *International Journal of Mineral Processing*, v. 22, p. 223-237, 1988.

IVINGS, M. J.; GANT, S. E.; SAUNDERS, C. J.; POCOCK, D. J. Flammable gas cloud build up in a ventilation enclosure. *Journal of Hazardous Materials*, v. 184, p. 170-176, 2010.

IEC 60079-10-1/Ed2. Explosive Atmospheres – Part 10-1: Classification of Areas – Explosive Gas Atmospheres, 2015.

JI, L.; KUANG, S.; YU, A. Numerical Investigation of Hydrocyclone Feed Inlet Configurations for Mitigating Particle Misplacement. *Industrial and Engineering Chemistry Research*, v. 58 (36), p. 16823-16833, 2019.

JONES, M. R. O.; UNDERWOOD, M. C. An appraisal of expressions used to calculate the release rate of pressurized liquefied gases. *The Chemical Engineering Journal*, v. 26, p. 251-254, 1983.

KAY, P.; BOWEN, P.J.; WITLOX, H.W.M. Sub-cooled and flashing liquid jets and droplet dispersion, II. Scaled experiments and derivation of droplet atomisation correlations. *Journal of Loss Prevention in the Process Industries*, v. 23, p. 849-856, 2010.

LEES, F. *Lees' Loss Prevention in the Process Industries: Hazard Identification, Assessment and Control*, 3 ed. v. 1. Butterworth-Heinemann, 2005.

- LI, X.; ABBASSI, R.; CHEN, G.; WANG, Q. Modeling and analysis of flammable gas dispersion and deflagration from offshore platform blowout. *Ocean Engineering*, v. 201, 107146, 2020a.
- LI, X.; HAN, Z.; YANG, S.; CHEN, G. Underwater gas release modeling and verification analysis. *Process Safety and Environmental Protection*, v. 137, p. 8-14, 2020b.
- LI, X.; CHEN, G.; ZHANG, R.; ZHU, H.; XU, C. Simulation and assessment of gas dispersion above sea from subsea release: A CFD-bases approach, *International Journal of Naval Architecture and Ocean Engineering*, v. 11(1), p. 353-363, 2019.
- MCMILLAN, A. *Electrical Installations in Hazardous Area*. Elsevier Science LTD, 1998.
- MENTER, F. R. Review of the shear-stress transport turbulence model experience from an industrial perspective. *International Journal of Computational Fluid Dynamics*, v. 23:4, p. 305-316, 2009.
- MOKNI, I.; BOURNOT, P.; MHIRI, H. Feed temperature effect on separation performance of industrial hydrocyclone: advanced CFD analysis. *Separation Science and Technology*, 2019. DOI: 10.1080/01496395.2019.1617739.
- MURANO, H.; TAKATA, Y.; ISOI T. Origin of the soil texture classification system used in Japan. *Journal of Soil Science and Plant Nutrition*, v. 61, p. 688-697, 2015.
- NI, L.; TIAN, J.; ZHAO, J. Experimental study of the relationship between separation performance and lengths of vortex finder of a novel de-foulant hydrocyclone with continuous underflow and reflux function. *Separation Science Technology*, v. 52 (1), p. 142-154, 2017.
- NI, L.; TIAN, J.; SONG, T.; JONG, Y.; ZHAO, J. Optimizing geometric parameters in hydrocyclones for enhanced separations: a review and perspective. *Separation and Purification Reviews*, v. 48 (1), p. 30-51, 2019.
- OLIVEIRA, T.C.L.; NETO, A.T.P.; ALVES, J.J.N. CFD Simulation of flashing jet applied to area classification. *The Canadian Journal of Chemical Engineering*, v. 97, p. 465-476, 2019.

ÖZGEN, S.; YILDIZ, A.; ÇALIŞKAN, A.; SABAH, E. Modeling and optimization of hydrocyclone processing of low grade bentonites. *Applied Clay Science*, v. 46, p. 305-313, 2009.

PAPANIKOLAOU, E.; BARALDI, D.; KUZNETSOV, M.; VENETSANOS, A. Evaluation of notional nozzle approaches for CFD simulations of free-shear under-expanded hydrogen jets. *International Journal of Hydrogen Energy*, v.37(23), p.18563-18574, 2012.

POLANCO, G.; HOLDO, A. E.; MUNDAY, G. General review of flashing jet studies. *Journal of Hazardous Materials*, v. 173, p. 2-18, 2010.

SABBAGH, R.; LIPSETT, M. G.; KOCH, C. R.; NOBES, D. S. An experimental investigation on hydrocyclone underflow pumping. *Powder Technology*, v. 305, p. 99-108, 2017.

SILGADO-CORREA, K. J.; FERREIRA, T. D.; VIANNA, S. S. V. Leak release momentum and the convective flow influence on the calculation of the flammable cloud. *Journal of Loss Prevention in the Process Industries*, v. 65, 104123, 2020.

SILVA, C.L.Q.; PENNA, W.; ARAÚJO, A.C.B.; BRITO, R.P.; VASCONCELOS, L.G.S.; ALVES, J.J.N. Model fine tuning for prediction of hydrocyclone performance - An industrial case study. *International Journal of Mineral Processing*, v. 92, p. 34-41, 2009.

SISSOM, L.E.; PITTS, D.R. *Elements of Transport Phenomena*. McGraw-Hill Book Company, New York, USA, 1972.

SOUZA, A.O.; LUIZ, A. M.; NETO, A.T.P.; ARAUJO, A.C.B.; SILVA, H.B.; SILVA, S.K.; ALVES, J.J.N. A new correlation for hazardous area classification based on experiments and CFD predictions. *Process Safety Progress*, v. 31 (1), p. 21-26, 2018.

SOUZA, A.O.; LUIZ, A. M.; NETO, A.T.P.; ARAUJO, A.C.B.; SILVA, H.B.; SILVA, S.K.; ALVES, J.J.N. CFD predictions for hazardous area classification. *Chinese Journal of Chemical Engineering*, v. 27, p. 21-31, 2019.

SVAROVSKY, L. *Hydrocyclones*. Volume 1; Technomic Pub Co.:Pennsylvania, US, 1984.

- SVAROVSKY, L. Solid-Liquid Separation. 4th Edition; Butterworth-Heinemann, 2001.
- SWAIN, S.; MOHANTY, S. A 3-dimensional Eulerian-Eulerian CFD simulation of a hydrocyclone. *Applied Mathematical Modelling*, v. 37, p. 2921-2931, 2013.
- TANG, B.; XU, Y.; SONG, X.; SUN, Z.; YU, J. Numerical study on the relationship between high sharpness and configurations of the vortex finder of a hydrocyclone by central composite design. *Chemical Engineering Journal*, v. 15, p. 504-516, 2015.
- TOMMASINI, R. The classification of hazardous areas where explosive atmospheres may be present. *Safety Science*, v. 58, p. 53-58, 2013.
- TOWLER, G.; SINNOTT, R. K. *Chemical Engineering Design: Principles, Practice and Economics of Plant and Process Design*, 2nd ed.; Butterworth-Heinemann: Boston, USA, 2013.
- TU, J.; YEOH, G.; LIU, C. *Computational Fluid Dynamics: A Practical Approach*. Butterworth-Heinemann, 3 ed., 2018.
- VAKAMALLA, T. R.; KUMBHAR, K. S.; GUJJULA, R.; MANGADODDY, N. Computational and experimental study of the effect of inclination on hydrocyclone performance. *Separation and Purification Technology*, v. 138, p. 104-117, 2014.
- VAKAMALLA, T. R.; KORUPROLU, V.B.R.; ARUGONDA, R.; MANGADODDY, N. Development of novel hydrocyclone designs for improved fines classification using multiphase CFD model. *Separation and Purification Technology*, v. 175, p. 481-497, 2017.
- WANG, B.; YU, A. B. Numerical study of particle-fluid flow in hydrocyclones with different body dimensions. *Minerals Engineering*, v. 19, p. 1022-1033, 2006.
- WEBBER, D. M.; IVINGS, M. J.; SANTON, R. C. Ventilation theory and dispersion modelling applied to hazardous area classification. *Journal of Loss Prevention in the Process Industries*, v. 24, p. 612-621, 2011.
- WITLOX, H.; HARPER, M.; BOWEN, P.; CLEARY, V. Flashing liquid jets and two-phase droplet dispersion II. Comparison and validation of droplet size and rainout formations. *Journal of Hazardous Materials*, v. 142, p. 797-809, 2007.

WITLOX, H.W.M.; HARPER, M. Two-phase jet releases, droplet dispersion and rainout I. Overview and model validation. *Journal of Loss Prevention in the Process Industries*, v. 26, p. 453-561, 2013.

WITLOX, H. W. M.; HARPER, M.; OKE, A.; KAY, P.; BOWEN, P. J. Sub-cooled and flashing liquid jets and droplet dispersion, I. Overview and model implementation/validation. *Journal of Loss Prevention in the Process Industries*, v. 23, p. 831-842, 2010.

YANG, X.; SIMMONS, M. J.; LIU, P.; ZHANG, Y.; JIANG, L. Effect of feed body geometry on separation performance of hydrocyclone. *Separation Science and Technology*, v. 54, p. 2959-2970, 2019.

YE, J.; XU, Y.; SONG, X.; YU, J. Novel conical section design for ultra-fine particles classification by a hydrocyclone. *Chemical Engineering Research and Design*, v. 144, p. 135-149, 2019.

ZHANG, Y.; CAI, P.; JIANG, F.; DONG, K.; JIANG, Y.; WANG, B. Understanding the separation of particles in a hydrocyclone by force analysis. *Powder Technology*, v. 322, p. 471-489, 2017.

ZHANG, C.; CUI, B.; WEI, D.; LU, S. Effects of underflow orifice diameter on the hydrocyclone separation performance with different feed size distributions. *Powder Technology*, v. 355, p. 481-494, 2019.

ZHU, G.; LIOW, J.; NEELY, A. Computational study of the flow characteristics and separation efficiency in a mini-hydrocyclone. *Chemical Engineering Research and Design*, v. 90, p. 2135-2147, 2012.

ZHIYIN, Y. Large-eddy simulation: Past, present and the future. *Chinese Journal of Aeronautics*, v. 28 (1), p. 11-24, 2015.

ZOHDIRAD, H.; EBADI, T.; GIVEHCHI, S.; MEYSAMI, H. Grid-based individual risk calculation in the classification of hazardous area with a risk-based approach. *Journal of Loss Prevention in the Process Industries*, v. 43, p. 98-105, 2016.